Energy Storage Materials Using Metal Boranes as Solid-State Electrolytes

Thomas Adam Hales

0000-0003-3264-9894

This thesis is presented for the Degree of

Doctor of Philosophy

of

Curtin University

March 2024

DECLARATION

To the best of my knowledge and belief this thesis contains no material previously published by any other person except where due acknowledgment has been made.

This thesis contains no material which has been accepted for the award of any other degree or diploma in any university.

COPYRIGHT STATEMENT

ACKNOWLEDGEMENTS

Firstly, I would like to thank my parents, Andrew and Jane, my sister Lucy, and the rest of my family for their everlasting support and encouragement to follow my dreams, aim high and go for it. Also, all of my Australian family who have adopted me, supported and looked after me ever since moving to Australia. Everyone at Jandakot Park Cricket Club, especially Adam Bryce and Anthony Wright for all the lifts I have asked for, to and from cricket, and for being great friends whenever I've needed them. All of my housemates in particular Sarah Loughnan, who took me into her home and showed me the great city of Perth for my first 2 years.

I acknowledge everyone in the Hydrogen Storage Research Group (HSRG) both past and present for the help and support throughout my PhD whether that be in the lab or in everyday life, they have been there and are all a massive reason why this thesis has been possible. I would like to give special mention to Dr Amanda Berger and Dr Diego Holanda Pereira de Souza for all their laboratory help and general good times spent whilst we completed our PhDs. My primary supervisor, Assoc. Prof. Mark Paskevicius, has been the best supervisor I could ever ask for and I would not have finished this without his unwavering guidance and support even when I've had setbacks and have been hard to deal with. I would also like to thank Prof. Craig Buckley for his support and guidance of myself and the whole group, and our AFL discussions over a beer on a Friday afternoon. Furthermore, I cannot thank Dr Terry Humphries and his wife Keelie Munroe enough for not only their support with my PhD, both technically and doing Synchrotron night shifts with but also, inviting me into their lives and friendship group. You have introduced me to a great group of people and have given me a family overseas to spend Christmas and have so many good times with. I class you both as great friends and cannot wait to have many more. Thank you to the rest of the HSRG past and present: Aneeka, Lucie, Ainee, Thao, Kyran, El, Bithiah, Simon, Praveen, Sruthy and Lucas, and the Post-docs, Dr Adriana Pires Vieira, Dr Kasper Moller, Dr Yu Liu, Dr Peter Connolly, Dr Jacob Martin, Dr Mauricio Di Lorenzo and Dr Pouran Hudson along with Dr Jason Fogg for all great memories. I would also like to acknowledge Dr Thomas Becker (Curtin), Ching Goh (Curtin) and Dr Anita D'Angelo (ANSTO) from outside the HSRG for their technical support through my PhD.

Finally, I would like to thank Kate Fitzgerald for being the rock in my life I have needed and for being my number one fan. Without you in my life I do not think I could have finished my thesis and I look forward to many more adventures with you.

STATEMENT OF CONTRIBUTION

Chapter 1: The introduction chapter presenting the context and background to this project, including a literature review of relevant materials. All writing is original completed by myself with corrections and suggestions from Assoc. Prof. Mark Paskevicius, Dr Terry Humphries, and Prof. Craig Buckley.

Chapter 2: The experimental and methods chapter providing a detailed overview of all chemicals used, synthetic methodology and characterisation techniques. This is fully original work by myself with corrections and suggestions from Assoc. Prof. Mark Paskevicius, Dr Terry Humphries, and Prof. Craig Buckley.

Chapter 3: This chapter presents the published work "Investigating the potential of alkali metal plumba-*closo*-dodecaborate ($B_{11}H_{11}Pb^{2-}$) salts as solid-state battery electrolytes" (T. A. Hales, K. T. Møller, T. D. Humphries, A. M. D'Angelo, C. E. Buckley and M. Paskevicius, *J. Phys. Chem. C*, 2023, **127**, 949–957.) which was written by myself with revisions made by all co-authors. Supplementary Information can be found in Appendix A. The contributions of each author can be found in Appendix D. (https://doi.org/10.1021/acs.jpcc.2c07226).

Chapter 4: This chapter presents the published work "Stannaborates: tuning the ion conductivity of dodecaborate salts with tin substitution" (T. A. Hales, A. M. D'Angelo, K. T. Møller, C. E. Buckley, T. D. Humphries and M. Paskevicius, *Phys. Chem. Chem. Phys.*,(Advance Article)) which was written by myself with revisions made by all co-authors. Supplementary Information can be found in Appendix B. The contributions of each author can be found in Appendix D. (https://doi.org/10.1039/D3CP03725H)

Chapter 5: This chapter presents the paper "Monovalent heavy metal substituted closo-dodecaborate ($B_{11}H_{11}M^-$) (M = Sb, Bi) salts as potential solid-state ion conductors" which was

written by myself with revisions made by all co-authors Supplementary Information can be found in Appendix C. The contributions of each author can be found in Appendix D.

Chapter 6: This chapter presents the concluding remarks and future suggested work based on this thesis. All writing is original completed by myself with corrections and suggestions from Assoc. Prof. Mark Paskevicius, Dr Terry Humphries, and Prof. Craig Buckley.

ABSTRACT

The world is heading towards a global warming crisis, world temperature is increasing, due in part to the use of fossil fuels as the major energy source. The prevalence and importance of improved battery technologies are only going to increase as the world switches to intermittent renewable energy sources from the incumbent fossil fuels. Modern-day lithium-ion batteries have been used as large scale energy storage devices, however, as the fire at the Victorian Big Battery in 2021 has shown, there are major safety issues around the large amounts of highly flammable solvents used in liquid electrolytes. One way to avoid this is by using a solid-state electrolyte leading to a fully solid-state battery. Research into this technology is in its infancy, however, there are some commercial solid-state batteries, for example, the Toyota solid-state batteries.

There are many different types of materials that have been developed as solid-state ionic conductors and this project will focus on using cluster borohydride salts as potential solid-state ion conductors. This class of compounds has previously shown excellent ion conductivity, with the mono-carborane salts ($CB_{11}H_{12}^-$) showing superionic conductivity near room temperature. This project focusses on developing other substituted dodecaborate salts with the aim of creating materials with similar ion conductivity to the incumbent ionic liquid at room temperature. Lead, tin, bismuth and antimony will be substituted into the 12-vertex dodecaborate anion, paired with group 1 alkali metals and these novel salts will be characterised with a view to being potential solid-state electrolytes for battery applications.

Group 1 plumba-*closo*-dodecaborate salts were synthesised from trimethylammonium nido-undecaborate as confirmed using Fourier-Transform Infra-red (FTIR) and Nuclear Magnetic Resonance (NMR) spectroscopies. These anions have a lead atom within the 12-vertex cage, which creates a dipole and anisotropy in the divalent anion, similar to $CB_{11}H_{12}^-$ salts. $Li_2B_{11}H_{11}Pb \cdot xH_2O$ shows superionic conductivity up to ~ 7 mS cm^{-1} at 120 °C, which is comparable to $LiCB_{11}H_{12}$. However, at temperatures above 120 °C, dehydration of the material causes a reduction in the ionic conductivity performance. This observation is reinforced by Synchrotron-Radiation X-Ray Diffraction (SR-XRD) studies, where a change in crystal structure is determined. The sodium and potassium salts show moderate performance

as ionic conductors. Despite the plumba-borate salts being inferior to carboranes in terms of ionic conductivity, they are an improvement on the unsubstituted $B_{12}H_{12}{}^{2-}$ salts.

A tin substitution into the closo-dodecaborate anion ($B_{11}H_{11}Sn^{2-}$) was also undertaken from $Me_3NHB_{11}H_{14}$. This anion is polar, however, smaller than $B_{11}H_{11}Pb^{2-}$ anion, with the hypothesis that this will improve the conductivity of the material. $Li_2B_{11}H_{11}Sn$ shows high ionic conductivity of $\sim$ 8 mS cm^{-1} at 130 °C, similar to the state-of-the-art $LiCB_{11}H_{12}$ at these temperatures. $Na_2B_{11}H_{11}Sn$ also reaches superionic conductivity at 170 °C, but $K_2B_{11}H_{11}Sn$ exhibits moderate conductivity. The stannaborate salts do not show the required performance at room temperature, however they do show potential compared with the $B_{12}H_{12}{}^{2-}$ salts demonstrating that electrostatically polar anions may be advantageous for ionic conductivity.

Group 1 stiba- and bisma-*closo*-dodecaborate salts were successfully synthesised as confirmed by NMR and Raman spectroscopies. These anions show electrostatic charge distributions similar to the best performed borohydride salts and are monovalent akin to the carborane salts. $NaB_{11}H_{11}Bi$ and $NaB_{11}H_{11}Sb$ show superionic conductivity above 140 and 90 °C and up to maximum of 2 x 10^{-3} S cm^{-1} at 170 °C and 1 x 10^{-2} S cm^{-1} at 150 °C, respectively. This performance is far better than the lithium salts, which not only show low ionic conductivity $\leq$ 10^{-8} S cm^{-1} but do not reach superionic conductivity even at elevated temperatures.

The ion conductivities achieved by these novel alkali metal *closo*-borate salts have been shown to be promising, due to the superionic conductivity of many of the materials. However, this conductive performance was only achieved at high temperatures so cannot be used in every day battery technologies, alongside using more expensive materials during synthesis and low chemical stabilities than the current contemporaries. However, these materials show promise and further investigation in substituted metallo-borane salts as potential solid-state battery materials is warranted.

TABLE OF CONTENTS

LIST OF FIGURES

LIST OF TABLES

Chapter 1

Introduction

CHAPTER 1 - INTRODUCTION

1.1 World Energy Crisis?

The world is at a tipping point. The effects of global warming are being seen around the world with melting ice caps leading to rising sea levels causing frequent flooding to densely populated, low lying areas.[1,2] Furthermore, the amount of weather-related catastrophes are increasing, for example, the increase in precipitation rates during tropical cyclones.[3] The damage and destruction of global warming is not only seen by humans, it has pillaged other living organisms around the world. Sea acidity levels are increasing which has a catastrophic effect on marine life, this is no more apparent than the health of corals off the coast of Australia, where death and bleaching of these colourful and crucial organisms has occurred.[4]

Global warming is not the only phenomenon seen in the 21st century. The technological age is in full swing with booming populations and industrialisation leading to increased energy demand around the world.[5,6] This is partially due to improved medical technology, such as drugs and surgical techniques, curing previously deadly conditions leading to higher life expectancies worldwide.[7] Digitalisation of the world leads to the increased reliance of electrical devices and therefore energy is needed to fuel the world and the daily norm we see today.[8]

1.1.1 Fossil Fuels

The usage of increasing amounts of energy is not inherently a bad thing for global warming and the world in general. The major issue is the source of this energy and what the bigger picture is from using energy from this source. Nowadays, the largest source of energy is from burning non-renewable fossil fuels such as coal, oil or natural gases, for example methane and propane.[9] They are a wonderful resource in the fact they have a large energy density, so burning a small amount releases a large amount of energy. They are extracted from within

the Earth's crust and have been formed by the pressurised decomposition of natural species, such as animals and plants, over millions of years.[10] Due to the length of time taken for fossil fuels to form, they are considered a finite resource.[11] However, the greatest issue with using fossil fuels as an energy source is the fact they emit greenhouse gases, for example, carbon dioxide (CO_2), which release 36.1 $GtCO_2$ per year into the atmosphere.[12] A greenhouse gas is a gas that absorbs UV radiation and must contain a heteronuclear bond as homonuclear bonds do not absorb UV radiation.[13] An increased amount of greenhouse gases in the atmosphere leads to increased global warming as the Sun's energy cannot escape as easily from the Earth's atmosphere after reflecting off its surface.[13] This extra retention of energy within the ionosphere leads to increased global air temperatures and global warming. Fossil fuels are not the sole source of energy used to power the world. Other "greener" sources such as nuclear energy are also used but they also possess their own potential health hazards, for example, the disposal of highly toxic radioactive waste.[14]

1.1.2 Renewables

However, there are other energy resources that can help fuel the world that do not lead to the emission of large amounts of greenhouse gases or the dumping of toxic waste. These use the natural phenomena seen globally, such as the weather, and harness their power and convert them into an energy source to fuel the world.[15] Furthermore, they are considered renewable, meaning that they are not finite and can be used without limitation.

One example is the use of solar power. The energy released from the sun is used to power the Earth in two main ways. Firstly, photovoltaic (PV) cells can be used to convert the sun's rays into electrical energy which can power electrical devices.[16] Secondly, the energy can be converted into heat using an array of mirrors to focus the energy at a specific point which generates extremely high temperatures.[17] Another source is using wind power to drive turbines that drives a generator, creating electrical energy for use.[18] There are also many more renewable sources of energy, for example, hydroelectric power.[19]

There is one major drawback for the use of renewables to power the world and that is because they are intermittent sources. The sun does not shine all day, nor does the wind blow

consistently. Studies have shown that these resources can power the world with the addition of one vital component; an energy storage device. This allows energy to be stored and accumulated when there is a surplus and then deployed when there is a shortage.

1.2 Energy Storage

Energy storage devices are vastly abundant the world round and come in different shapes, sizes and designs in order to fit their purpose. There are three main types of energy storage; mechanical, thermochemical and electrochemical. Mechanical energy storage takes advantage of kinetic or gravitational potential by using energy to, for example, compress air.[20] When the energy is needed to be used, the pressure is released, the energy is released and available to be used on demand.

1.2.1 Thermochemical Energy Storage

Thermochemical energy storage uses heat to power a reversible endothermic chemical reaction. This heat can be provided from many sources, including concentrated solar power (CSP). When the energy is needed to be used the reverse reaction is encouraged, leading to an exothermic chemical reaction, hence releasing energy.[21,22] Examples of this are using materials such as metal hydrides or metal carbonates.[17,23] The metal hydrides, for example, are heated to a high temperature ($\sim$ 1000 °C), releasing hydrogen gas and the metal. The hydrogen gas is stored and then reintroduced when needed into the system, exothermically reacting with the metal when heat is desired to power a heat engine and produce electricity.

1.2.2 Electrochemical Energy Storage

Electrochemical energy storage devices, or as they are more colloquially known, batteries, are the most common type of energy storage technology and are used to power a great quantity of electrical items from cars to mobile phones.[24] The first battery was developed by Volta in the early 19th Century and the concept has been built on ever since.[25] A battery contains three main components; a positively charged cathode, a negatively charged anode and a liquid electrolyte when supplying power.[26] Energy is released from a battery from oxidation-reduction (redox) reactions at the respective electrode (reduction at cathode, oxidation at anode).[27] The liquid electrolyte allows ions but not free electrons to be dissolved within the liquid to be transported to the electrodes and under these redox reactions. This energy is in the form of direct current (DC), which is used to power many electrical items.[27] There are many different types of battery such as lead-acid and nickel-cadmium batteries.[28] Lead-acid batteries (LAB) are commonly used, however, the lithium ion battery (LIB) has a similar usage (LAB - 49.9% vs LIB - 45.7%) with projections to take over as the most widely used in the future.[29]

1.3 Lithium ion Batteries

Lithium ion batteries (LIB) have been developed for over 40 years and could take a key role in helping to overcome the world energy crisis.[30] They are lightweight, highly functional batteries that are also high energy density (700 WhL^{-1}), so a large amount of energy can be stored in a small and light battery.[31] The battery contains three main components; a metal oxide cathode (such as $LiMnO_2$ or $LiCoO_2$), a graphite anode and a lithium based liquid electrolyte such as $LiPF_6$ in ethylene carbonate (Figure 1.1).[27,31] Li^+ ions travel through the electrolyte to the cathode where they are reduced, releasing energy. This creates a charge imbalance that is corrected by electron travel through the circuit, providing electricity for power applications.
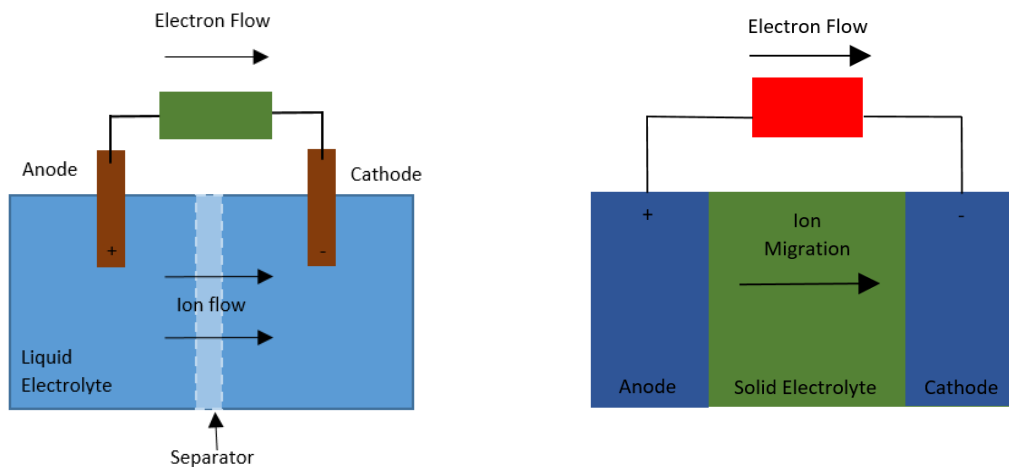
Figure 1.1. A comparison between cells with liquid and solid-state electrolytes batteries.

Equations 1.1-1.3 show the respective half and full cell equations for a generic lithium ion battery. LIBs are rechargeable due to the reversibility of the reactions at both electrodes.[27,31] The input of a DC voltage through the cell drives the reverse chemical reactions, thus returning the cell to its original state.[30] This allows the cells to be reused and as a result are a device to store renewable energy.

One drawback is the degradation of performance over time. In one study after 1000 cycles, these cells will begin to wear, and the capacity of the battery will decrease by $\sim 20\%$.[26] A major disadvantage of lithium ion batteries is the use of a highly flammable and volatile solvent such as ethylene carbonate.[32] Furthermore, the use of a liquid reduces their ability to function outside of their operating window due to freezing and boiling.[33] Also, solid lithium cannot be used as the anode to make the batteries inexpensive and perform at an improved voltage window.[34] The way to avoid these issues is using a full solid state construct including a solid state electrolyte (Figure 1.1).

Half Cell Equation at the cathode:

(1.1)

$$LiMO_2 + xLi^+ + xe^- \leftrightarrow Li_{1+x}MO_2$$
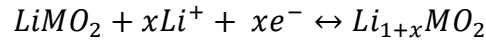
where M = metal

Half Cell Equation at the anode:

(1.2)

$$LiC_6 \leftrightarrow C_6 + Li^+ + e^-$$
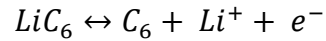
where C_6 = graphite

Full Cell Equation:

(1.3)

$$LiMO_2 + Li_xC_6 \leftrightarrow Li_{1+x}MO_2 + C_6$$
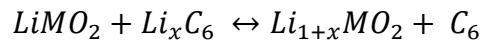
1.4 Solid State Electrolytes

Solid state electrolytes are seen as the future of battery technology as they remove some of the negative features of the current market leader, the lithium ion battery.[35] By definition, they remove the need for the highly flammable and volatile liquid electrolyte making them an inherently much safer option than traditional liquid electrolytes. Furthermore, they can have a higher energy density so they will theoretically have a longer time span between recharges (1200 Wh L^{-1}).[36] A full solid state construction allows the use of a pure metal anode as one of the electrodes. Using a lithium metal anode (LMA) with traditional liquid electrolytes can cause short circuiting due to the growth of lithium dendrites from the metal anode. Dendrites are the deposition of lithium metal on the anode from the reduction of Li^+ ions in the electrolyte. Whilst these dendrites can exist using solid-state electrolytes, there are techniques such as using solid electrolyte separators. This allows the use of LMAs as they have a much higher energy density then standard graphite anodes (1200 vs 770 WhL^{-1}).

Furthermore, solid-state electrolytes are compatible with the cathode materials used with liquid electrolytes which reduces the amount of technological cost in developing the cathode. However, there are drawbacks to the use of solid materials as electrolytes. Firstly, they have inherently low ion conductivity in comparison to their liquid contemporaries. Currently liquid electrolytes have an ion conductivity of ~ 10 mS cm^{-1} at 293 K whereas the solid alternatives are much lower.[37] Furthermore, the synthesis of the solid materials used are often very expensive due to the cost of starting materials or synthetic conditions.[38,39] In addition, the solid-solid interface gives poorer electrolyte-electrode contact than their liquid alternatives and also needs to be addressed.[40]

1.4.1 Solid ion conductors

Materials in the solid state do not allow for the free movement of ions in the same way that materials in the liquid state do.[41] In traditional batteries, ions can freely travel through a liquid to each electrode with minimal impact of their respective counter ion.[42] In a solid lattice of ions, this is not the case, however ions must still be able to flow in order to be oxidised and reduced at the respective electrode.[43] This requires a special design of the solid material to allow ionic migration throughout its crystal lattice without electronic conduction. Ion conductors have been known since the 19th century, and materials have been developed and refined so that they have ion conductivity performance similar to the incumbent liquid electrolyte, LiBF$_4$/EMIBF$_4$.[25,44] There are various methods for ion conductivity depending on the structure of the material.[45] The vacancy mechanism uses Schottky defects (ion vacancies within the crystal structure) to allow ions to hop into available ion sites (Figure 1.2). This creates a new vacancy allowing a further ion to hop and this phenomenon repeats, allowing ions to transport through the solid.[46] The interstitial mechanism uses Frenkel defects (over population of ion sites).[47] This allows ions to displace neighbour ions in adjacent available sites, thus allowing diffusion of these ions through the solid lattice. In the cation conduction mechanism, which is seen in this project, cations are usually transported through a static ionic lattice. However, a recent study has unveiled additional anionic rotation within the crystal structure known as the "paddle-wheel" mechanism as the conductive method within certain high performing borate cluster materials.[37,48] Cations move through the paddle-wheels

formed by the anionic rotation and compounds which exhibit this phenomenon have been shown to have high ion conductivity.
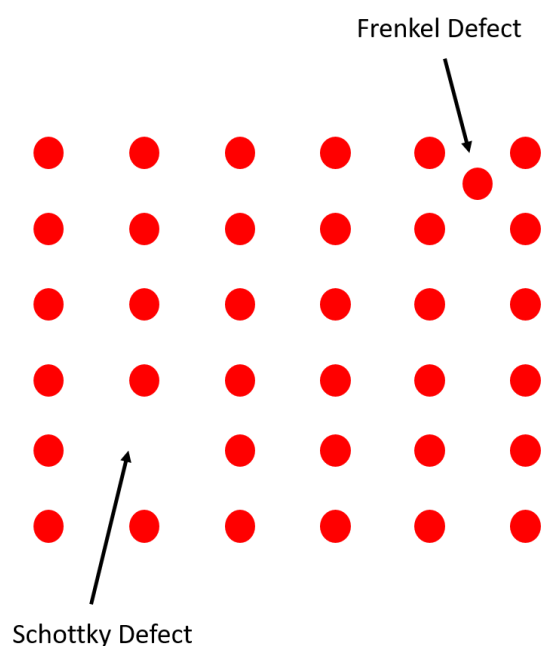
Figure 1.2. A lattice depicting Schottky and Frenkel defects

1.4.2 Current Solid State Electrolytes

There are different types of compounds which have shown promise as possible solid state electrolytes as seen in Table 1.1. Perhaps the more prevalent is the use of inorganic solids such as sulphides (e.g. $Li_{10}GeP_2S_{12}$) and silicates (e.g. $Na_3Zr_2PSi_2O_{12}$).[37,49–51] They show high promise due to the high lability of the respective lithium and sodium ions. These have high ion conductivity, especially at high temperature (> 100 °C) and are chemically stable. Inorganic solids such as sulfides are already being used commercially alongside a lithium metal and lithium nickel manganese cobalt oxide electrodes, however, these compounds require a high synthesis temperature or use of ball milling which lead to sample impurities and irregularities not suitable for mass production.[52] Other solid state batteries use solvent-free salts and polymers as the electrolyte, but these materials often have low room temperature ion conductivity and see degradation at the electrolyte cathode interface.[53] They work by the migration of ions through the polymer chain between the two electrodes.[54] An example of

this is shown by Yue *et. al.* where a mixture of polymers are used in the electrode to afford high ion conductivity levels.[55]

Figure 1.3 shows a comparison between different types of materials as potential solid-state electrolytes. Sulfides have been proposed as potential electrolytes due to their superionic conductivity and high thermal stability, allowing prospective batteries to be able to run at a wide range of temperatures.[56] However, these compounds tend to show low chemical stability, leading the release of toxic H_2S gas.[57] Metal oxides also show high ion conductivities and thermal stability alongside excellent oxidation and reduction resistance.[39] However, these compounds show poor interfacial compatibilities and extreme temperature synthetic methods.[58] Polymers overcome these interfacial difficulties, however, show low ion conductivities so are usually unsuitable as potential electrolytes.[40] Hydroborates overcome a wide range of the drawbacks found with the other compounds. They show superionic conductivities and are compatible with a range of alkali metals.[59,60] Their drawbacks include synthetic methods which are not well refined and developed. This project aims to develop novel methods in synthesising new hydroborate salts as potential solid-state ion conductors.
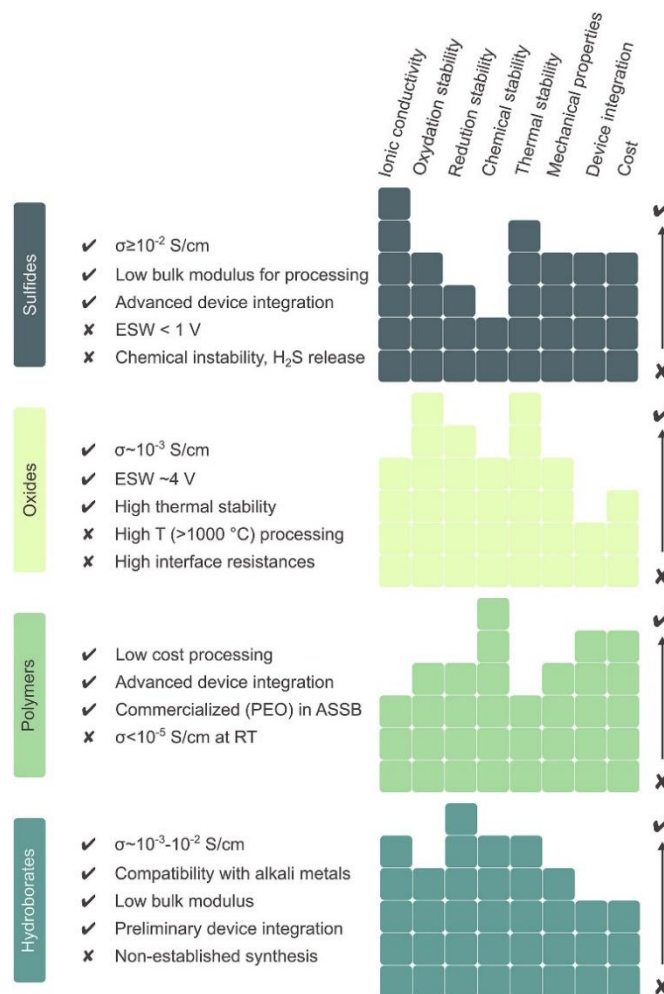
Figure 1.3. The advantages and disadvantages of various materials as potential solid-state electrolytes.[61] This figure is reused from the reference provided and permission to use this figure is shown in Appendix E.

Sodium ion batteries are a promising alternative to lithium ion batteries due to the much higher abundance of sodium (2.83 %) than lithium (0.01 %) on Earth and as a result sodium ($150 per tonne) is much cheaper than lithium ($5000 per tonne).[62] The abundance and price of sodium is the primary advantage of sodium ion batteries and drives further development into electrode technologies. Currently, there is a commercial sodium battery using a solid-state electrolyte, however, this uses elevated temperatures (~ 300 °C) and molten sodium and sulfur electrodes.[63] This requires a high level of safety precautions to use this technology implying it is not viable to be widely used.

Table 1.1. Examples of some existing solid-state ion conductors

Compound	Material Type	Ion Conductivity at 25 °C (S cm^{-1})	Max. Conductivity (S cm^{-1}) and Temperature (°C)	Problems	Ref
$Ag_2B_{12}H_{12}$	Inorganic salt	2×10^{-4}	3×10^{-1} at 220 °C	Wrong cation – Ag is very expensive	[64]
$Li_{10}GeP_2S_{12}$	Ceramic	2.8×10^{-3}	1×10^{-1} at 110 °C	Expensive to manufacture	[49,50]
$Li_2B_{12}H_{12}$	Inorganic salt	1×10^{-7}	2×10^{-4} at 180 °C	Low Conductivity at room temperature	[65]
$LiCB_{11}H_{12}$	Inorganic salt	1×10^{-4} (at 40 °C)	5×10^{-1} at 160 °C	High manufacture cost	[66]
LiN_3	Inorganic salt	1×10^{-3}	8×10^{-2} at 270 °C	Extremely hygroscopic	[67,68]
$Li\text{-}\beta''\text{-}Al_2O_3$	Doped inorganic solid	3×10^{-3}	-	Extremely hygroscopic and difficult to prepare dry	[67]
$Na_{10}GeP_2S_{12}$	Ceramic	1.2×10^{-5}	1×10^{-3} at 130 °C	Low ion conductivity at room temperature and expensive to manufacture	[69]
$Na_2B_{12}H_{12}$	Inorganic salt	1×10^{-7}	1×10^{-1} at 270 °C	Low conductivity at room temperature	[66]
Na_3PS_4	Inorganic solid	3.5×10^{-3}	2×10^{-2} at 270 °C	Defects introducing due to ball milling synthesis	[70]
$Na_3Zr_2PSi_2O_{12}$	Ceramic	1×10^{-3}	2×10^{-1} at 300 °C	High temperature during synthesis	[37,51]
$NaCB_{11}H_{12}$	Inorganic salt	5×10^{-5}	2×10^{-1} at 120 °C	High manufacture cost	[38,66]
PAN - $Li_{0.33}La_{0.55}TiO_3$	Polymer	9.56×10^{-6}	9×10^{-5} at 140 °C	Low conductivity	[71]

PEO - (LiTFSI)	Polymer	1×10^{-6}	1×10^{-3} at 80 °C	Low conductivity at room temperature	40

1.4.3 Ion Conductivity

Ion conductivity (σ in S cm^{-1}) is the measurement that determines a compounds ability to conduct ions within a solid material.[72] The mechanism by which these materials conduct varies depending on the material and these mechanisms are discussed above. Ion conductivity generally improves with increased temperature for two reasons. Firstly, as temperature increases, the entropy of the material increases and as a result the number of defects is increased which improves conductivity. Also, the number of molecules with the activation energy to diffuse through the material is increased at higher temperature by Boltzmann's law and thus higher conductivity.[73,74] However, large increases in ion conductivity can also be observed due to a polymorphic phase transitions which can form structures which are more favourable for ion migration.[75] Figure 1.4 shows the ion conductivity against temperature of a selection of different lithium and sodium compounds. They show that a multitude of different chemistries can give super ion conductivity (σ > 1 mS cm^{-1}). One family of compounds with particular promise are cluster boron compounds.[37]
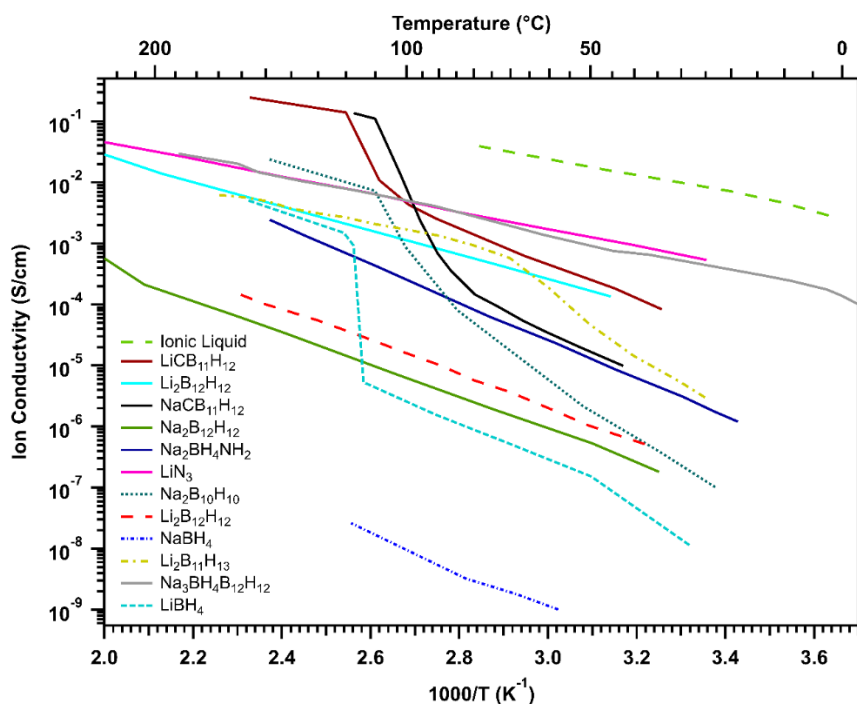
Figure 1.4. Ion conductivity of various lithium and sodium ion conductors against temperature.[37,66,76–79]

1.5 Boron

Boron is the lightest group 13 element with an atomic number of 5. The electron configuration for boron is $1s^2\,2s^2\,2p^1$ meaning it has just three valence electrons which it readily bonds with itself and other elements using covalent bonds.[80] Boron was discovered as a component of the mineral borax ($Na_2B_4O_7$) but was not isolated until the late 18th century by Sir Humphrey Davey.[81] Boron has two major stable isotopes ^{10}B and ^{11}B at approximately a 20:80 ratio leading to an atomic number of 10.811. Boron forms a wide range of compounds namely oxides, simple hydrides, sulfides and halides, where it has a formal +3 oxidation state.[80] However, elemental boron is rare as it is difficult to synthesise and does not occur naturally.[82] Boron is an inherently electron deficient element as many neutral molecules containing boron leave boron having only six valence electrons and not the normal stable octet.[80] As a result, boron containing neutral molecules are reactive, for example, the simplest boron containing molecule, BH_3, reacts violently in air and is only stable in an electron donating solvent such as tetrahydrofuran (THF) or diethyl ether or as a dimer.[80]

1.5.1 Three centre – Two electron bonding

Diborane (B_2H_6) was discovered by Stock in 1943 and is an extremely reactive and toxic gas but its bonding is very interesting and unique to group 13 elements and their compounds.[83] Regular covalent bonding shares two electrons between two atomic centres (2c-2e bonding), however, diborane does not contain enough electrons to do the conventional 2c-2e bonds.[83] Instead it shares the electron density of two electrons over three atomic centres (3c-2e bonding). This allows each boron atom to have a *pseudo* full octet.[84,85] In effect, it forms atom bridges (e.g. H or Cl) between the boron atoms (Figure 1.5) where each bridge contains just two electrons. This phenomenon is found throughout group 13 compounds such as Al_2H_6 and also allows the formation of boron cluster molecules.[85]
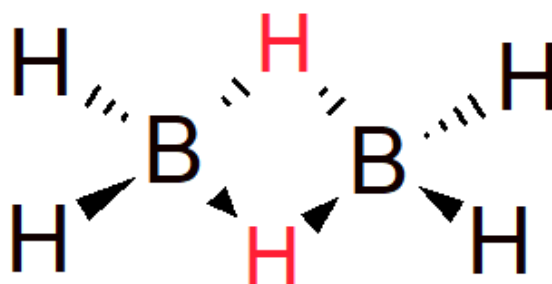
Figure 1.5. The bonding within B_2H_6 – red hydrogen atoms indicate bridging hydrogen which undertake the 3 centre – 2 electron bonds.

1.6 Cluster Boron Compounds

Complex boron-hydrogen compounds, or boranes, have been known for over 70 years with one of the most well-known and used compounds, decaborane ($B_{10}H_{14}$) discovered in 1948 by Lipscomb, for which he won the Nobel prize for chemistry in 1976.[84,86] These compounds can be molecular but are also commonly found as anions. Complex boranes form a variety of three-dimensional multi-vertex polyhedra, which can be classified into four different types as discussed below. These compounds follow Wade's rules to diagnose their structures.[87]

1.6.1 Wade's Rules

Wade's rules were developed by Wade in 1971 and they diagnose their structure by calculating the total number of skeletal electron pairs depending on the number of available electrons for bonding within the structure (Figure 1.6).[87] *Closo* (closed) boranes have no missing vertices and have the general formula B_nH_{n+2} for molecular compounds. A relative example is the lithium and sodium salts of the dodecahydrido-*closo*-dodecaborate dianion ($B_{12}H_{12}^{2-}$) which show high ion conductivity. *Nido* (nest-life) boranes have one missing vertice from a perfect polyhedron and have the formula B_nH_{n+4}, *nido*-undecaborate anion ($B_{11}H_{14}^{-}$) is a widely used starting material for the synthesis of many substituted borates. *Arachno* (web-life) boranes are missing two vertices and *hypho* boranes are missing three, however they are only found in adducts and do not have any stable compounds by themselves.

| *Closo-* | *Nido-* | *Arachno-* | *Hypho-* |
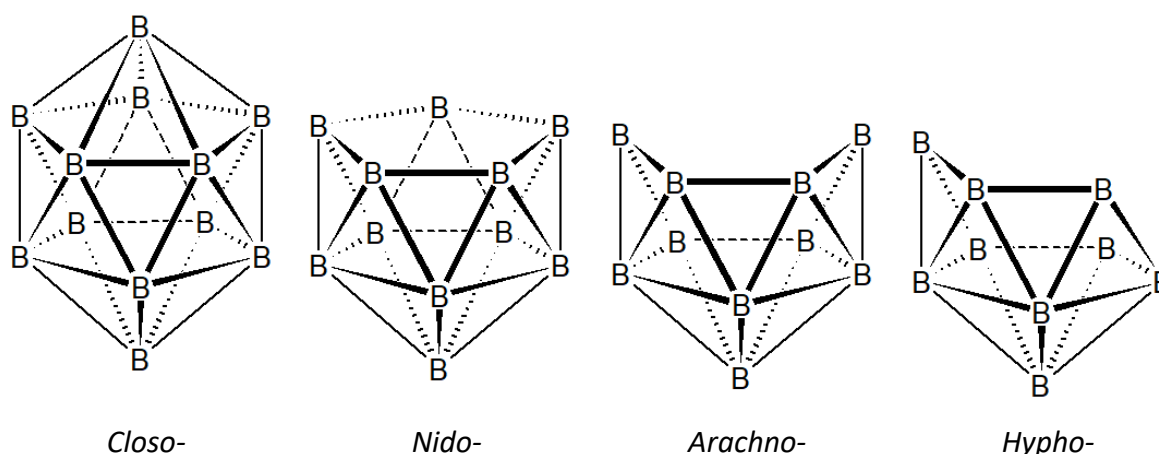
Figure 1.6. Wade's Rules using $B_{12}H_{12}^{2-}$ as the *closo* compound. Note – these examples have been used to show the structure and are not necessarily stable in nature.

1.7 Substituted Cluster Boron Compounds

1.7.1 Carborane

Substituted cluster boron compounds involve introducing one or more heteroatoms into the boron cage, usually to make a *closo* structure, although *nido* structure like nido-7,9-$C_2B_9H_{12}^-$ are also known.[88] The dodecahydrido-*closo*-carbadodecaborane anion ($CB_{11}H_{12}^-$), or carborane for short, is greatly researched with many different synthetic routes being proposed.[38,89,90] The carborane is analogous to the $B_{12}H_{12}^{2-}$ anion, however, a single B-H unit has been replaced with a C-H unit, reducing the overall charge of the anion because the of the addition proton (+1 charge) in a carbon atom in comparison to boron. Most of the syntheses for $CB_{11}H_{12}^-$ start from $B_{10}H_{14}$ which is extremely toxic, however, a safe, cheaper synthesis has been developed by Berger *et. al.*[38] This synthesis starts from $NaBH_4$ via $Me_3NHB_{11}H_{14}$ using common laboratory reagents, for example, sodium hydroxide and potassium carbonate and using solvents, such as diethylene glycol dimethyl ether (diglyme) and tetrahydrofuran (THF).

The insertion of a heteroatom removes a degree of symmetry within the carborane anion in comparison with the unsubstituted $B_{12}H_{12}^{2-}$ dianion. This greatly improves the ion conductivity of the lithium and sodium salts of the carborane due to beneficial phase transitions and molecular dynamics (paddle-wheel) leading to improved conductivity.[48] Furthermore, these carborane salts undergo a phase transition at $\sim$ 100 °C, which shows superionic levels of ion conductivity with a maximum of 5 x 10^{-1} S cm^{-1} at 160 °C for $LiCB_{11}H_{12}$ and 2 x 10^{-1} S cm^{-1} at 120 °C for $NaCB_{11}H_{12}$, respectively.[38] This compares to 2 x 10^{-4} at 180 °C 1 x 10^{-1} S cm^{-1} at 270 °C for unsubstituted $Li_2B_{12}H_{12}$ and $Na_2B_{12}H_{12}$.[65,66] In the high temperature polymorph, cation migration is aided by the internal rotation of the carborane anions as mentioned above.

1.7.2 Heavy Metal Substituted Boron Compounds

Carbon is not the only element that has been successfully integrated into boron cage-like anions. Heavy metals such as lead (Pb) and tin (Sn) have also been inserted into *nido* cages to form stable *closo* 12-vertex structures. The syntheses were published by Chapman *et. al.* in 1992 and involve the isolation for *plumba-* and *stanna*-dodecaborate salts ($B_{11}H_{11}Pb^{2-}$ and $B_{11}H_{11}Sn^{2-}$).[91] These salts were only isolated with bulky organic cations such as the methyltriphenylphosphonium ($MePh_3P^+$) and tetramethylammonium (Me_4N^+) cations. Insertions of other elements such as germanium ($B_{11}H_{11}Ge^{2-}$), bismuth ($B_{11}H_{11}Bi^-$) and antimony ($B_{11}H_{11}Sb^-$) have also been synthesised, again with bulky organic cations.[92]

The synthesis for all of these insertions involves trimethylammonium *nido*-undecaborate ($Me_3NHB_{11}H_{14}$) as the starting material. Each synthesis has slightly different reagents, however, they all follow the same overriding principles. They treat $B_{11}H_{14}^-$ with a base, to remove the acidic hydrogen on the cation and also remove hydrogen on the anion to make it more reactive, and a heavy metal halide (e.g. $PbCl_2$). The resulting solution is reacted with a bulky cation and the product is insoluble in the respective solvents so the salts are able to be isolated.[91,92] Alkali metal salts of these anions have not previously been synthesised, as a result, the knowledge of these materials is limited.

$B_{11}H_{11}Sn^{2-}$ anions have been used as ligands for transition metals used in chemical catalysis.[93,94] These anions have been shown to be highly labile ligands with the ability to coordinate to a variety of metals and have been shown to activate the metal complex for isonitrile insertion and hydroformylation.[95] Furthermore, they cause the dimerisation of gold complexes.[93] However, further research in $B_{11}H_{11}Pb^{2-}$, $B_{11}H_{11}Sb^-$ and $B_{11}H_{11}Bi^-$ compounds has not been performed. Consequently, any electrochemical probing has not been performed and will be the basis of this project. These materials have been chosen for the project due to their similarity to the *mono*-carborane ($CB_{11}H_{12}^-$) as substituted *closo*-dodecaborate anions. The materials probe in this research also contain a dipole and their increased size and therefore cation-anion size disparity is hoped to show increased performance as possible solid-state ion conductors.

1.8 Research Questions, Aims and Objectives

The primary research question is to investigate the proficiency of heavy metal substituted cluster borate salts as potential solid-state electrolytes. Further questions this thesis will tackle include the effect of size and polarity of ions on their performance as ion conductors. Furthermore, what is the effect of the valency of these heavy metal substituted anions on the respective performances.

To address these research questions this thesis will investigate the potential of group 14 and 15 heavy metal substituted borohydride cluster salts as solid state electrolytes in battery systems using the following methodology.

- Synthesise a library of *plumba-* ($B_{11}H_{11}Pb^{2-}$), *stanna-* ($B_{11}H_{11}Sn^{2-}$), *bisma-* ($B_{11}H_{11}Bi^-$) and *stiba-closo*-dodecaborate ($B_{11}H_{11}Sb^-$) salts with different metal cations.

- Characterise the materials using a plethora of spectroscopic techniques such as Nuclear Magnetic Resonance (NMR), Fourier Transform Infra-red (FTIR), Residual Gas Analysis - Mass Spectroscopy (RGA-MS) and Differential Scanning Calorimetry (DSC).

- Ascertain the crystal structure of the samples using Synchrotron Radiation X-ray Diffraction (SR-XRD). *In-situ* X-ray diffraction will be used to discover any phase changes that occur at elevated or reduced temperature.

- Measure the performance of the material as potential solid state electrolytes using Electrochemical Impedance Spectroscopy (EIS) to measure ion conductivity. Other electrochemical techniques such as cyclic voltammetry (CV) and linear sweep voltammetry (LSV) will be used to ascertain the oxidative stability of the materials.

1.9 References

1   W. Ruebsam, B. Mayer and L. Schwark, *Glob. Planet. Change*, 2019, **172**, 440–453.

2   M. Taherkhani, S. Vitousek, P. L. Barnard, N. Frazer, T. R. Anderson and C. H. Fletcher, *Sci. Rep.*, 2020, **10**, 1–17.

3   M. Liu, G. A. Vecchi, J. A. Smith and T. R. Knutson, *npj Clim. Atmos. Sci.*, 2019, **2**, 1–5.

4   M. Mies, R. B. Francini-Filho, C. Zilberberg, A. G. Garrido, G. O. Longo, E. Laurentino, A. Z. Güth, P. Y. G. Sumida and T. N. S. Banha, *Front. Mar. Sci.*, 2020, **7**, 1–13.

5   S. Lange, J. Pohl and T. Santarius, *Ecol. Econ.*, 2020, **176**, 106760.

6   B. J. van Ruijven, E. De Cian and I. Sue Wing, *Nat. Commun.*, 2019, **10**, 1–12.

7   P. Rajpurkar, E. Chen, O. Banerjee and E. J. Topol, *Nat. Med.*, 2022, **28**, 31–38.

8   J. Mitali, S. Dhinakaran and A. A. Mohamad, *Energy Storage Sav.*, 2022, **1**, 166–216.

9   A. Qazi, F. Hussain, N. A. B. D. Rahim, G. Hardaker, D. Alghazzawi, K. Shaban and K. Haruna, *IEEE Access*, 2019, **7**, 63837–63851.

10   M. K. Hubbert, *Science (80-.).*, 1949, **109**, 103–109.

11   N. Abas, A. Kalair and N. Khan, *Futures*, 2015, **69**, 31–49.

12   Z. Liu, Z. Deng, S. Davis and P. Ciais, *Nat. Rev. Earth Environ.*, 2023, **2022**, 2022–2023.

13   N. Borduas and N. M. Donahue, *The Natural Atmosphere*, Elsevier Inc., 2018.

14   M. D. Mathew, *Prog. Nucl. Energy*, 2022, **143**, 104080.

15   A. G. Olabi and M. A. Abdelkareem, *Renew. Sustain. Energy Rev.*, 2022, **158**, 112111.

16   K. Ranabhat, L. Patrikeev, A. A. Revina, K. Andrianov, V. Lapshinsky and E. Sofronova, *J. Appl. Eng. Sci.*, 2016, **14**, 481–491.

17   K. Williamson, K. T. Møller, A. M. D'Angelo, T. D. Humphries, M. Paskevicius and C. E. Buckley, *Phys. Chem. Chem. Phys.*, 2023, **25**, 7268–7277.

18 P. Gipe, *Wind Eng.*, 2004, **28**, 629–631.

19 A. M. Bagher, M. Vahid, M. Mohsen and D. Parvin, *Am. J. Energy Sci.*, 2015, **2**, 17–20.

20 A. V. Olympios, J. D. McTigue, P. Farres-Antunez, A. Tafone, A. Romagnoli, Y. Li, Y. Ding, W. D. Steinmann, L. Wang, H. Chen and C. N. Markides, *Prog. Energy*, 2020, **3**, 022001.

21 S. Balakrishnan, M. V. Sofianos, T. D. Humphries, M. Paskevicius and C. E. Buckley, *Phys. Chem. Chem. Phys.*, 2020, **22**, 25780–25788.

22 S. Balakrishnan, T. D. Humphries, M. Paskevicius and C. E. Buckley, *Int. J. Hydrogen Energy*, 2023, **48**, 30479–30488.

23 S. Balakrishnan, M. V. Sofianos, M. Paskevicius, M. R. Rowles and C. E. Buckley, *J. Phys. Chem. C*, 2020, **124**, 17512–17519.

24 M. Chen, Y. Zhang, G. Xing, S. L. Chou and Y. Tang, *Energy Environ. Sci.*, 2021, **14**, 3323–3351.

25 R. Cecchini and G. Pelosi, *IEEE Antennas Propag. Mag.*, 1992, **34**, 30–37.

26 G. Zubi, R. Dufo-López, M. Carvalho and G. Pasaoglu, *Renew. Sustain. Energy Rev.*, 2018, **89**, 292–308.

27 D. Solyali, B. Safaei, O. Zargar and G. Aytac, *Int. J. Energy Res.*, 2022, **46**, 17786–17812.

28 G. Marin-Garcia, G. Vazquez-Guzman, J. M. Sosa, A. R. Lopez, P. R. Martinez-Rodriguez and D. Langarica, in *2020 IEEE International Autumn Meeting on Power, Electronics and Computing, ROPEC 2020*, 2020, pp. 1–6.

29 Y. Zhao, O. Pohl, A. I. Bhatt, G. E. Collis, P. J. Mahon, T. Rüther and A. F. Hollenkamp, *Sustain. Chem.*, 2021, **2**, 167–205.

30 A. Yoshino, *Angew. Chemie - Int. Ed.*, 2012, **51**, 5798–5800.

31 M. Li, J. Lu, Z. Chen and K. Amine, *Adv. Mater.*, 2018, **30**, 1–24.

32 L. T. M. Le, T. D. Vo, K. H. P. Ngo, S. Okada, F. Alloin, A. Garg and P. M. L. Le, *J. Mol.*

Liq., 2018, **271**, 769–777.

33   J. Wang, Q. Zheng, M. Fang, S. Ko, Y. Yamada and A. Yamada, *Adv. Sci.*, 2021, **8**, 1–10.

34   T. Krauskopf, F. H. Richter, W. G. Zeier and J. Janek, *Chem. Rev.*, 2020, **120**, 7745–7794.

35   A. M. Bates, Y. Preger, L. Torres-Castro, K. L. Harrison, S. J. Harris and J. Hewson, *Joule*, 2022, **6**, 742–755.

36   R. C. Agrawal and G. P. Pandey, *J. Phys. D. Appl. Phys.*, 2008, **41**, 223001.

37   B. R. S. Hansen, M. Paskevicius, H. W. Li, E. Akiba and T. R. Jensen, *Coord. Chem. Rev.*, 2016, **323**, 60–70.

38   A. Berger, C. E. Buckley and M. Paskevicius, *Inorg. Chem.*, 2021, **60**, 14744–14751.

39   N. Ohta, K. Takada, I. Sakaguchi, L. Zhang, R. Ma, K. Fukuda, M. Osada and T. Sasaki, *Electrochem. commun.*, 2007, **9**, 1486–1490.

40   Y. Zhao, R. Tao and T. Fujinami, *Electrochim. Acta*, 2006, **51**, 6451–6455.

41   J. A. Barker and D. Henderson, *Rev. Mod. Phys.*, 1976, **48**, 587–671.

42   D. Roberts, *Am. J. Phys.*, 1983, **51**, 829–831.

43   J. Nanda, C. Wang, P. Liu and G. Editors, 2018, **43**, 740–745.

44   R. Hagiwara and J. S. Lee, *Electrochemistry*, 2007, **75**, 23–33.

45   H. Yang and N. Wu, *Energy Sci. Eng.*, 2022, **10**, 1643–1671.

46   G. Guisbiers, *J. Phys. Chem. C*, 2011, **115**, 2616–2621.

47   W. Schilling, *J. Nucl. Mater.*, 1994, **216**, 45–48.

48   Z. Zhang and L. F. Nazar, *Nat. Rev. Mater.*, 2022, **7**, 389–405.

49   L. Schweiger, K. Hogrefe, B. Gadermaier, J. L. M. Rupp and H. M. R. Wilkening, *J. Am. Chem. Soc.*, 2022, **144**, 9597–9609.

50   S. Song, Z. Yan, F. Wu, X. Zhang and Y. Xiang, *IOP Conf. Ser. Earth Environ. Sci.*, 2020, **461**, 0–8.

51   A. Jalalian-Khakshour, C. O. Phillips, L. Jackson, T. O. Dunlop, S. Margadonna and D. Deganello, *J. Mater. Sci.*, 2020, **55**, 2291–2302.

52   R. Schlem, C. F. Burmeister, P. Michalowski, S. Ohno, G. F. Dewald, A. Kwade and W. G. Zeier, *Adv. Energy Mater.*, 2021, **11**, 2101022.

53   A. Mauger, C. M. Julien, A. Paolella, M. Armand and K. Zaghib, *Materials (Basel).*, 2019, **12**, 1–86.

54   Y. Zhao, L. Wang, Y. Zhou, Z. Liang, N. Tavajohi, B. Li and T. Li, *Adv. Sci.*, 2021, **8**, 1–22.

55   L. Yue, J. Ma, J. Zhang, J. Zhao, S. Dong, Z. Liu, G. Cui and L. Chen, *Energy Storage Mater.*, 2016, **5**, 139–164.

56   N. Kamaya, K. Homma, Y. Yamakawa, M. Hirayama, R. Kanno, M. Yonemura, T. Kamiyama, Y. Kato, S. Hama, K. Kawamoto and A. Mitsui, *Nat. Mater.*, 2011, **10**, 682–686.

57   Z. Yu, S. L. Shang, J. H. Seo, D. Wang, X. Luo, Q. Huang, S. Chen, J. Lu, X. Li, Z. K. Liu and D. Wang, *Adv. Mater.*, 2017, **29**, 0–6.

58   W. D. Richards, L. J. Miara, Y. Wang, J. C. Kim and G. Ceder, *Chem. Mater.*, 2016, **28**, 266–273.

59   A. Unemoto, M. Matsuo and S. I. Orimo, *Adv. Funct. Mater.*, 2014, **24**, 2267–2279.

60   R. Mohtadi and S. I. Orimo, *Nat. Rev. Mater.*, 2016, **2**, 1–16.

61   L. Duchêne, A. Remhof, H. Hagemann and C. Battaglia, *Energy Storage Mater.*, 2020, **25**, 782–794.

62   F. Li, Z. Wei, A. Manthiram, Y. Feng, J. Ma and L. Mai, *J. Mater. Chem. A*, 2019, **7**, 9406–9431.

63   X. Xu, D. Zhou, X. Qin, K. Lin, F. Kang, B. Li, D. Shanmukaraj, T. Rojo, M. Armand and G. Wang, *Nat. Commun.*, 2018, **9**, 1–12.

64   M. Paskevicius, B. R. S. Hansen, M. Jørgensen, B. Richter and T. R. Jensen, *Nat. Commun.*, 2017, **8**, 10–15.

65   C. Zhou, Y. Yan and T. R. Jensen, *ACS Appl. Energy Mater.*, 2023, **6**, 7346–7352.

66   W. S. Tang, A. Unemoto, W. Zhou, V. Stavila, M. Matsuo, H. Wu, S. I. Orimo and T. J. Udovic, *Energy Environ. Sci.*, 2015, **8**, 3637–3645.

67   Z. Zhang, Y. Shao, B. Lotsch, Y. S. Hu, H. Li, J. Janek, L. F. Nazar, C. W. Nan, J. Maier, M. Armand and L. Chen, *Energy Environ. Sci.*, 2018, **11**, 1945–1976.

68   G. Y. Adachi, N. Imanaka and H. Aono, *Adv. Mater.*, 1996, **8**, 127–135.

69   F. Tsuji, N. Tanibata, A. Sakuda, A. Hayashi and M. Tatsumisago, *Chem. Lett.*, 2018, **47**, 13–15.

70   A. Banik, T. Famprikis, M. Ghidiu, S. Ohno, M. A. Kraft and W. G. Zeier, *Chem. Sci.*, 2021, **12**, 6238–6263.

71   F. Tan, H. An, N. Li, J. Du and Z. Peng, *Nanoscale*, 2021, **13**, 11518–11524.

72   H. Yang and N. Wu, *Energy Sci. Eng.*, 2022, **10**, 1643–1671.

73   J. S. Rowlinson, *Mol. Phys.*, 2005, **103**, 2821–2828.

74   D. P. Almond, *Solid State Ionics*, 1986, **18**, 1105–1109.

75   A. Berger, A. Ibrahim, C. E. Buckley and M. Paskevicius, *Phys. Chem. Chem. Phys.*, 2023, **25**, 5758–5775.

76   L. He, H. W. Li, H. Nakajima, N. Tumanov, Y. Filinchuk, S. J. Hwang, M. Sharma, H. Hagemann and E. Akiba, *Chem. Mater.*, 2015, **27**, 5483–5486.

77   Y. Sadikin, M. Brighi, P. Schouwink and R. Černý, *Adv. Energy Mater.*, 2015, **5**, 1501016.

78   T. J. Udovic, M. Matsuo, W. S. Tang, H. Wu, V. Stavila, A. V. Soloninin, R. V. Skoryunov, O. A. Babanova, A. V. Skripov, J. J. Rush, A. Unemoto, H. Takamura and S. I. Orimo, *Adv. Mater.*, 2014, **26**, 7622–7626.

79   H. Rickert, *Angew. Chemie Int. Ed. English*, 1978, **17**, 37–46.

80   H. Defrancesco, J. Dudley and A. Coca, *ACS Symp. Ser.*, 2016, **1236**, 1–25.

81   G. Önal and F. Burat, *Gospod. Surowcami Miner.*, 2008, **24**, 49–60.

82   J. Zhou and P. Bai, *ASIA-PACIFIC J. Chem. Eng.*, 2015, **10**, 325–338.

83   P. Laszlo, *Angew. Chemie - Int. Ed.*, 2000, **39**, 2071–2072.

84   E. A. Malinina, V. V. Avdeeva, L. V. Goeva and N. T. Kuznetsov, *Russ. J. Inorg. Chem.*, 2010, **55**, 2148–2202.

85   R. E. Rundle, *J. Phys. Chem.*, 1947, **61**, 45–50.

86   W. N. Lipscomb, *Science (80-.).*, 1977, **196**, 1047–1055.

87   K. Wade, *J. Chem. Soc. D Chem. Commun.*, 1971, 792–793.

88   M. A. Fox, A. E. Goeta, A. K. Hughes and A. L. Johnson, *J. Chem. Soc. Dalt. Trans.*, 2002, **11**, 2132–2141.

89   S. Körbe, P. J. Schreiber and J. Michl, *Chem. Rev.*, 2006, **106**, 5208–5249.

90   H. Han, Y. Y. Wang, X. C. Yu, Y. N. Ma and X. Chen, *Crystals*, 2022, **12**, 1339.

91   R. W. Chapman, J. G. Kester, K. Folting, W. E. Streib and L. J. Todd, *Inorg. Chem.*, 1992, **31**, 979–983.

92   J. L. Little, M. A. Whitesell, J. G. Kester, K. Folting and L. J. Todd, *Inorg. Chem.*, 1990, **29**, 804–808.

93   H. Schubert, F. R. Küchle and L. Wesemann, *Collect. Czechoslov. Chem. Commun.*, 2010, **75**, 963–970.

94   E. Molinos, T. P. H. Player, G. Kociok-Köhn, G. D. Ruggerio and A. S. Weller, *Heteroat. Chem.*, 2006, **17**, 174–180.

95   L. Wesemann, T. Marx, U. Englert and M. Ruck, *Eur. J. Inorg. Chem.*, 1999, 1563–1566.

Chapter 2

Experimental

CHAPTER 2 - EXPERIMENTAL

2.1 Chemical Synthesis

2.1.1 Equipment and Materials

All chemical synthesis was performed in a fume hood using a Schlenk line to ensure an inert argon atmosphere for all samples where necessary. All air sensitive materials were stored in an argon filled glove box (MBraun, < 0.1 ppm H_2O, < 0.1 ppm O_2) to ensure the preservation of samples due to the highly hygroscopic nature of the materials produced. All synthesis and analysis was performed at Curtin University, Perth apart from Synchrotron Radiation – X-Ray Diffraction, which was conducted at the Australian Synchrotron, Melbourne.

2.1.2 Trimethylammonium *nido*-undecaborate

Trimethylammonium *nido*-undecaborate ($Me_3NHB_{11}H_{14}$) is the starting chemical for all the materials further synthesised. It can be produced by the self-condensation of sodium borohydride ($NaBH_4$) using 1-bromopentane ($C_5H_{11}Br$) in a diethylene glycol dimethyl ether (diglyme) solvent. The method used was published by Dunks *et al.* (detailed below) by first synthesising the sodium analogue.[1]

2.1.2.1 Synthesis of sodium nido-undecaborate (NaB₁₁H₁₄)

This method is adapted from the method shown by Dunks *et al.*[1] Sodium borohydride (24.88 g, 65.8 mmol) was added to diglyme (200 mL) in a three necked round bottom flask. The flask was equipped with a dropping funnel and a mechanical stirrer under an inert argon atmosphere. The mixture has heated to 110 °C before 1-bromopentane (76 mL, 61.3 mmol)

was added dropwise over 4 hours, ensuring the temperature remains between 105 – 120 °C, which is crucial to avoid the synthesis of unwanted by-products such as $B_3H_8^-$ and $B_9H_{14}^-$.[1] The mixture was stirred for 6 hours and then filtered at room temperature *in vacuo* and washed with small aliquots of diethyl ether. The filtrate was collected and the solvent removed *in vacuo* leaving the sticky yellow solid $NaB_{11}H_{14}$.digylme product (14.36 g). This product contained a large amount of coordinated diglyme deeming the yield was not able to be accurately determined.

2.1.2.2 Synthesis of trimethylammonium nido-undecaborate (Me₃NHB₁₁H₁₄)

$NaB_{11}H_{14}$.diglyme (2.04 g, 13.1 mmol) was dissolved in warm milli-Q water (19 mL). Trimethylamine hydrochloride (2.43 g, 25.4 mmol) was dissolved in water (10 mL) and added slowly to the borate solution, precipitating into the product as a pale yellow solid. The mixture was filtered and the filtrate dried *in vacuo* at 100 °C. This yielded a pale yellow solid product (0.63 g, 3.3 mmol, 25% yield). This yield was 38% with respect to the initial amount of sodium borohydride used for the synthesis.

2.1.3 Synthesis of $M_2B_{11}H_{11}Pb$ (M = Li, Na, K)

The method was adapted from Chapman *et al.*[2] $(Me_3)_3NHB_{11}H_{14}$ (1.231 g, 6.37 mmol) was dissolved in aqueous MOH (45 mL, 2M, M = Li, Na, K) before $PbCl_2$ (3.713 g, 13.35 mmol) was added and stirred at room temperature for 4 hours. The grey suspension was filtered and the filtrate neutralised to pH 7 using HCl (1M). The resulting grey precipitate was filtered, and the filtrate dried using a rotary evaporator yielding a yellow solid product. The solid was dissolved in CH_3CN (20 mL) to remove the insoluble MCl by-product, filtered and the filtrate dried once more at 150 °C yielding a pale yellow, highly hygroscopic solid, which was stored under an inert atmosphere ($Na_2B_{11}H_{11}Pb$ (0.7752 g, 2.02 mmol, 32% yield) ($Li_2B_{11}H_{11}Pb$ – 34% yield, $K_2B_{11}H_{11}Pb$ – 30% yield). ^{11}B {^1H} NMR (128 MHz, CD_3CN, ppm) −3.5 (s, 1B), −5.4 (t, $^1J_{11B–207Pb}$ = 263 Hz, 5B), −10.8 (s, 5B). ^1H {^{11}B} NMR (400 MHz, CD_3CN, ppm) 6.7 (s, 1H), 3.0 (s, 5H), 0.9

(t, $^2J^1_{H^{-207}Pb}$ = 120 Hz, 5B). FTIR (ATR, cm^{-1}) 2420 (vs), 1600 (w), 1050 (m), 730 (m), 700 (w), 520 (m).

2.1.3.1 Synthesis of (MePh₃P)₂B₁₁H₁₁Pb

2.1.3.1 Synthesis of (MePh$_3$P)$_2$B$_{11}$H$_{11}$Pb

$(CH_3)_3NHB_{11}H_{14}$ (0.271 g, 1.40 mmol) was dissolved in *M*OH (20 mL, 2M) before $PbCl_2$ (1.514 g, 5.45 mmol) was added and stirred at room temperature for 4 hours. The grey suspension was filtered and the filtrate neutralised to pH 7 using HCl (1M) and filtered *in vacuo* once more. MePh$_3$PBr (1.010 g, 2.83 mmol) was dissolved in milli-Q H_2O (10 mL) and added to the filtrate. A yellow solid precipitate was filtered, washed with milli-Q H_2O (2 x 5 mL), and the resulting solid dried at 90 °C under vacuum for 4 hours ((MePh$_3$P)$_2$B$_{11}$H$_{11}$Pb, 0.8664 g, 0.971 mmol, yield 69 %). ^{11}B {^1H} NMR (128 MHz, CD$_3$CN, ppm) −3.5 (s, 1B), −5.4 (m, 5B), −10.8 (s, 5B).

2.1.4 Synthesis of Li₂B₁₁H₁₁Sn

2.1.4 Synthesis of Li$_2$B$_{11}$H$_{11}$Sn

$(Me_3)_3NHB_{11}H_{14}$ (2.600 g, 13.46 mmol) was dissolved in anhydrous tetrahydrofuran (THF, 40 mL) and cooled to 0 °C before *n*-butyllithium (30 mL) was added dropwise and the solution stirred for 30 minutes under an inert argon atmosphere. Tin (II) chloride (3.70 g, 19.51 mmol) dissolved in THF (30 mL) was added dropwise to the pale yellow solution at room temperature. The solution turned deep red instantaneously and stirring continued for a further 4 hours at room temperature. THF was removed using rotary evaporation and the dry product was dissolved in aqueous lithium hydroxide (1M, 50 mL) to extract the product from the resulting mixture. The solution was filtered *in vacuo* and the filtrate neutralised to pH 7 using HCl (1M). The solvent was removed *in vacuo* and acetonitrile (15 mL) was added to the resultant solid to aid the removal of the LiCl by-product. The suspension was filtered and the filtrate was dried *in vacuo* at 150 °C leaving a pale yellow, highly hygroscopic solid, which was stored under argon, Li$_2$B$_{11}$H$_{11}$Sn (2.083 g, 7.93 mmol, 59% yield). ^{11}B {^1H} NMR (128 MHz,

CD$_3$CN) −5.3 (s, 1B), -11.1 (s, 5B), -12.4 (s, 5B). ^{1}H {^{11}B} NMR (400 MHz, CD$_3$CN) 2.98 (s, 1H), 1.60 (s, 5H), 0.82 (s, 5B).

2.1.4.1 Synthesis of M$_2$B$_{11}$H$_{11}$Sn (M = Na, K)

Li$_2$B$_{11}$H$_{11}$Sn (0.215 g, 0.819 mmol) was dissolved in water (5 mL) and passed through a column containing Amberlite® IR 120 hydrogen form ion exchange resin. The resulting acidic solution was treated with the relevant metal hydroxide (NaOH or KOH) until pH 7 was obtained. The water was removed *in vacuo* at 150 °C leaving the desired product, Na$_2$B$_{11}$H$_{11}$Sn (0.201 g, 84% yield) or K$_2$B$_{11}$H$_{11}$Sn (68% yield).

2.1.5 Synthesis of LiB$_{11}$H$_{11}$Bi

(Me$_3$)$_3$NHB$_{11}$H$_{14}$ (0.75 g, 3.88 mmol) was dissolved in anhydrous THF (30 mL) and cooled to 0 °C before *n*-butyllithium (6 mL) was added dropwise and the solution stirred for 15 minutes under an inert Ar atmosphere. Bismuth (III) chloride (2.26 g, 7.17 mmol) dissolved in THF (15 mL) was added dropwise to the pale yellow solution at room temperature. The solution turned black instantaneously and was stirred for a further 15 minutes at room temperature before being refluxed for 4 hours at 65 °C. Water (4 mL) was added then the solvent was removed *in vacuo*. The residues were dissolved in water and the mixture filtered *in vacuo* and the resulting yellow liquid was dried *in vacuo*. The resultant solid was dried *in vacuo* at 150 °C leaving a pale yellow, highly hygroscopic solid, which was stored under argon, LiB$_{11}$H$_{11}$Bi (0.677 g, 1.96 mmol, 50 % yield).

2.1.5.1 Synthesis of NaB$_{11}$H$_{11}$Bi

LiB$_{11}$H$_{11}$Bi (0.282 g, 0.82 mmol) was dissolved in water (6 mL) and passed through a column containing Amberlite® IR 120 hydrogen form ion exchange resin. The resulting acidic solution

was treated with the sodium hydroxide until pH 7 was obtained. The water was removed *in vacuo* at 150 °C leaving the desired product, $Na_2B_{11}H_{11}Bi$ (0.181 g, 61 % yield).

2.1.6 Synthesis of $MB_{11}H_{11}Sb$ (M = Li or Na)

$(Me_3)_3NHB_{11}H_{14}$ (0.821 g, 4.25 mmol) was dissolved in anhydrous THF (80 mL) and triethylamine (2.4 mL) was added before stirring for 15 minutes under an inert Ar atmosphere. Antimony (III) chloride (1.21 g, 5.3 mmol) dissolved in THF (15 mL) was added dropwise to the pale yellow solution at room temperature. The solution turned red instantaneously, then brown, and was stirred for a further 12 hours at room temperature. The solvent was removed *in vacuo* resulting in a brown oil. Lithium or sodium hydroxide (1 M, 20 mL) was added then the solution was heated to 80 °C for 2 hours whilst stirring and the resultant orange solid was filtered *in vacuo*. The filtrate was neutralised to pH 7 using HCl and a yellow solid formed. This was filtered *in vacuo* and the filtrate dried *in* vacuo. Acetone (20 mL) was added to the resulting solid and the insoluble LiCl by-product was filtered *in vacuo.* The filtrate was dried *in vacuo* at 80 °C for 5 hours leaving a pale yellow, highly hygroscopic solid, which was stored under argon, $LiB_{11}H_{11}Sb$ (0.174 g, 0.67 mmol, 16 % yield), $NaB_{11}H_{11}Sb$ (0.280 g, 1.02 mmol, 24 % yield).

2.2 List of Chemicals

Table 2.1. List of chemicals used in this project.

Chemical Name	Formula	Purity %	State	Supplier
1-bromopentane	$C_5H_{11}Br$	98	Liquid	Merck
Acetone	$CH_3C(O)CH_3$	-	-	Unilab
Acetonitrile	CH_3CN	-	Anhydrous	Merck
Amberlyte® IR120 hydrogen ion exchange resin	-	-	Beads	Merck

Antimony (III) chloride	$SbCl_3$	98	Anhydrous	Merck
Argon	Ar	99.997	Gas	Coregas
Bismuth (III) chloride	$BiCl_3$	98	Anhydrous	Merck
Deionised (milli-Q) water	H_2O	18 MΩcm	Liquid	
Acetonitrile-d_3	CD_3CN	99.8	Liquid	Merck
Dimethylsulfoxide-d_6	$(CD_3)_2SO$	99.9	Liquid	Merck
Water-d_2	D_2O	99.9	Liquid	Merck
Diethyl ether	Et_2O	99.7	Liquid	Merck
Diglyme (diethylene glycol dimethyl ether)	$C_6H_{14}O_3$	99.5	Anhydrous	Merck
Gold foil	Au	99.95	Foil, 0.1 mm	Merck
Hydrochloric acid	HCl	37	Liquid	Scharlau
Lead (II) chloride	$PbCl_2$	98	Anhydrous	Merck
Lithium hydroxide	LiOH	98	Powder	Alfa Aeser
Methyltriphenylphosponium bromide	$MePh_3PBr$	98	Powder	Merck
n-butyllithium	nC_4H_9Li	2.5M in hexane	-	Merck
Platinum	Pt	99.99	Foil, 0.1 mm	Merck
Potassium hydroxide	KOH	≥ 85	Powder	Merck
Sodium borohydride	$NaBH_4$	99	Powder	Merck
Sodium hydroxide	NaOH	98	Pellets	Merck
Super P conductive carbon	C	> 99	Powder	Merck
Tetrahydrofuran	C_4H_8O	99	Anhydrous (with 250 ppm BHT inhibitor)	Merck
Tin (II) chloride	$SnCl_2$	98	Anhydrous	Merck
Triethylamine	Et_3N	99.5	Liquid	Merck
Trimethylamine hydrochloride	$Me_3N\bullet HCl$	99	Solid	Merck

2.3 Nuclear Magnetic Resonance

Nuclear Magnetic Resonance spectroscopy (NMR) is a technique that gathers information on the presence of a particular element within a material and also the chemical environment of these particular atoms within the molecular structure. In NMR, the nuclear spin of an atom interacts with an electric or magnetic field, which increases the energy of the nuclear spin. When this relaxes, the energy is released as a radio wave and is detected.[3] This is only possible for nuclei with a spin, I, of greater than zero and these nuclei are said to be "NMR active". Each NMR active element gives off its own characteristic frequency so different elements can be probed by detecting different frequencies.

This project used traditional liquid-phase NMR, which comprised of solid samples being dissolved in solvents before being probed. This is vital as probing in the solid state can lead to anisotropic interactions between the molecules, for example, dipolar coupling which leads to peak broadening and thus losing vital resolution in the data. In the liquid state, the molecules are free to move and rotate, meaning that there is no net orientation.[3,4] The peak positions are determined by the shielding of respective nuclei within the molecule.[3] The amount of shielding a nucleus has depends on neighbouring atoms and, as a result, the electron density around the atom. This slightly changes the frequency of the signal that is omitted, thus seeing a different peak position on the resulting spectrum. Traditionally, NMR spectra are reported against a known standard (^{1}H NMR = tetramethylsilane (TMS), ^{11}B NMR = trifluoroborane diethyl ether) and this corresponds to a chemical shift: δ = 0 ppm. Chemical shift = Change in frequency / Frequency of the spectrometer.

In this project, [11]B and ^{1}H nuclei were probed using a Bruker Avance III 400 MHz spectrometer (128.1 MHz used for [11]B experiments). As these nuclei, along with other elements studied in this project, for example Pb and Sn, are NMR active each signal is split by coupling with the spin of NMR active neighbouring elements. This phenomenon only occurs when coupling with different elements and does not occur for coupling between identical elements. The quantity of peaks seen are governed by equation 4.1.

$$Number\ of\ Peaks = 2 \times N \times I + 1$$

N = number of neighbouring atoms

I = Nuclear Spin of neighbouring atoms

For example, in ^{11}B NMR, a boron atom bonded to a hydrogen atom (*I* = ½) would show a doublet (2 peaks) as 2 x 1 x ½ + 1 = 2. However, coupling to different nuclei can be avoided by probing the materials with a small frequency range or specific frequency. This eliminates this splitting effect and shows just single peaks per chemical environment within the sample. This is particularly important for elucidating the exact chemical shift of the signal and furthermore to help distinguish overlapping signals with similar chemical shifts.

2.4 Fourier Transform Infrared Spectroscopy

Fourier Transform Infrared Spectroscopy (FTIR) is an analytical technique that allows functional groups within molecular solids and liquids to be identified. The sample is bombarded with multi frequency infrared radiation and the energy that is absorbed/transmitted is measured. Chemical bonds in the material absorb distinct frequencies of energy and as a result can be characterised by the absorption at respective frequencies.

For a bond to be "IR active" and absorb infrared radiation then it must undergo a change in dipole moment. Consequently, in a ground state the bond in question must have a dipole moment and therefore be a polar bond. Homonuclear single bonds are therefore not active and will show not infrared absorption. Homonuclear pi bonds can be IR active if the substituents of the two atoms in the bonds are not equal. As a result, carbon-carbon double bonds can be identified using FTIR spectroscopy.

In this project, samples were analysed using a Thermo Fisher Nicolet Summit spectrometer with an Attenuated Total Reflected (ATR) module with a diamond crystal. Samples (as a powder) were exposed to a minimal amount of air ($\sim$ 2 secs) when conducting the experiments. This was unavoidable due to the location of the spectrometer in air. Reflection

ATR was used to measure the samples directly to avoid mixing with a salt or dissolving within a solvent.

2.5 Raman Spectroscopy

Raman Spectroscopy is a vibrational spectroscopic technique similar to FTIR spectroscopy. It is also used to determine the vibrational modes of a molecule. This allows functional groups within a material to be determined which helps with phase identification. For a specific vibration to be "Raman-active" there must be a change in polarisability caused by the vibration. These vibrations tend to be IR inactive in nature so a mixture of techniques can be used to gain more knowledge about the bonding within a molecule.

This technique is based on the scattering of light in the near infrared or visible light region by the vibration of bonds within a molecule at specific energy levels. The energy from the light source excites the molecule to a higher energy level. Upon relaxation, energy is released as photons in both elastic (Rayleigh scattering) and inelastic (Stokes or anti-Stokes) modes. Raman spectroscopy uses the inelastic scattering and these photons are detected and results are produced as a change in wavenumber (cm^{-1}) from the incident beam.

In this project, Raman spectroscopy was performed using a WITec Alpha 300 SAR confocal Raman microscope with a 532 nm green light excitation wavelength and 600 grating/mm. Samples were prepared by packing powder into a 1 mm wide borosilicate capillaries in an argon filled glovebox, then flame sealed to ensure no exposure to air and moisture which would degrade the samples. Spectra were collected using 100 accumulations with an integration time of 400 ms and data processing was performed using Project 4 (WITec) software, which includes background subtraction. Data was acquired with assistance of Dr Thomas Becker at Curtin University.

2.6 X-Ray Diffraction

X-Ray Diffraction (XRD) is an extremely powerful tool for characterising crystalline solid state materials and provides information about the composition and size of the unit cell.[5] A unit cell is the minimum repeating unit within the crystal structure that is repeated throughout the lattice. Diffraction patterns are characteristic for each compound, due to the characteristic nature of each compound's unit cell and the atoms within. In powder XRD, the sample is ground into a fine powder to reduce the preferential orientation of the crystals in the powder to ensure accurate intensities for each peak in the diffraction pattern.[6] Single crystal XRD is also available, however this was not possible to be used in this project due to single crystals of the materials being extremely difficult to grow. Preferential orientation reduces the intensity for some diffraction reflections but techniques can avoid preferential orientation, including rotating the sample during data collection.

Monochromatic X-rays are fired at the sample and these rays are scattered in all directions but are constructively reinforced when Bragg's Law (Figure 2.1) is satisfied (Equation 2.1). When the X-rays pass through the sample, they are diffracted by the atoms within the crystal structure, which acts as a diffraction grating. This leads to areas of constructive and deconstructive interference, which manifests itself as areas of high and low intensity in the resulting diffraction pattern. These photons are picked up by a detector that shows the angle at which the X-rays have been diffracted by the sample. X-rays are used because they have a wavelength of $\sim$ 0.5 – 2.5 Å, which is in the order of interatomic distances within a crystal. Monochromatic waves are used to keep the wavelength constant so that only the incident angle (ϑ) between the X-Ray source and diffraction plane and the distance between diffraction planes (d) differ.

$$n\lambda = 2d\sin\theta \hspace{4cm} (2.1)$$

n = integer

λ = Incident Wavelength

d = Distance between diffraction planes

ϑ = Incident Angle
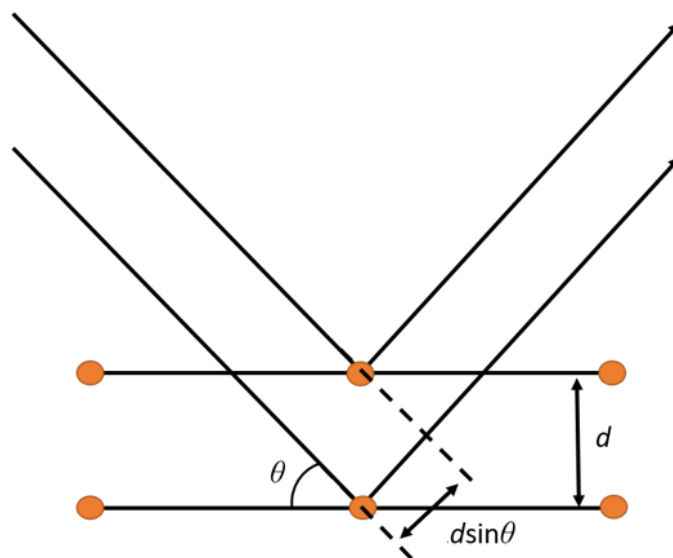
Figure 2.1. Depiction of Bragg's Law.

In this project, synchrotron radiation was used as this gives high intensity X-rays, which provides high resolution and low signal-to-noise. Furthermore, it allowed the rapid acquisition of data and *in-situ* data while ramping the temperature of the sample.

In this project, *in situ* data was collected on the powder diffraction beamline at the Australian Synchrotron using a Mythen-II strip detector using two wavelengths, 0.59096(1) Å and 0.825040(5) Å. All samples were ground into a fine powder and packing into a borosilicate capillary (inner diameter – 0.7 mm) under an argon atmosphere then flame sealed to prevent any exposure to air or moisture. The samples were heated using a hot air blower to a variety of temperatures depending on the material at 6 °C min^{-1}. The X-ray wavelength was calibrated using a LaB$_6$ standard (NIST 660b) and sample temperatures were calibrated against the known lattice parameters of silver and sodium chloride as a function of temperature.[7] Crystallographic indexing was performed in Topas v.5 (Bruker, Germany), peaks were indexed

using an indexing phase, then matched against all space groups with known impurities added. *Ex situ* data was performed using a Bruker D8 Advance diffractometer equipped with a copper X-ray source Cu K$_{\alpha 1}$ radiation, λ = 1.540593 Å, Cu K$_{\alpha 2}$ radiation, λ = 1.544414 Å and a Lynxeye PSD detector in Bragg-Brentano geometry. Data were collected in the 2θ range from 5° to 80° with a step size of 0.02°. Powder samples were prepared into a flat-plate in an argon filled glovebox and the packed material was covered with a MYLAR® film and sealed with grease to prevent contact with air and moisture.
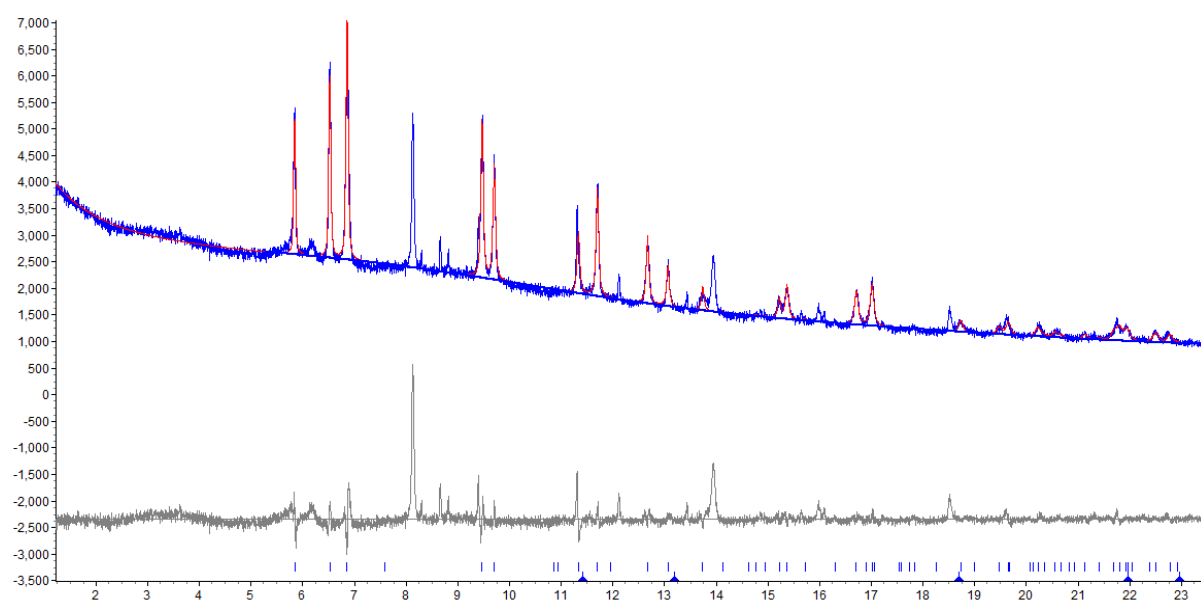
Figure 2.2. Le Bail fit of LiB$_{11}$H$_{11}$Pb with known LiCl impurity and an unknown impurity, performed in Topas. Space Group – 102, lattice parameter – a = b = 6.99 Å, c = 10.39 Å.

2.7 Scanning Electron Microscopy

Scanning Electron Microscopy (SEM) is a technique that allows the morphology of a sample to be imaged by bombarding the sample with high energy electrons and measuring the resulting secondary or backscattered electron emitted as a result. In this project, a Zeiss Neon 40EsB scanning electron microscope was used to collect high resolution surface images.

SEM allows the surface of a sample to be captured at micron scale and therefore particle details such as size and shape can be captured and determined. Firstly, a filament is used to

generate electrons that are then bundled into a beam and focussed onto the surface of the sample. These electrons are accelerated and fired at the sample, which causes secondary and backscattered electrons to be emitted and are collected by a detector. The energy of the electrons can be tuned between 0.5 – 30 kV depending on the aim of the experiment to gather the best morphological information with a lower voltage showing a higher resolution but higher voltages resulting in a stronger signal.

In this project, all samples were prepared in an argon filled glovebox. Powder samples were loaded on carbon tape mounted on an aluminium stub. Samples were covered in a custom made air sealed container then placed inside the air free atmosphere SEM, preventing air exposure. All images were produced using backscattered electrons as this gave the best images with the samples and was conducted in conjunction with Energy Dispersive X-Ray analysis. The acceleration voltage used was 20 kV at a working distance of 7 mm and an aperture size of 60 mm.
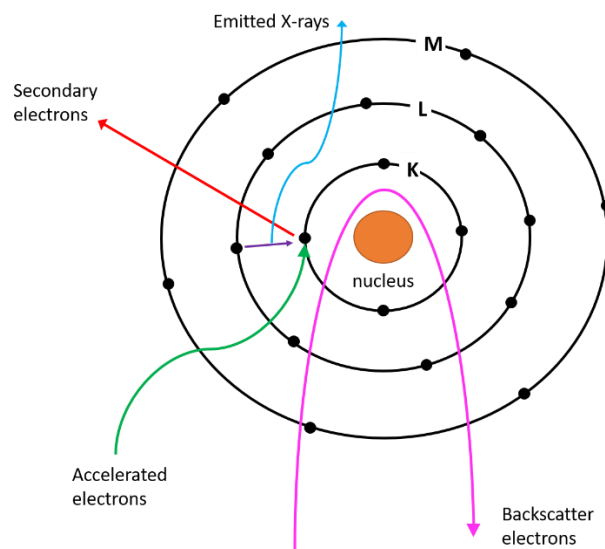
Figure 2.3. Depicting the generation of emitted electrons and X-rays detected by a Scanning Electron Microscope (SEM) and an Energy Dispersive X-Ray Spectrometer (EDS).

2.8 Energy Dispersive X-Ray Spectroscopy

Energy Dispersive X-ray Spectroscopy (EDS) is an elemental analysis tool used to determine the presence of an element and the chemical composition of a sample. It uses the same scanning electron microscope as the SEM images used in the thesis, however a separate detector detecting X-rays is used. High energy electrons (at approximately 20 kV) were bombarded at the sample and beam electrons can eject a core electron from a low-lying energy level creating a core hole. Once such a hole is created, an electron from a higher shell can relax into the lower energy state. This process leads to emission an X-ray with the same energy as the difference between the two respective energy levels. Each element has characteristic binding energies for its electrons, the energy of this X-ray can be matched to a distinct transition between energy levels in a specific element. The intensity of these X-rays measured by the detector can also give information about the relative abundancies of these elements within the sample, as a result, quantitative measurements can be performed, however are often inaccurate unless flat samples and standards are used to calibrate the signals. This allows the composition of the compound to be determined. However, a drawback to this technique is that it is difficult to detect lighter elements due to the low energy gap between energy levels. Lighter elements than boron do not have a sufficient energy gap between its outer electrons and a core hole to be detected. To detect these elements, other techniques such as NMR, ICP-OES or MS can be used. In this project, the Aztec software was used alongside the Zeiss Neon 40EsB scanning electron microscope.

2.9 Differential Scanning Calorimetry – Thermographic Analysis

Differential scanning calorimetry (DSC) is a technique used to determine the temperature and energy of phase changes and other thermodynamic events of materials. DSC measures the changes in heat flow in a material, which are exothermic and endothermic events, caused by physical or chemical changes in a sample. This allows phase transition temperatures to be determined from a variety of events, for example, melting, crystallisation or polymorphic

transitions. Thermogravimetric Analysis (TGA) can be conducted simultaneously with DSC and measures the change in mass of a sample as a function of temperature. This allows any mass loss due to the evolution of gases to be quantified.

In this project, DSC-TGA data was collected using a NETZSCH STA 449 F3 Jupiter paired with a Pt furnace. The temperature was ramped at 10 °C min^{-1} under a constant argon flow of 40 mL min^{-1}. The final temperature reached for each sample was determined based on the material itself. The temperature and sensitivity of the DSC-TGA was calibrated using In, Zn, Sn, Bi, and CsCl reference materials, resulting in a temperature accuracy of ± 0.2 °C. All samples were prepared in an argon filled glovebox to prevent contamination. Samples weighing ∼ 4 mg were sealed in an aluminium crucible with a pinhole pierced in the top, immediately prior to applying a vacuum to the crucible in the DSC-TGA, to allow the escape of any gases evolved during measurement. This also removed air and moisture from the furnace allowing an accurate analysis of the samples.

2.10 Residual Gas Analysis – Mass Spectroscopy

Residual Gas Analysis – Mass Spectroscopy (RGA-MS) is a technique which allows the determination of gases evolved as a material is heated in a vacuum. This technique was used to determine any coordinated solvents, which can be identified upon evolution along with any gaseous thermal decomposition products of the material. An RGA−MS (Stanford Research systems, SRS, RGA−300) equipped with a quadrupole probe was used with a vacuum pressure of ∼ 10^{-4} mbar. Data was collected as an intensity of different masses of gases hitting the detector up to a maximum mass on charge (m/z) ratio of 65. Samples (∼ 10 mg) were placed in stainless steel Swagelok reactors with a gas filter (to allow gases but not solids to pass through) in an argon filled glovebox. The reactor was heated in a tube furnace from 25 - 500 °C at 10 °C min^{-1}.

2.11 Temperature Programmed Photographic Analysis

Temperature programmed photographic analysis (TPPA) is a technique where the physical appearance of a compound can be monitored and visualised as a function of temperature.[8] Samples were pressed into a 6 mm diameter pellet with a thickness of approximately 1 mm under a pressure of 350 MPa in an argon filled glovebox. The pellets were placed in a borosilicate test tube fitted with a rubber septum and an argon filled balloon to maintain the argon atmosphere and prevent pressure build up. Temperature was heated to 325 °C at 4 °C min^{-1} using an Omega CSi8D series benchtop controller attached to a brass heating block. The temperature was measured using a K-type thermocouple and videos were recorded using a Celestron 5 MP digital microscope pro.

2.12 Electrochemical Impedance Spectroscopy

Electrochemical impedance spectroscopy (EIS) is a technique used to measure the ion conductivity of a material.[9] In impedance spectroscopy, a sinusoidal perturbation voltage, E(t) is applied to a system that results in a linear current density, *j(t)* which shares the frequency of the input voltage. The ratio of these quantities in the impedance, *Z(t)*.

$$Z(t) = \frac{E(t)}{j(t)} \tag{2.2}$$

This is potentiostatic EIS (PEIS) and by varying the frequency, processes at different timescales can be determined. Ion migration can occur at higher frequencies, whereas diffusion is more prevalent at lower frequencies.

The input voltage *E(t)* can be written as

$$E(t) = |\Delta E| \sin(\omega t) \tag{2.3}$$

|ΔE| = peak voltage amplitude

ω = angular frequency

The current response $j(t)$ is known as

$$j(t) = |\Delta j| \sin(\omega t + \Delta t) \tag{2.4}$$

$|\Delta j|$ = current density amplitude

Δt = phase difference

The component ($\omega t + \Delta t$) is the phase angle and can be written as, φ. As the quantities $E(t)$ and $j(t)$ contain magnitude and phase information, they can be written as complex number having both real (Z_{re}) and imaginary (Z_{im}) components.

$$|Z(\omega)| = \sqrt{Re\ (Z(\omega))^2 + Im\ (Z(\omega))^2} \tag{2.5}$$

Equation 2.6 can be visualised using a Nyquist plot (Figure 2.4b), which plots Z_{re} and Z_{im} on the x and y coordinates, respectively. These plots of a symmetrical cell with ion blocking electrodes (gold in this project) (Au|electrolyte|Au) show a semi-circle followed by a 45° line known as the Warburg impedance. $R1$ is the offset from the y-axis where the semicircle begins, as seen in Figure 2.3a, and comes from the resistance from the connections and wiring and $R2$ signifies the resistance within the electrolyte itself. The intercept of the semi-circle with the Warburg impedance signifies the total resistance of the cell, which is used to measure the ion conductivity of the material at a given temperature. The total resistance, R_T = $R1 + R2$, can be used to measure the ion conductivity using equation 4.6.

$$\sigma = \frac{d}{R_T A} \tag{2.6}$$

σ = ion conductivity (S cm^{-1})

d = pellet thickness (cm)

R_T = total resistance (Ω)

A = pellet area (cm^2)

In this project, EIS was measured using a ZIVE SP1 instrument. Materials were prepared within an argon filled glovebox and powder samples were pressed into a pellet of thickness $\approx$ 1 mm (measured using a micrometre to ascertain a more accurate thickness) and diameter 6 mm

by applying a pressure of 9800 N (350 MPa) for 60 seconds. The resulting pellet was placed between two gold wafers (thickness – 0.1 mm) and placed within a spring-loaded Teflon sample cell with stainless steel electrodes, sealed with o-rings to prevent contamination with air and moisture. The data were collected using 50 mV AC voltage with a frequency range 1 MHz – 10 Hz.
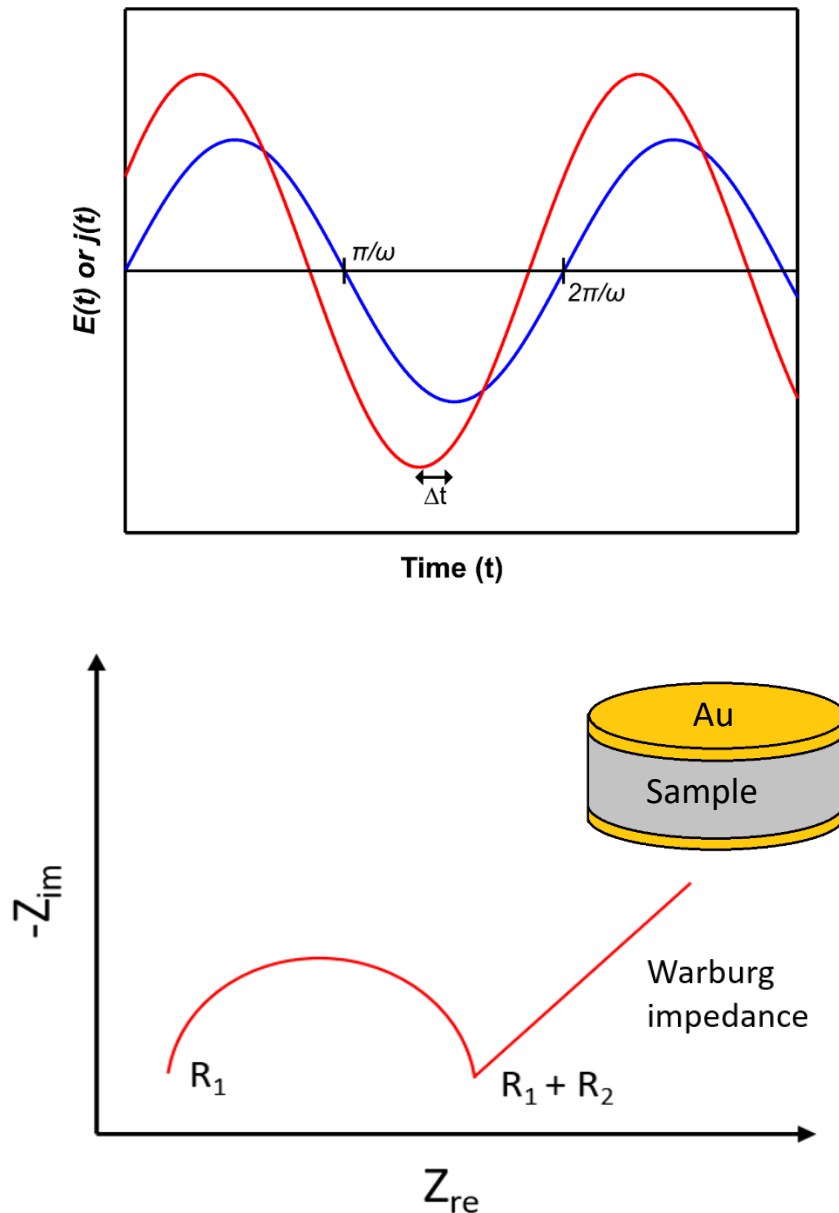

Figure 2.4a. Plot showing the relationship between the input voltage, $E(t)$ and output current, $j(t)$ which results in impedance. Figure 2.4b. Example Nyquist plot showing the initial semi-circle and Warburg impedance and an example cell used to measure this parameter.

2.13 Linear Sweep Voltammetry

Linear sweep voltammetry (LSV) is a technique that can be used to elucidate the oxidative stability of a material.[10] This gives information on the working voltages at which the materials can be used before irreversible oxidative decomposition. For materials to be used as potential solid-state electrolytes they should have a large operating window with a high oxidative stability.[11] Above the oxidative stability limit the samples oxidise which can render the surface or bulk of the material ineffective for ionic conduction. LSV is the premier technique to determine this limit with borohydride salts as other techniques, such as cyclic voltammetry (CV) can overestimate the stability limit due to the scan rate. Scanning at a slow rate (50 μV s^{-1}) allows the kinetically slow oxidation rate to be more accurately determined near its thermodynamic point, and also mixing the electrolyte with conductive carbon increases the contact surface area, thus improving the kinetics of the measurement.

In this project, the method used followed that proposed by Han *et al.* and Asakura *et al.*[10,11] The materials were mixed with graphite, previously heated to 550 °C under vacuum for 12 h, to remove moisture, in a ratio of 75:25 by mass, grinding 5 times with a pestle and mortar. 40 mg of sample was layered with 3 mg of the sample + graphite (C) mixture. This was pressed at 19600 N (693.2 MPa) in an inert argon atmosphere to form a two layered pellet. This was used to form an Al/Pt/Sample+C/Sample/Li cell and sealed in an airtight Teflon cell with stainless steel electrodes. LSV was performed twice on the same cell at 60 °C (elevated temperature used to improve ion conductivity thus producing more representative results) with a scan rate of 50 μV s^{-1}. The voltage range probed was different from sample to sample depending on the open circuit voltage of the material which is the starting point of the scan. The oxidative stability of the material vs. Li$^+$/Li was determined from the intersection point of two linear lines with $R^2 > 0.99$ (the background and the oxidative current).[11]

2.14 Computational Studies

Computational studies were used to give extra information about the ions synthetised in this project. They were used to predict the atomic coordinates of the respective anions and the electrostatic potential (ESP) surfaces, which provides information on the charge distribution within an anion. The calculations were performed using Density Functional Theory (DFT) with a B3LYP functional and a LANL2MB basis set.[12–14] This basis set was used to be able to compute the large number of electrons found in the heavy metals in the anions.[12–14] The calculations optimised the anion geometry and energy using the Gaussian G09W software energy.[15] ESP surfaces were plotted using a total density cube and a mapped surface with an isovalue of 0.008 electrons bohr^{-1} (5.40 x 10^{28} electrons m^{-3}). The electrostatic potentials were mapped in atomic units (au) - 1 au = 2.625 MJ mol^{-1}.

2.15 References

1   G. B. Dunks, K. Barker, E. Hedaya, C. Hefner, K. Palmer-Ordonez and P. Remec, *Inorg. Chem.*, 1981, **20**, 1692–1697.

2   R. W. Chapman, J. G. Kester, K. Folting, W. E. Streib and L. J. Todd, *Inorg. Chem.*, 1992, **31**, 979–983.

3   H. Günther, *NMR Spectroscopy: Basic Principles, Concepts and Applications in Chemistry*, Wiley-VCH, Siegen, 3rd edn., 2013.

4   a. Laws, David D., Bitter, H.L., Jerschow, *Angew. Chem. Int. Ed. Engl.*, 2002, **41**, 3096–3129.

5   L. D. Whittig and W. R. Allardice, in *Methods of Soil Analysis, Part 1. Physical and Mineralogical Methods-Agronomy*, ed. A. Klute, American Society of Agronomy-Soil Science Society of America, Madison, 2nd edn., 1986, pp. 331–362.

6   C. F. Holder and R. E. Schaak, *ACS Nano*, 2019, **13**, 7359–7365.

7   I. K. Suh, H. Ohta and Y. Waseda, *J. Mater. Sci.*, 1988, **23**, 757–760.

8   M. Paskevicius, M. B. Ley, D. A. Sheppard, T. R. Jensen and C. E. Buckley, *Phys. Chem. Chem. Phys.*, 2013, **15**, 19774–19789.

9   P. Vadhva, J. Hu, M. J. Johnson, R. Stocker, M. Braglia, D. J. L. Brett and A. J. E. Rettie, *ChemElectroChem*, 2021, **8**, 1930–1947.

10   F. Han, Y. Zhu, X. He, Y. Mo and C. Wang, *Adv. Energy Mater.*, 2016, **6**, 1–9.

11   R. Asakura, L. Duchêne, R. S. Kühnel, A. Remhof, H. Hagemann and C. Battaglia, *ACS Appl. Energy Mater.*, 2019, **2**, 6924–6930.

12   W. R. Wadt and P. J. Hay, *J. Chem. Phys.*, 1985, **82**, 284–298.

13   P. J. Hay and W. R. Wadt, *J. Chem. Phys.*, 1985, **82**, 270–283.

14   P. J. Hay and W. R. Wadt, *J. Chem. Phys.*, 1985, **82**, 299–310.

15   M. J. Frisch, G. W. Trucks, H. B. Schlegel, G. E. Scuseria, M. A. Robb, J. R. Cheeseman, G.

Scalmani, V. Barone, G. A. Petersson, H. Nakatsuji, X. Li, M. Caricato, A. V. Marenich, J. Bloino, B. G. Janesko, R. Gomperts, B. Mennucci, H. P. Hratchian, J. V. Ortiz, A. F. Izmaylov, J. L. Sonnenberg, Williams, F. Ding, F. Lipparini, F. Egidi, J. Goings, B. Peng, A. Petrone, T. Henderson, D. Ranasinghe, V. G. Zakrzewski, J. Gao, N. Rega, G. Zheng, W. Liang, M. Hada, M. Ehara, K. Toyota, R. Fukuda, J. Hasegawa, M. Ishida, T. Nakajima, Y. Honda, O. Kitao, H. Nakai, T. Vreven, K. Throssell, J. A. Montgomery Jr., J. E. Peralta, F. Ogliaro, M. J. Bearpark, J. J. Heyd, E. N. Brothers, K. N. Kudin, V. N. Staroverov, T. A. Keith, R. Kobayashi, J. Normand, K. Raghavachari, A. P. Rendell, J. C. Burant, S. S. Iyengar, J. Tomasi, M. Cossi, J. M. Millam, M. Klene, C. Adamo, R. Cammi, J. W. Ochterski, R. L. Martin, K. Morokuma, O. Farkas, J. B. Foresman and D. J. Fox, *Gaussian 09, Revis. A. 02*, 2009.

Chapter 3

Investigating the potential of alkali metal plumba-*closo*-dodecaborate ($B_{11}H_{11}Pb^{2-}$) salts as solid-state battery electrolytes

CHAPTER 3 - INVESTIGATING THE POTENTIAL OF ALKALI METAL PLUMBA-*CLOSO*-DODECABORATE ($B_{11}H_{11}Pb^{2-}$) SALTS AS SOLID-STATE BATTERY ELECTROLYTES

3.1 Abstract

Metal dodecaborate salts have been identified as a new class of ion conductor that are highly tuneable. A [B−H] unit within the dodecaborate anion can be replaced with a Pb atom to create a dipole and anisotropy within the anion to tune the crystal structure of alkali metal salts, enhancing ion conductivity for solid-state electrolyte (SSE) applications in batteries. $Li_2B_{11}H_{11}Pb \cdot xH_2O$ shows superionic conductivity up to ~ 7 mS cm^{-1} at 120 °C, proving it comparable to state-of-the-art $LiCB_{11}H_{12}$ at these temperatures. Dehydration of the Li-salt occurs above 120 °C causing changes in the crystal structure and a decrease in the ion conductivity. $Na_2B_{11}H_{11}Pb \cdot xH_2O$ shows modest ion conductivity (0.01 mS cm^{-1} at 170 °C), whereas the potassium salt shows conductivities below 1×10^{-5} mS cm^{-1}. The $B_{11}H_{11}Pb^{2-}$ analogues are proposed to be inferior ion conductors to the $CB_{11}H_{12}^{-}$ varieties due to the divalent $B_{11}H_{11}Pb^{2-}$ anion causing stronger bonding between the cation and anion, possibly higher energy required to move from position to position within the crystal structure. Despite this, the insertion of a lead atom into the dodecaborate cage improves the ion conductivity in comparison to the pristine dodecaborate anion.

3.2 Introduction

Batteries are becoming more prevalent as large-scale energy storage devices due to the increased use of intermittent energy sources including wind and solar. Classical lithium ion batteries contain three main components; a lithium-doped metal oxide cathode (e.g. CoO_2), a graphite anode, and a liquid electrolyte such as $LiPF_6$ in an organic solvent (e.g. ethylene carbonate).[1] Due to the fluidic nature of liquid electrolytes they have high ion conductivity but the organic solvents are prone to leakage and are often volatile and flammable.[2]

Furthermore, the temperature range in which these solvents are in a liquid state is limited (e.g. −20 − 60 °C) so there are freezing and evaporation risks.[3–5] To counteract these drawbacks, and assess alternate battery chemistries, investigations into solid-state electrolytes have recently been revived. Inorganic solids have been known to be good ion conductors since the 19th century, however, it is only recently that they have come to prevalence due to the search for alternatives to traditional liquid electrolytes in battery applications.[6] Studies have shown that solid electrolytes can be more effective due to the possibility for higher power densities.[7]

Boranes have been known for over 100 years since their discovery by Alfred Stock in 1912 and exist from the simplest BH_3 molecule to larger polyhedral borane cages,[8] such as the *closo*-dodecaborate $[B_{12}H_{12}]^{2-}$ dianion. A major characteristic of boranes is their electron deficient nature and also 3-centre 2-electron bonding with bridging hydride for molecules with multiple boron atoms, where these factors help define much of the chemistry in which boranes partake.[9,10] This allows the formation of highly stable multi-vertex borane cages.

One borate of particular interest is the *closo*-dodecaborate dianion $[B_{12}H_{12}]^{2-}$ that has an icosahedral structure with a high degree of symmetry, where metal salts of this anion have shown to have high ion conductivity of the cation.[11,12] Substituting a boron atom with a carbon forms a 12-vertex monocarborate anion $[CB_{11}H_{12}]^-$, which reduces the charge of the anion to monovalent, due to the extra proton in the carbon atom. The asymmetry also creates a dipole within the anion due to the difference in electronegativity between the respective elements.[13,14] The ion conductivity of $[CB_{11}H_{12}]^-$ salts is higher than their borate analogues at lower temperatures,[12] partly hypothesised to be due to the reorientational motion of the asymmetric anion.[15] Despite the promising ion conductivity of $[CB_{11}H_{12}]^-$ salts, there has been little research into the ion conductivity by incorporating other group 14 heteroatoms into the 12-vertex borate cage.

Replacing a [B−H] unit in the $[B_{12}H_{12}]^{2-}$ structure with a Pb atom maintains the −2 charge on the anion and also produces a dipole within the molecule. Pb has a larger atomic radius (2.49 Å) compared to C (1.90 Å) and significantly changes the charge distribution in the anion.[16] Thus, it is postulated that the structural and electronic changes to the anion could affect the ion conductivity of alkali metal salts of plumba-*closo*-dodecaborates, which may allow them to be used as SSEs in battery applications. The synthesis of $B_{11}H_{11}Pb^{2-}$ was reported in 1992, where Chapman *et. al.* published a method where trimethylammonium *nido*-undecaborate $((CH_3)_3NHB_{11}H_{14})$ was reacted with lead(II) chloride in basic conditions at room temperature.[17] Despite the toxicity of PbCl₂, this synthetic method does not require any additional or extreme conditions so it is a preferential route.[18]

This paper focuses on the synthesis and characterisation of alkali metal salts of the plumba-*closo*-dodecaborate dianion ($B_{11}H_{11}Pb^{2-}$) and their use as prospective solid-state electrolytes. The substitution of a carbon atom for a boron atom, the lightest group 14 element, has been proven to improve ion conductivity. As such, substituting with other group 14 elements may also demonstrate improved ion conductivity. Lead is already widely used in Pb-acid batteries and due to the full solid-state nature of the cell, the battery is easier to dispose of and spill risk is eradicated, as a result, the risk of lead poisoning is lower than current lead containing batteries.[19]

3.3 Experimental

3.3.1 Materials and Methods

Nuclear Magnetic Resonance (NMR) spectroscopy was performed on a Bruker AVANCE III 400 MHz spectrometer (128.4 MHz for ^{11}B) with proton decoupled spectra referenced to BF₃·OEt₂. There is a pronounced background signal in ^{11}B spectra due to the presence of borosilicate probe coil inserts in the instrument. An ^{11}B background scan is shown in Figure A1. Fourier

Transform Infrared Attenuated Total Reflectance (FTIR-ATR) spectroscopy using a diamond crystal was performed on all samples on a ThermoFisher Nicolet Summit FTIR Spectrometer. Due to the hygroscopic nature of the compounds, air exposure was minimised to ~ 2 seconds. Each sample was measured from $400 - 4000$ cm^{-1} and averaged over 16 scans. Differential scanning calorimetry (DSC) and Thermogravimetric analysis (TGA) were performed using a Netzsch STA 449 F3 Jupiter apparatus. The samples (~ 4 mg) were placed in a sealed aluminium crucible and heated from 40 to 400 °C (10 °C min^{-1}) in an argon flow of 40 mL min^{-1}. The temperature and sensitivity of the DSC was calibrated using In, Zn, Sn, Bi, and CsCl reference materials, resulting in a temperature accuracy of ± 0.2 °C, while the balance has an accuracy of ± 20 µg. Residual Gas Analysis – Mass Spectroscopy (RGA) was performed on all samples by adding ~ 10 mg to a sealed Swagelok reactor. The reactor was then placed under vacuum and heated at 5 °C min^{-1} from 25 °C to 350 °C. The residual gases evolved from the heating were measured using an RGAPro-2500 (Hy-Energy LLC).

Temperature Programmed Photographic Analysis (TPPA) was performed on the samples by pressing the compounds into pellets (Diameter - 6 mm, Thickness – 1 mm, Pressure – 9800 N (346.6 MPa)) in an inert argon atmosphere. The pellet was placed within a sealed test tube filled with argon gas. The test tube was placed within an aluminium block, which is heated by resistive heating at a rate of 10 °C min^{-1} until 350 °C. The pellet was recorded using a camera to elucidate any physical changes through the heating process.

Electrochemical Impedance Spectroscopy (EIS) was measured using a ZIVE SP1 instrument. The compounds were pressed into pellets, with a diameter of 6 mm and thickness of ~ 1 mm, by applying a pressure of 9800 N (346.6 MPa) in an inert argon atmosphere. A pellet was placed between 2 gold wafers (0.1 mm thickness) and loaded into Teflon sealed sample cells with stainless steel electrodes, which was sealed to maintain an inert atmosphere throughout the test. The data was collected using AC voltage from 1 MHz to 10 Hz. To elucidate the ion conductivity (σ) from the data, the x-intercept (R_{real}) of the Nyquist plot was determined using a known literature method, see Figure A2. [11]

Linear Sweep Voltammetry (LSV) was performed to determine the oxidative stability limit of the sample against Li metal. The method used was based on a method proposed by Han *et. al.* and Asakura *et. al.*.[20,21] $Li_2B_{11}H_{11}Pb \cdot xH_2O$ was mixed with graphite (Sigma Aldrich), previously heated to 550 °C under vacuum for 12 h, in a weight ratio of 75:25 by grinding 5 times with a mortar and pestle. 3 mg of the mixture was layered on top of 40 mg of pure sample and pressed together at 19600 N (693.2 MPa) in an inert argon atmosphere to form a two layered pellet. This pellet was sandwiched to form an Al/Pt/Sample+C/Sample/Li configuration, which was sealed within an air tight Teflon cell. LSV was conducted twice at 60 °C with a scan rate of 50 $\mu V\ s^{-1}$ from 1 V to 5.2 V. The oxidative stability of the material vs Li^+/Li was determined from the intersection point of two linear lines with $R^2 > 0.99$ (the background and the oxidative current).[21]

In situ and ex situ Synchrotron Radiation – X-Ray Diffraction (SR-XRD) data were collected on the powder diffraction (PD) beamline at the Australian Synchrotron using a Mythen strip detector with at a scan rate of 30 secs $scan^{-1}$ using a wavelength of 0.590958(5) Å, refined using NIST LaB_6 660b.[22] All samples were packed in borosilicate capillaries (outer diameter – 0.7mm) and sealed to ensure an argon atmosphere. The samples were heated to 600 K using a hot air blower at 5 °C min^{-1}. Sample temperatures were calibrated against the known lattice parameter of silver as a function of temperature.[23] Crystallographic indexing was performed in Topas v.5 (Bruker, Germany).

Density Functional Theory (DFT) was performed using the B3LYP hybrid functional with a LanL2MB basis set, in order to be able to compute the large number of electrons in the Pb atom.[24–26] The calculations were performed using the software Gaussian G09W optimising geometry and anion energy.[27] Electrostatic Potential (ESP) surfaces were mapped at an isovalue of 5.40 x 10^{29} electrons m^{-3}.

3.3.2 Materials

Lithium hydroxide (98%, −4+14 mesh, anhydrous, Alfa Aesar), anhydrous sodium hydroxide (reagent grade, ≥98%, pellets, Sigma-Aldrich), potassium hydroxide (technical, ≥85% powder, Sigma-Aldrich), lead (II) chloride (98%, Sigma-Aldrich), hydrochloric acid (37%, Fisher), nitric acid (70%, Sigma-Aldrich), methyltriphenylphosponium bromide (98%, Sigma-Aldrich) were all used as purchased or diluted to desired concentrations using Milli-Q water. $(CH_3)_3NHB_{11}H_{14}$ was prepared using the method of Dunks *et. al.* from sodium borohydride (98% (0.5% $MgCO_3$) Sigma-Aldrich) and 1-bromopentane (98%, Sigma-Aldrich) in diglyme (99.5%, anhydrous, Sigma-Aldrich).[28] The synthesis involves dissolving sodium borohydride in diglyme and heating with added 1-bromopentane to 105 °C for 4h. All samples were prepared in air but were stored in a glove box under an inert argon atmosphere.

3.3.3 Synthetic Procedures

3.3.3.1 Synthesis of $M_2B_{11}H_{11}Pb$ (M = Li, Na, K)

The method was adapted from Chapman *et. al.*[17] $(CH_3)_3NHB_{11}H_{14}$ (1.231 g, 6.37 mmol) was dissolved in aqueous MOH (45 mL, 2M, M = Li, Na, K) before $PbCl_2$ (3.713 g, 13.35 mmol) was added and stirred at room temperature for 4 hours. The grey suspension was filtered and the filtrate neutralised to pH 7 using HCl (1M). The resulting grey precipitate was filtered, and the filtrate dried using a rotary evaporator leaving a yellow solid product. The solid was dissolved in CH_3CN (20 mL), to remove the insoluble MCl by-product, filtered and the filtrate dried once more at 150 °C yielding a pale yellow, highly hygroscopic solid, which was stored under an inert atmosphere ($Na_2B_{11}H_{11}Pb$ (0.7752 g, 2.02 mmol, 32% yield) ($Li_2B_{11}H_{11}Pb$ − 34% yield, $K_2B_{11}H_{11}Pb$ − 30% yield). $^{11}B\{^1H\}$ NMR (128 MHz, CD_3CN, ppm) −3.5 (s, 1B), −5.4 (t, $^1J_{^{11}B–^{207}Pb}$ = 263 Hz, 5B), −10.8 (s, 5B). $^1H\{^{11}B\}$ NMR (400 MHz, CD_3CN, ppm) 6.7 (s, 1H), 3.0 (s, 5H), 0.9 (t, $^2J_{^1H–^{207}Pb}$ = 120 Hz, 5B). FTIR (ATR, cm^{-1}) 2420 (vs), 1600 (w), 1050 (m), 730 (m), 700 (w), 520 (m).

3.3.3.2 Synthesis of (MePh₃P)₂B₁₁H₁₁Pb

[(CH₃)₃NH]B₁₁H₁₄ (0.271 g, 1.40 mmol) was dissolved in MOH (20 mL, 2M) before PbCl₂ (1.514 g, 5.45 mmol) was added and stirred at room temperature for 4 hours. The grey suspension was filtered and the filtrate neutralised to pH 7 using HCl (1M) and filtered *in vacuo* once more. MePh₃PBr (1.010 g, 2.83 mmol) was dissolved in milliQ H₂O (10 mL) and added to the filtrate. A yellow solid precipitated and was filtered, washed with milliQ H₂O (2 x 5 mL), and the resulting solid dried at 90 °C under vacuum for 4 hours ((MePh₃P)₂B₁₁H₁₁Pb, 0.8664 g, 0.971 mmol, yield 69 %). ¹¹B {¹H} NMR (128 MHz, CD₃CN, ppm) −3.5 (s, 1B), −5.4 (m, 5B), −10.8 (s, 5B).

3.4 Results and Discussion

The syntheses of $B_{11}H_{11}Pb^{2-}$ salts follow that of the analogous compound, $CB_{11}H_{12}^{-}$. This can be performed from the trimethylammonium salt of the *nido*-undecaborate anion ((CH₃)₃NHB₁₁H₁₄). A $[CB_{11}H_{12}]^{-}$ synthesis pathway proposed by Franken *et. al.,* uses chloroform to form dichlorocarbene, which is inserted into the *nido* cage to form the *closo* 12-vertex product,[29] and was recently made cost effective.[30] This method requires the use of an inert gas atmosphere (*e.g.* argon) at all stages due to the highly reactive carbene intermediate, which must be synthesised *in situ*. However, the formation of the lead analogue is simpler. Heavier group 14 elements such as lead and tin can form stable EX_2 (*E* = Group 14 element, *X* = Halide) compounds so, in the case of PbCl₂, the reaction can be performed in air. Alkali metal $B_{11}H_{11}Pb^{2-}$ salts are soluble in water and organic solvents such as dimethylsulfoxide (DMSO), acetone and acetonitrile.

An insoluble $B_{11}H_{11}Pb^{2-}$ salt can be isolated as shown in reactions 1 and 2.[31]

$$[(CH_3)_3NH][B_{11}H_{14}]_{(s)} + 4\ NaOH_{(aq)} + PbCl_{2\ (s)} \xrightarrow[RT\ 4h]{}$$

$$Na_2B_{11}H_{11}Pb_{(aq)} + 2\ NaCl_{(aq)} + (CH_3)_3N_{(g)} + 4\ H_2O_{(l)} \quad (3.1)$$

$$Na_2B_{11}H_{11}Pb_{(aq)} + 2\ (CH_3)_4NCl_{(aq)} \longrightarrow [(CH_3)_4N]_2B_{11}H_{11}Pb_{(s)} + 2\ NaCl_{(aq)} \quad (3.2)$$
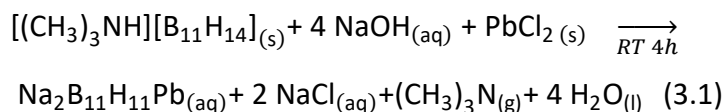
Figure 3.1 shows the electrostatic potential surface of varying borate and heteroborate anions calculated using Gaussian G09W software. Substituting a [B−H] unit with a heteroatom in the 12-membered boron cage produces a pronounced electrostatic dipole. This dipole may be responsible for improving the ion conductivity in $[CB_{11}H_{12}]^-$ compounds with respect to the unsubstituted $[B_{12}H_{12}]^{2-}$ anion.[32] Adding a lead atom into the cage also creates a dipole, similar to the $[CB_{11}H_{12}]^-$, with the main difference between the two anions being the valency, i.e. $[B_{11}H_{11}Pb]^{2-}$ is a divalent anion, whereas the $[CB_{11}H_{12}]^-$ is monovalent. Another difference is the X−B1 (X = B12, C, or Pb (see Figure 3.1)), distance, which increases, respectively, due to the size of the lead atom (4.338 Å) with respect to carbon (3.273 Å) or boron (3.437 Å) as theoretically calculated. However, the calculated overall size, measured from Pb−H1 (where H1 is hydrogen atom bonded to B1), of the $[B_{11}H_{11}Pb]^{2-}$ anion (5.503 Å) is a similar size to both the unsubstituted $[B_{12}H_{12}]^{2-}$ (H12−H1 = 5.833 Å) and the $[CB_{11}H_{12}]^-$ (CH−H1 = 5.524 Å). This is due to the fact that the smaller carbon atom sits further down into the cage, causing a degree of asymmetry. The $B_{12}H_{12}^{2-}$ anion is slightly bigger than the $B_{11}H_{11}Pb^{2-}$ due to the lack of hydrogen atom bonded to the Pb atom, as a result, there is an extra H atom in the full length of the unsubstituted $B_{12}H_{12}^{2-}$ anion. It is expected that cationic coordination to the anion will be impacted by the electrostatic dipole, affecting the solid-state crystal structure of the resulting alkali metal salts (for atomic coordination of the $B_{11}H_{11}Pb^{2-}$ anion as calculated see Table A1). The cationic coordination also depends on the level of coordinated water on the cation, which would buffer the distance between the cation and anion and may impact the mobility of the cation in the crystal.
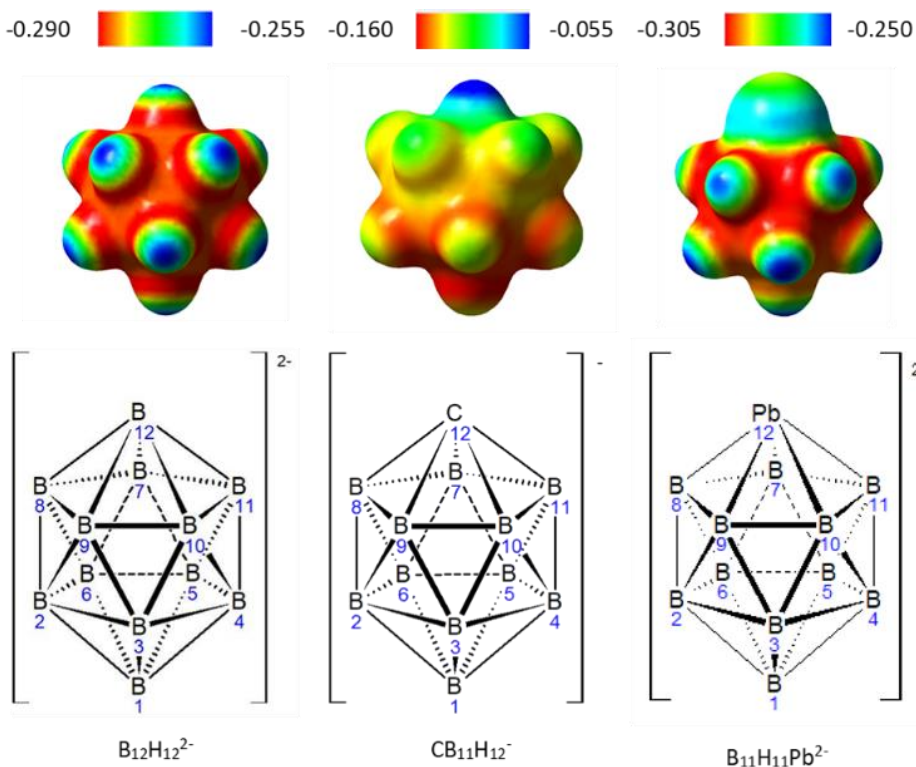
Figure 3.1. Electrostatic potential and structures without hydrogens of various anions using Density Functional Theory (DFT) and a B3LYP/LanM2MB basis set (Total Self-Consistent Field (SCF) Density (isovalue = 0.008)). NOTE: Pb atom in $B_{11}H_{11}Pb^{2-}$ is not protonated.

FTIR spectroscopy data confirms that the spectra of the methyltriphenylphosphine (MePh$_3$P$^+$) $B_{11}H_{11}Pb^{2-}$ salt corresponds to previously published FTIR data (Figure A3).[17] This spectrum shows a large amount of signals in the low-wavenumber fingerprint region. These modes arise from the additional bonding seen in the MePh$_3$P$^+$ cation that contains C-H, C=C aromatic and C-P bonds, in contrast to the alkali metal cations.[33] The corresponding IR active modes contribute to the large number of additional peaks in comparison to the alkali metal salts. The three alkali metal salts have very similar FTIR spectra with the characteristic B−H stretch at 2420 cm^{-1}. However, the lithium compound shows a stronger water signal at both 3500 and 1600 cm^{-1} compared to the sodium and potassium salts. These peaks correspond to an O−H stretch and H−O−H bend, respectively, which arise from coordinated water to the compounds in their crystal structure.[34] Furthermore, the FTIR spectra shows there is an absence of a Pb−H stretch meaning the Pb atom in the anion structure is not protonated as desired.[35]

Furthermore, the Pb atom has a +2 oxidation state which is desirable and any protonation would lead to a higher, more unfavourable oxidation state, as determined by the inert pair effect.[36]

The ^{11}B NMR spectrum of the $B_{11}H_{11}Pb^{2-}$ anion shows three distinct signals at −3.5 (B1), −5.4 (B7−B11), and −10.8 ppm (B2−B6) (Figure 3.2). These resonances are shifted downfield from the non-substituted $B_{12}H_{12}^{2-}$ dianion which has a typical chemical shift of −15.4 ppm, with respect to a $BH_3 \cdot OEt_2$ standard.[37,38] There are three chemical environments for boron within the anion and all hydrogen coupled signals are doublets ($^2J_{B-H}$ = 125.5 Hz) as each boron atom is bonded to a single hydrogen atom (see Figure A4c). ^{11}B integration shows a 1:5:5 ratio, revealing that the −3.5 ppm resonance corresponds to the antipodal boron (B1 − see Figure 3.1 for atom identification) atom with respect to the Pb heteroatom. The large downfield-shift of the antipodal boron (B1) is caused by the introduction of a heteroatom into the cage-like structure, which causes the largest amount of deshielding in the antipodal position.[39] The two upfield resonances correspond to the two different sets of five equivalent boron atoms (B2−B6 and B7−B11). The peak at −5.4 ppm is split further by coupling with a ^{207}Pb nuclei, which is also NMR active ($^1J_{B-Pb}$ = 265.1 Hz), confirming that the peak at −5.4 ppm corresponds to boron atoms directly bonded to the lead atom (B7−B11). The splitting is noticeable because the ^{207}Pb nucleus has a relative natural abundance of 23% with the remainder of the stable isotopes being NMR inactive.[40] This gives an apparent triplet, as 23% of the $B_{11}H_{11}Pb^{2-}$ molecules show a doublet and 77% a singlet. These peaks have the same chemical shift, as a result, the spectrum shows a multiplet with three signals. There is a minor impurity peak at −16 ppm in the spectra, which correspond to the $B_{11}H_{11}^{2-}$ anion that is formed by premature closure of the *nido*-cage without the insertion of the Pb atom (Figure A4b). Other impurities found during synthetic process include unreacted $B_{11}H_{14}^-$ precursor (δ_{11B} = 13.7, −15.5 and −16.9) and its oxidation product, $B_{11}H_{12}O^-$, at 12.8, 11.3, 4.4, −7.0, 14.2, −16.4 and −29.1 ppm.[41,42] The concentrations of these impurities are low and not thought to greatly affect the properties of the bulk materials, as from ^{11}B NMR spectroscopy and SR-XRD, we believe the purity to be >95%. The purity achieved is similar to other materials previously screened for ionic conductivity.[43] All NMR spectra can be found in the supporting information (Figure A4).
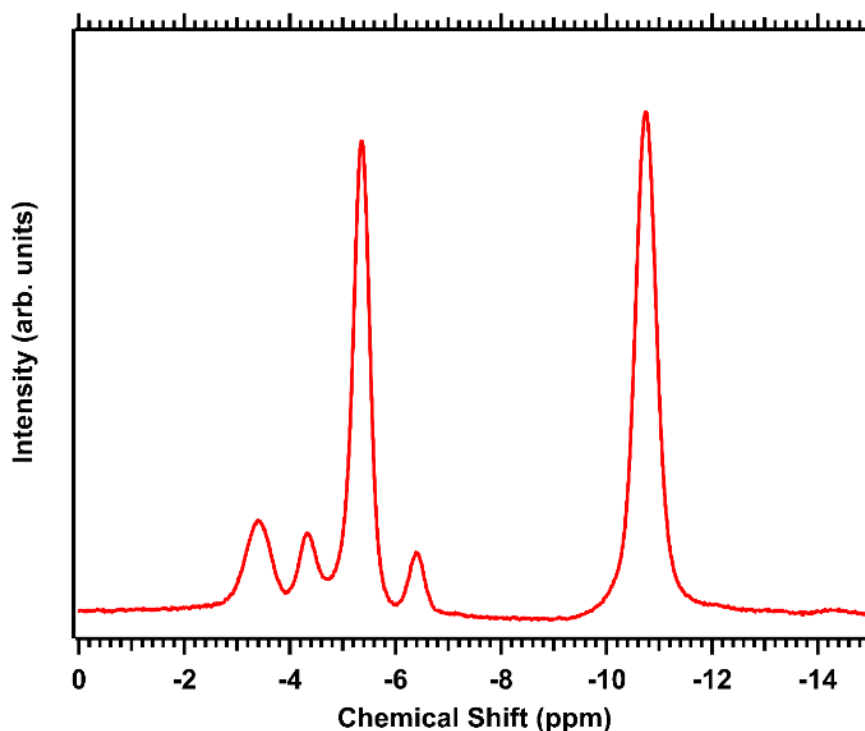
Figure 3.2. ^{11}B {^{1}H} NMR spectrum of Na$_2$B$_{11}$H$_{11}$Pb in CD$_3$CN - −3.5 (s, 1B, B1), −5.4 (m, ^{1}J$_{11B–207Pb}$ = 263 Hz, 5B, B7−B11), −10.8 (s, 5B, B2−B6).

The *in-situ* SR-XRD of Li$_2$B$_{11}$H$_{11}$Pb, performed during thermal treatment, identifies a mixture of at least three different compounds at room temperature (Figure 3.3), considered to be a mixture of different hydrates of Li$_2$B$_{11}$H$_{11}$Pb. *α*-Li$_2$B$_{11}$H$_{11}$Pb·*x*H$_2$O (blue circles) disappears at ~120 °C on heating, causing an increase in scattered intensity in *β*-Li$_2$B$_{11}$H$_{11}$Pb·*x*H$_2$O (green diamond), indicating a potential dehydration event. A similar event occurs at ~170 °C when *β*-Li$_2$B$_{11}$H$_{11}$Pb·*x*H$_2$O disappears and an increase in scattered intensity is seen in *γ*-Li$_2$B$_{11}$H$_{11}$Pb·*x*H$_2$O (purple triangles).

The *α*-phase could not be indexed but *β*-Li$_2$B$_{11}$H$_{11}$Pb·*x*H$_2$O was indexed in space group *P*4$_2$*nm* (102), however, determining the atomic positions was not possible due to the large discrepancy between the combined scattering power of the B$_{11}$H$_{11}$Pb^{2-} anion with the electron-poor Li$^+$ cation. *γ*-Li$_2$B$_{11}$H$_{11}$Pb·*x*H$_2$O persists until 300 °C where decomposition into

Pb metal occurs slightly below the reported melting point at 327.5 °C.[35] This is a lower temperature than unsubstituted $Li_2B_{12}H_{12}$, which shows that it is less stable.[44] The lead is partially molten in the X-ray beam as indicated by the weak crystalline peaks (red squares) coupled by the broad non-crystalline scattering halo at $2\vartheta = 12°$, indicative of a disordered molten phase. All samples see the freezing of lead metal during cooling at ~ 190 °C, which is corroborated by an exothermic event seen in the DSC analysis of the compounds (Figure A5). This is vastly lower than the melting point of lead metal. Possible reasons for this could be the atmosphere within the capillary preventing the crystallisation of the solid, or the amalgamation of the alkali metals into Pb metal after decomposition of the borate causes the reduction of the melting point, however, not to the level seen in this experiment.[45] A minor impurity of lithium chloride (LiCl) also persists throughout the heating ramp, resulting from the slight solubility of lithium chloride in acetonitrile during synthesis. Other solvents, such as acetone, with lower solubilities of lithium chloride, are not used as they cause the $B_{11}H_{11}Pb^{2-}$ anion to decompose.

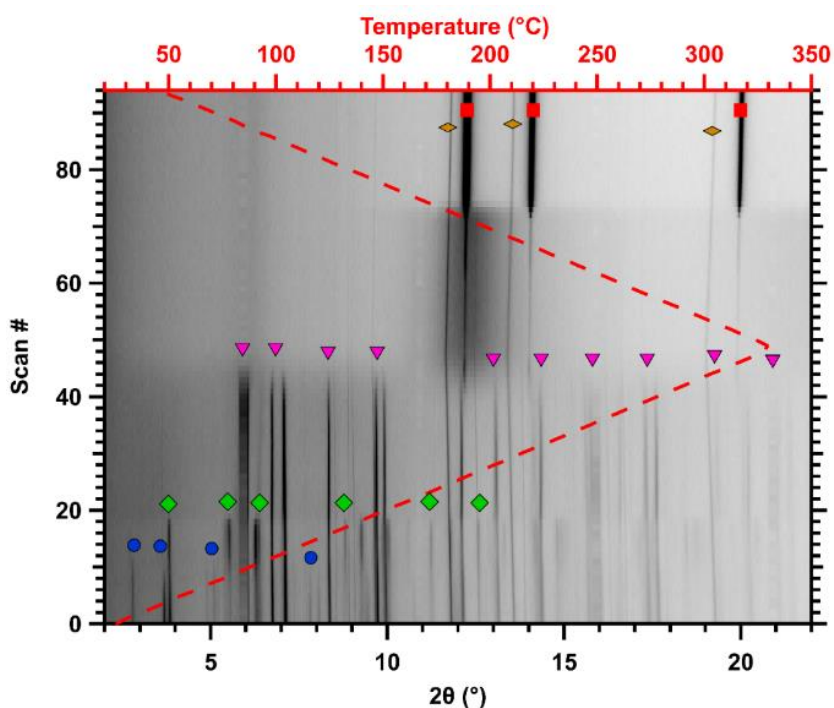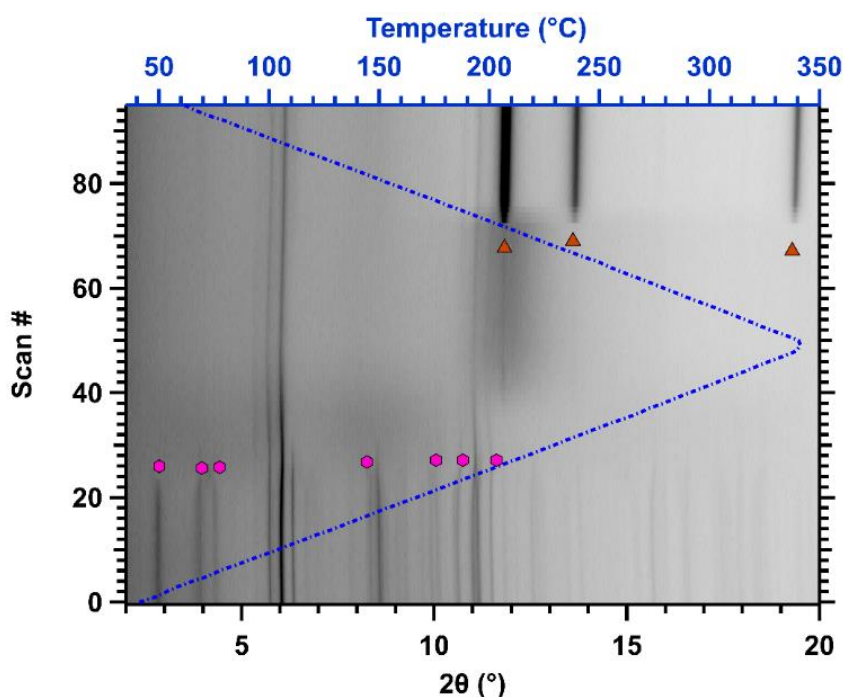**Figure 3.3.** *In-situ* SR-XRD of dried $Li_2B_{11}H_{11}Pb$ under sealed Ar atmosphere and heated to 327 °C at 5 °C min^{-1} – Blue circle = α-$Li_2B_{11}H_{11}Pb \cdot xH_2O$, Green Diamond = β-$Li_2B_{11}H_{11}Pb \cdot xH_2O$, Pink Triangle = γ-$Li_2B_{11}H_{11}Pb \cdot xH_2O$, Red Square = Pb metal, Orange Diamond = LiCl.

The *in-situ* SR-XRD data for $Na_2B_{11}H_{11}Pb$ reveals a first decomposition of α-$Na_2B_{11}H_{11}Pb \cdot xH_2O$ into an amorphous phase, signified by a halo at 210 °C, before full decomposition into lead metal at ~ 300 °C. Sodium chloride is present as an impurity throughout the heating and cooling process (Figure 3.4a). Once more, the presence of molten lead occurs at a lower temperature than its standard melting point. The α-$Na_2B_{11}H_{11}Pb$ shows no dehydration in the initial heating which differs to the lithium salt. The initial phase α-$Na_2B_{11}H_{11}Pb \cdot xH_2O$ could not be indexed, possibly due to a mixture of different compounds or hydrates. The potassium analogue behaves similarly to the sodium variant (Figure 3.4b). The initial phase, α-$K_2B_{11}H_{11}Pb \cdot xH_2O$, decomposes at 220 °C into an amorphous compound which are notoriously difficult to identify, whilst molten Pb forms at 310 °C.[38] As with the lithium salt, both the sodium and potassium salts freeze at 190 °C.
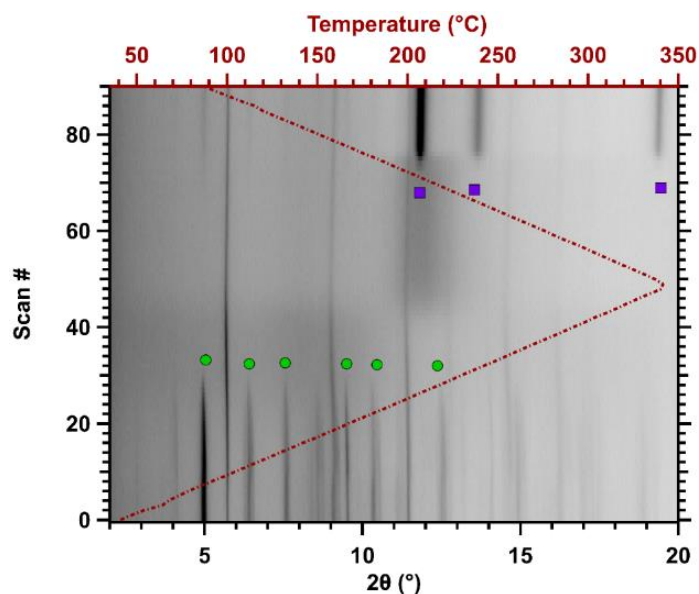
Figure 3.4a. *In-situ* SR-XRD of dried $Na_2B_{11}H_{11}Pb$ under sealed Ar atmosphere and heated to 327 °C at 5 °C min^{-1} – Pink circle = α-$Na_2B_{11}H_{11}Pb.xH_2O$, Brown Triangle = Pb metal. **Figure 3.4b.** *In-situ* SR-XRD of dried $K_2B_{11}H_{11}Pb$ under sealed Ar atmosphere and heated to 327 °C at 5 °C min^{-1} – Green Circle = α-$K_2B_{11}H_{11}Pb.xH_2O$, Blue Square = Pb metal.

Residual Gas Analysis (RGA) was performed on the different salts dried at both 90 °C and 150 °C with the water and hydrogen gas intensities being particularly probed (Figure 3.5). When the samples are dried at 90 °C *in vacuo*, a large amount of water was released for all samples above 90 °C. However, drying at 150 °C removed this coordinated water and reveals a release of water at higher temperatures, $Li_2B_{11}H_{11}Pb$ – 160 °C, $Na_2B_{11}H_{11}Pb$ and $K_2B_{11}H_{11}Pb$ – 240 °C. The evolution of hydrogen gas from a sample indicates the decomposition of the borate cage. The presence of the coordinated water (dried at 90 °C) causes decomposition at a lower temperature for all salts as they begin the evolution of hydrogen gas at ~ 150 °C. Once the majority of this coordinated water has been removed (dried at 150 °C), the decomposition of the compounds occurs at a much higher temperature for all compounds, $Li_2B_{11}H_{11}Pb$ – 220 °C, $Na_2B_{11}H_{11}Pb$ – 260 °C and $K_2B_{11}H_{11}Pb$ – 270 °C.

Temperature Programmed Thermal Analysis of $Li_2B_{11}H_{11}Pb$ (Figure A6a) shows slight discolouration of the pale yellow pellet at ~ 120 °C which correlates with the dehydration observed in the *in-situ* XRD. Further discolouration proceeds at ~ 220 °C until the sample becomes black at ~ 300 °C, which signified full decomposition as seen in the *in-situ* XRD. $Na_2B_{11}H_{11}Pb$ shows decolouration at 210 °C which correlates with the *in-situ* XRD observations (Figure A6b). Further darkening of the pellet continues upon heating coinciding with the evolution of hydrogen as seen in the RGA until 310 °C which correlates to its decomposition shown by XRD. The potassium salt behaves in a similar manner to the sodium analogue with discolouration beginning at ~ 200 °C and full darkening of the pellet at 305 °C which coincides with the decomposition seen in the *in-situ* XRD.
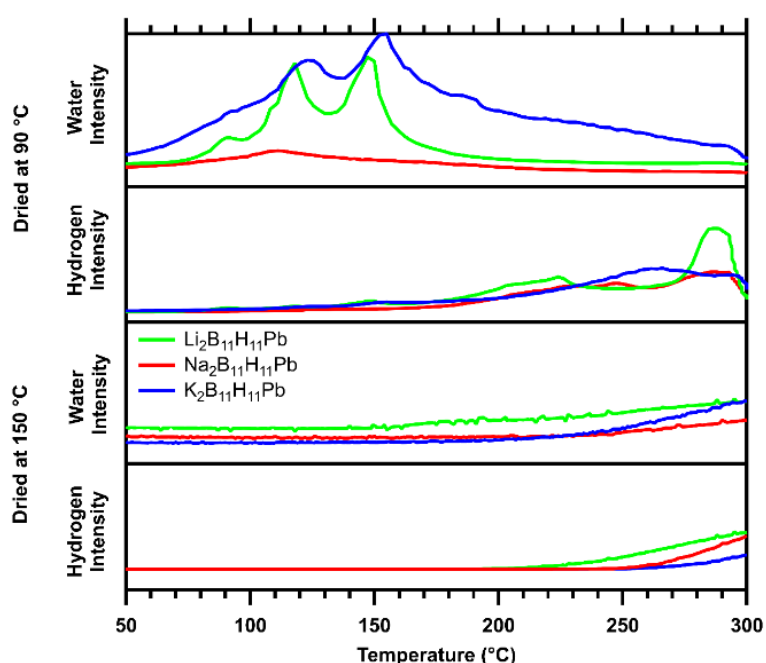
Figure 3.5. RGA Analysis of $Li_2B_{11}H_{11}Pb$, $Na_2B_{11}H_{11}Pb$ and $K_2B_{11}H_{11}Pb$ dried at 90 and 150 °C, heating at 5 °C min^{-1}.

Measuring the ion conductivity of a sample is the primary analytic technique to determine the potential of a compound as a solid-state electrolyte. $Li_2B_{11}H_{11}Pb \cdot xH_2O$ represents the best performing ion conductor in this study, reaching superionic conductivity (> 1 mS cm^{-1}) above 90 °C. Above 120 °C, the ion conductivity decreases again, which corresponds to the initial dehydration step of α-$Li_2B_{11}H_{11}Pb \cdot xH_2O$ observed in the *in-situ* SR-XRD. Between 90 - 120 °C

$Li_2B_{11}H_{11}Pb$ has a greater ion conductivity than the pristine $B_{12}H_{12}^{2-}$ anion (see Figure 3.6a). However, the low conductivity at cooler temperatures ($T < 70$ °C), introduces limitations of $Li_2B_{11}H_{11}Pb \cdot xH_2O$ when compared to $LiCB_{11}H_{12}$. At 40 °C, $LiCB_{11}H_{12}$ has an ion conductivity of ~ 0.3 mS cm^{-1} whereas $Li_2B_{11}H_{11}Pb \cdot xH_2O$ is three orders of magnitude lower at 1 µS cm^{-1} as seen in Figure 3.6a. $Li_2B_{11}H_{11}Pb$ was heated to 100, 150, 200 and 310 °C to determine the stability of the compound through heating. The ^{11}B {^{1}H} NMR spectra (Figure A4k) shows no anion degradation up to 200 °C which is higher than the temperatures at which the ion conductivity was measured. At 310 °C the anion has fully decomposed, matching the *in-situ* SR-XRD results.

One major difference between $CB_{11}H_{12}^-$ and $B_{11}H_{11}Pb^{2-}$ anions is the valency, as the lead containing compound is a divalent anion, the electrostatic attraction between the lithium cations and the anions is increased as seen in Figure 3.1. Furthermore, the $[CB_{11}H_{12}]^-$ is able to be fully dehydrated, whereas the $B_{11}H_{11}Pb^{2-}$ anion is not as seen by FTIR spectroscopy and RGA of the sample.[13] Complete dehydration of alkali metal plumba-*closo*-dodecaborates before decomposition is difficult or not possible once hydrated. The strong charge density of Li^+ and Na^+ cations result in strong coordination of crystal water until high temperatures where the compounds are shown to decompose. This is well-known in this class of compounds with weakly coordinating anions.[12] Despite this, it has been shown that hydration of other metal borates such as $LiB_{11}H_{14}$ and $NaB_{11}H_{14}$ is beneficial towards their ion conductivity due to the creation of a low energy migration pathway through the anionic lattice.[46,47] One reason that the $LiCB_{11}H_{12}$ has exceptional ion conductivity is due to the high temperature polymorphic transition at $\sim$160 °C to a super ion conducting phase with highly mobile anions and cations.[13] The $Li_2B_{11}H_{11}Pb \cdot xH_2O$ does not undergo a high temperature polymorphic transition and so, does not exhibit a step function change in ion conductivity as a function of temperature. The sodium analogue has comparatively poor ion conductivity reaching a maximum of $\sim 10^{-5}$ S cm^{-1} at 170 °C. This is considerably lower than the respective $NaCB_{11}H_{12}$ and also the pristine $NaB_{12}H_{12}$ salt (Figure 3.6b). The potassium salt has very low ion conductivity around the detectable limit (max. 7×10^{-9} S cm^{-1} at 160 °C). This is vastly reduced compared to its contemporaries, KB_3H_8 (3.4×10^{-7} S cm^{-1} at 150 °C), $KB_{11}H_{14}$ (1.2×10^{-4} S cm^{-1} at 150 °C) and $KCB_{11}H_{12}$ (3.2×10^{-4} S cm^{-1}) .[46,48,49]

Linear sweep voltammetry (LSV) was performed on $Li_2B_{11}H_{11}Pb$ to assess the oxidative stability of the compound. This shows the electrochemical limit at which the compound is irreversibly oxidised and therefore the working range of the materials. The limit was found to be 2.3 V vs Li^+/Li which is comparable to other borate salts such as $LiBH_4$, which has a slightly lower oxidative stability of 2.2 V vs Li^+/Li and $LiB_{11}H_{14}.xH_2O$ which is higher at 2.9 V vs Li^+/Li (Figure A7).[21,46] The LSV scan shows a negative initial current and a large positive current after the oxidative stability limit is seen. This is due to the addition of carbon in the cell, which increases background capacitive current, but also increases the accuracy of the oxidative stability limit.[21] Further investigations could involve the investigation of full cells. Possible cathode materials could include Ti_2S for Li and Na batteries.[50,51]
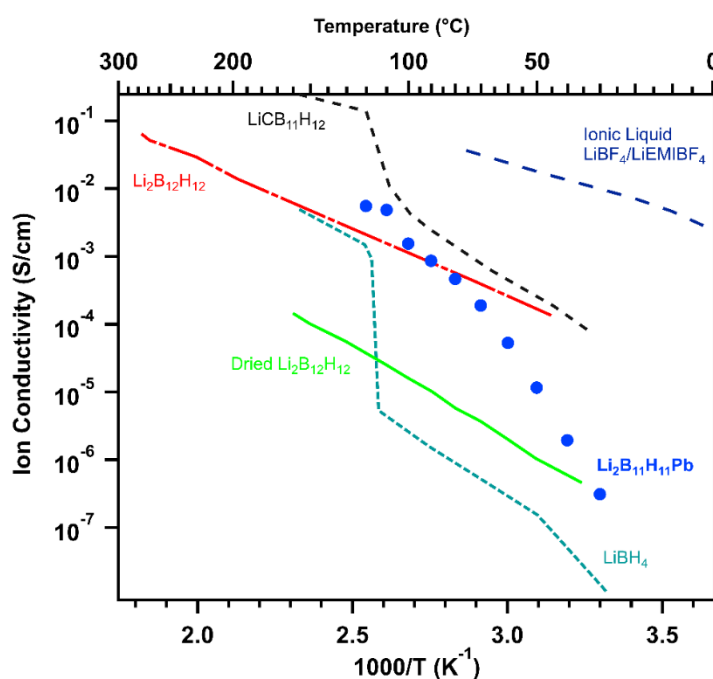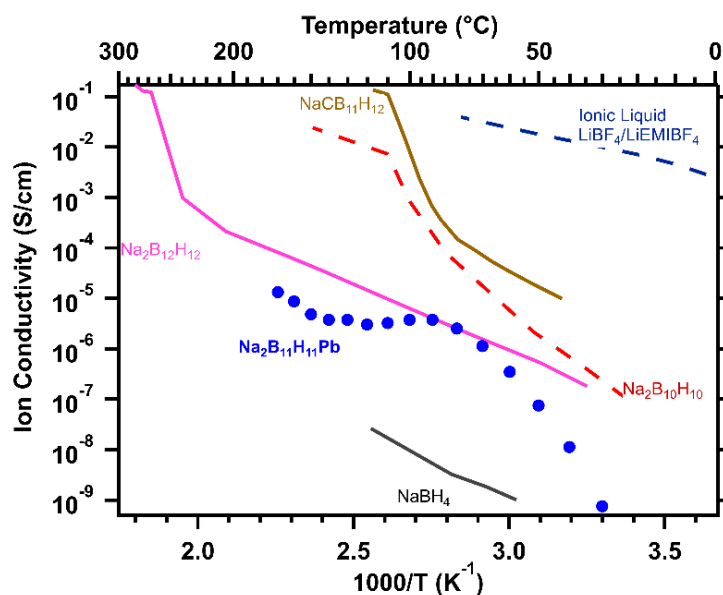
Figure 3.6a. Ion conductivity of various solid state Li $^+$ borate salts. [13,52–55,56] **Figure 3.6b.** Ion conductivity of various solid state Na$^+$ borate salts. [13,52–55]

3.5 Conclusions

A variety of group 1 metal plumba-*closo*-dodecaborate salts were successfully synthesised from trimethylammonium *nido*-undecaborate confirmed using ^{11}B NMR and FTIR spectroscopies. Further, investigation into the properties of this family of compounds using SR-XRD has shown that the crystal structures of these salts are internally different with the space group of $Li_2B_{11}H_{11}Pb$ being identified as *P4$_2$nm* (102). The full crystal structure could not be identified due to the large disparity in the scattering power of the large $B_{11}H_{11}Pb^{2-}$ anions and small Li$^+$ cations. The primary focus of this paper was the identification of these compounds as potential ion conductors to be used in full solid-state battery cells. It has been found that $Li_2B_{11}H_{11}Pb \cdot xH_2O$ has good ion conductivity of > 1 mS cm^{-1} at temperatures of 90 – 120 °C to a maximum of 7 mS cm^{-1} at 120 °C. At higher temperatures, the ion conductivity decreases and this coincides with dehydration of the salt as seen by *in-situ* SR-XRD and confirmed by the release of water vapour seen in the RGA-MS of the sample. Even though, it is surmised that is the divalent nature of the anion is the reason why the ion conductivity is

lower than the $[CB_{11}H_{12}]^-$ variant, there are other factors such as the hydration level and other structural factors which could cause a weaker performance. However, due to the reactive and unstable nature of the anion, further adaptation to the anion was not possible to reduce the valency. Other cations such as Na^+ and K^+ were also synthesised, however, these show poor ion conductivity in comparison to the Li^+ variant and other solid-state borate compounds.

In conclusion, we do not believe that plumba-dodecaborate salts ($B_{11}H_{11}Pb^{2-}$) would be suitable as solid-state electrolytes without further development due to their performance at room temperature in comparison to their contemporaries, such as $CB_{11}H_{12}^-$ salts. However, further development into these materials, for example through ball milling, could improve their performance and as a result their viability. A study into the dynamics of the conduction pathway using QENS or *in* situ NMR would also help gather additional information around this novel class of materials. Future work could include inserting different metals in the borate cage to reduce the charge of the anion to -1 similar to the 12-vertex carborane.

3.6 References

1   Y. Nishi, *J. Power Sources*, 2001, **100**, 101–106.

2   P. G. Balakrishnan, R. Ramesh and T. Prem Kumar, *J. Power Sources*, 2006, **155**, 401–414.

3   H. Wang, G. Wang, S. Yuan, D. Ma, Y. Li and Y. Zhang, *Nano Res.*, 2015, **8**, 1659–1668.

4   E. J. Plichta and W. K. Behl, *J. Power Sources*, 2000, **88**, 192–196.

5   S. Ma, M. Jiang, P. Tao, C. Song, J. Wu, J. Wang, T. Deng and W. Shang, *Prog. Nat. Sci. Mater. Int.*, 2018, **28**, 653–666.

6   K. Funke, *Sci. Technol. Adv. Mater.*, 2013, **14**, 043502.

7   S. Zhuiykov, T. Ono, N. Yamazoe and N. Miura, *Solid State Ionics*, 2002, **152**–**153**, 801–807.

8   I. B. Sivaev, V. I. Bregadze and S. Sjöberg, *Collect. Czechoslov. Chem. Commun.*, 2002, **67**, 679–727.

9   J. C. Green, M. L. H. Green and G. Parkin, *Chem. Commun.*, 2012, **48**, 11481–11503.

10   R. W. Parry and L. J. Edwards, *J. Am. Chem. Soc.*, 1959, **81**, 3554–3560.

11   B. R. S. Hansen, M. Paskevicius, M. Jørgensen and T. R. Jensen, *Chem. Mater.*, 2017, **29**, 3423–3430.

12   B. R. S. Hansen, M. Paskevicius, H. W. Li, E. Akiba and T. R. Jensen, *Coord. Chem. Rev.*, 2016, **323**, 60–70.

13   W. S. Tang, A. Unemoto, W. Zhou, V. Stavila, M. Matsuo, H. Wu, S. I. Orimo and T. J. Udovic, *Energy Environ. Sci.*, 2015, **8**, 3637–3645.

14   M. Jørgensen, P. T. Shea, A. W. Tomich, J. B. Varley, M. Bercx, S. Lovera, R. Černý, W. Zhou, T. J. Udovic, V. Lavallo, T. R. Jensen, B. C. Wood and V. Stavila, *Chem. Mater.*, 2020, **32**, 1475–1487.

15   T. J. Udovic, M. Matsuo, A. Unemoto, N. Verdal, V. Stavila, A. V. Skripov, J. J. Rush, H. Takamura and S. I. Orimo, *Chem. Commun.*, 2014, **50**, 3750–3752.

16   M. Rahm, R. Hoffmann and N. W. Ashcroft, *Chem. - A Eur. J.*, 2016, **22**, 14625–14632.

17   R. W. Chapman, J. G. Kester, K. Folting, W. E. Streib and L. J. Todd, *Inorg. Chem.*, 1992, **31**, 979–983.

18   R. A. Goyer, *Environ. Health Perspect.*, 1993, **100**, 177–187.

19   P. Ruetschi, *J. Power Sources*, 1977, **2**, 3–120.

20   F. Han, Y. Zhu, X. He, Y. Mo and C. Wang, *Adv. Energy Mater.*, 2016, **6**, 1–9.

21   R. Asakura, L. Duchêne, R. S. Kühnel, A. Remhof, H. Hagemann and C. Battaglia, *ACS Appl. Energy Mater.*, 2019, **2**, 6924–6930.

22   D. R. Black, D. Windover, A. Henins, J. Filliben and J. P. Cline, *Powder Diffr.*, 2011, **26**, 155–158.

23   I. K. Suh, H. Ohta and Y. Waseda, *J. Mater. Sci.*, 1988, **23**, 757–760.

24   W. R. Wadt and P. J. Hay, *J. Chem. Phys.*, 1985, **82**, 284–298.

25   P. J. Hay and W. R. Wadt, *J. Chem. Phys.*, 1985, **82**, 270–283.

26   P. J. Hay and W. R. Wadt, *J. Chem. Phys.*, 1985, **82**, 299–310.

27   M. J. Frisch, G. W. Trucks, H. B. Schlegel, G. E. Scuseria, M. A. Robb, J. R. Cheeseman, G. Scalmani, V. Barone, G. A. Petersson, H. Nakatsuji, X. Li, M. Caricato, A. V. Marenich, J. Bloino, B. G. Janesko, R. Gomperts, B. Mennucci, H. P. Hratchian, J. V. Ortiz, A. F. Izmaylov, J. L. Sonnenberg, Williams, F. Ding, F. Lipparini, F. Egidi, J. Goings, B. Peng, A. Petrone, T. Henderson, D. Ranasinghe, V. G. Zakrzewski, J. Gao, N. Rega, G. Zheng, W. Liang, M. Hada, M. Ehara, K. Toyota, R. Fukuda, J. Hasegawa, M. Ishida, T. Nakajima, Y. Honda, O. Kitao, H. Nakai, T. Vreven, K. Throssell, J. A. Montgomery Jr., J. E. Peralta, F. Ogliaro, M. J. Bearpark, J. J. Heyd, E. N. Brothers, K. N. Kudin, V. N. Staroverov, T. A. Keith, R. Kobayashi, J. Normand, K. Raghavachari, A. P. Rendell, J. C. Burant, S. S. Iyengar, J. Tomasi, M. Cossi, J. M. Millam, M. Klene, C. Adamo, R. Cammi, J. W. Ochterski, R. L. Martin, K. Morokuma, O. Farkas, J. B. Foresman and D. J. Fox, *Gaussian 09, Revis. A. 02*, 2009.

28   G. B. Dunks, K. Barker, E. Hedaya, C. Hefner, K. Palmer-Ordonez and P. Remec, *Inorg. Chem.*, 1981, **20**, 1692–1697.

29   A. Franken, B. T. King, J. Rudolph, P. Roa, B. C. Noll and J. Michl, *Collect. Czechoslov. Chem. Commun.*, 2001, **66**, 1238–1249.

30   A. Berger, C. E. Buckley and M. Paskevicius, *Inorg. Chem.*, 2021, **60**, 14744–14751.

31   J. Plešek, K. Baše, F. Mareš, F. Hanousek, B. Štíbr and S. Heřmánek, *Collect. Czechoslov. Chem. Commun.*, 1984, **49**, 2776–2789.

32   S. P. Fisher, A. W. Tomich, S. O. Lovera, J. F. Kleinsasser, J. Guo, M. J. Asay, H. M. Nelson and V. Lavallo, *Chem. Rev.*, 2019, **119**, 8262–8290.

33   L. W. Daasch and D. C. Smith, *Anal. Chem.*, 1951, **23**, 853–868.

34   J. Coates, *Encycl. Anal. Chem.*, 2004, 1–23.

35   D. R. Lide, *CRC Handbook of Chemistry and Physics*, CRC, Boca Raton, 85th edn., 2004.

36   M. Seth, K. Faegri and P. Schwerdtfeger, *Angew. Chemie - Int. Ed.*, 1998, **37**, 2493–2496.

37   S. Garroni, C. Milanese, D. Pottmaier, G. Mulas, P. Nolis, A. Girella, R. Caputo, D. Olid, F. Teixdor, M. Baricco, A. Marini, S. Suriñach and M. D. Baró, *J. Phys. Chem. C*, 2011, **115**, 16664–16671.

38   M. Paskevicius, L. H. Jepsen, P. Schouwink, R. Černý, D. B. Ravnsbæk, Y. Filinchuk, M. Dornheim, F. Besenbacher and T. R. Jensen, *Chem. Soc. Rev.*, 2017, **46**, 1565–1634.

39   F. Teixidor, C. Viñas and R. W. Rudolph, *Inorg. Chem.*, 1986, **25**, 3339–3345.

40 M. Komárek, V. Ettler, V. Chrastný and M. Mihaljevič, *Environ. Int.*, 2008, **34**, 562–577.

41 E. I. Tolpin and W. N. Lipscomb, *J. Am. Chem. Soc.*, 1973, **95**, 2384–2386.

42 X. Yang, H. Jiao and P. Von Rague Schleyer, *Inorg. Chem.*, 1997, **36**, 4897–4899.

43 S. H. Payandeh, D. Rentsch, Z. Łodziana, R. Asakura, L. Bigler, R. Černý, C. Battaglia and A. Remhof, *Adv. Funct. Mater.*, 2021, **31**, 2010046.

44 M. P. Pitt, M. Paskevicius, D. H. Brown, D. A. Sheppard and C. E. Buckley, *J. Am. Chem. Soc.*, 2013, **135**, 6930–6941.

45 D. Martelli, A. Venturini and M. Utili, *Fusion Eng. Des.*, 2019, **138**, 183–195.

46 D. H. P. Souza, K. T. Møller, S. A. Moggach, T. D. Humphries, A. M. D'Angelo, C. E. Buckley and M. Paskevicius, *J. Mater. Chem. A*, 2021, **9**, 15027–15037.

47 T. R. Jensen, *Phys. Chem. Chem. Phys.*, 2020, **22**, 9204.

48 J. B. Grinderslev, K. T. Møller, Y. Yan, X. M. Chen, Y. Li, H. W. Li, W. Zhou, J. Skibsted, X. Chen and T. R. Jensen, *Dalt. Trans.*, 2019, **48**, 8872–8881.

49 M. Dimitrievska, H. Wu, V. Stavila, O. A. Babanova, R. V. Skoryunov, A. V. Soloninin, W. Zhou, B. A. Trump, M. S. Andersson, A. V. Skripov and T. J. Udovic, *J. Phys. Chem. C*, 2020, **124**, 17992–18002.

50 M. Latroche, D. Blanchard, A. El, B. C. Hauback, T. R. Jensen, P. E. De Jongh, S. Kim, N. S. Nazer, P. Ngene, S. Orimo, D. B. Ravnsb and V. A. Yartys, *J. Hydrog. Energy*, 2019, **44**, 7878–7887.

51 K. Yoshida, T. Sato, A. Unemoto, M. Matsuo, T. Ikeshoji, T. J. Udovic and S. Orimo, *Appl. Phys. Lett.*, 2017, **110**, 103901.

52 L. He, H. W. Li, H. Nakajima, N. Tumanov, Y. Filinchuk, S. J. Hwang, M. Sharma, H. Hagemann and E. Akiba, *Chem. Mater.*, 2015, **27**, 5483–5486.

53 Y. Sadikin, M. Brighi, P. Schouwink and R. Černý, *Adv. Energy Mater.*, 2015, **5**, 1501016.

54 T. J. Udovic, M. Matsuo, W. S. Tang, H. Wu, V. Stavila, A. V. Soloninin, R. V. Skoryunov, O. A. Babanova, A. V. Skripov, J. J. Rush, A. Unemoto, H. Takamura and S. I. Orimo, *Adv. Mater.*, 2014, **26**, 7622–7626.

55 H. Rickert, *Angew. Chemie Int. Ed. English*, 1978, **17**, 37–46.

56   A. Unemoto, K. Yoshida, T. Ikeshoji and S. Orimo, 2016, **57**, 1639–1644.

Chapter 4

Stannaborates: Tuning the Ion Conductivity of Dodecaborate Salts with Tin Substitution

Thomas A. Hales, Anita M. D'Angelo, Kasper T. Møller, Craig E. Buckley, Terry D. Humphries and Mark Paskevicius, *Phys. Chem. Chem. Phys.*,(Advance Article))

CHAPTER 4 - STANNABORATES: TUNING THE ION CONDUCTIVITY OF DODECABORATE SALTS WITH TIN SUBSTITUTION

4.1 Abstract

Metal substituted dodecaborate anions can be coupled with alkali metal cations to have great potential as solid-state ion conductors for battery applications. A tin atom can replace a B-H unit within an unsubstituted dodecaborate cage to produce a stable, polar divalent anion. The chemical and structural change in forming a stannaborate results in a modified crystal structure of respective group 1 metal salts, and as a result, improves the material's ion conductivity. $Li_2B_{11}H_{11}Sn$ shows high ion conductivity of ~ 8 mS cm^{-1} at 130 °C, similar to the state-of-the-art $LiCB_{11}H_{12}$ at these temperatures, however, obtaining high ion conductivity at room temperature is not possible with pristine alkali metal stannaborates.

4.2 Introduction

Energy storage devices are vital to solidify a green future as they allow renewable energy from intermittent sources to be stored and redistributed whenever needed throughout the day. Current electrical storage devices, or batteries, as they are more commonly known, traditionally contain two solid electrodes and a liquid electrolyte, e.g. containing a lithium salt in an organic solvent such as diethylene carbonate.[1] The role of the electrolyte is to allow ions to be transported from one electrode to the other. However, these liquid electrolytes have severe drawbacks for large scale energy storage, for example, they are flammable and volatile.[2] Also, liquid electrolytes do not allow for pure metal (e.g. lithium) electrodes to be used due to dangerous dendrite growth.[3] One way to combat these issues is to use a complete solid-state construction for the battery. This all-solid-state battery contains a solid-state

electrolyte, which allows small metal cations to migrate through an anionic crystal lattice between the two solid electrodes.[4] Furthermore, an elemental metal cathode can be used which helps reduce the cost of the cell, improve the voltage window, and reduce the size and weight.[4]

There are many different types of compounds that have shown potential to be used as solid-state electrolytes. The most prevalent of these are inorganic ceramic solids such as sulphides (e.g. $Li_{10}GeP_2S_{12}$) and silicates (e.g. $Na_3Zr_2PSi_2O_{12}$).[5,6] They show promise due to the high lability of the respective lithium and sodium ions, resulting in high ion conductivity, especially at high temperature (> 100 °C), and importantly they are chemically stable with oxidative stabilities of 2.1 V for $Li_{10}GeP_2S_{12}$.[7] Inorganic solids, such as sulphides, are already being commercially used alongside a lithium metal anode and a lithium manganese oxide ($LiMn_2O_4$) cathode.[8] Other types of materials proposed as possible solid-state electrolytes are solvent-free salts or polymers. Polymeric electrolytes operate by the migration of metal ions through the polymer chain between the two electrodes, for example, in the work reviewed by Yue *et al.* where a variety of polymer mixtures are used to produce high ion conductivity levels.[9]

Borohydride salts have been shown to have high ion conductivity, in particular at high temperatures.[10] This is especially true for cluster borate salts, for example, *closo*-dodecaborate salts ($[B_{12}H_{12}]^{2-}$). These anions have been paired with different alkali metal cations such as lithium, sodium, and potassium and show excellent ionic conductivity performance at elevated temperatures, for example, $Li_2B_{12}H_{12}$ (8 x 10^{-2} S cm^{-1} at 280 °C), $Na_2B_{10}H_{10}$ (2 x 10^{-2} S cm^{-1} at 150 °C), and $KB_{11}H_{14}$ (1×10^{-4} S cm^{-1} at 150 °C).[11–14]

Substituted *closo*-dodecaborate cages have been known to improve the ion conductivity at lower temperatures in comparison to unsubstituted $B_{12}H_{12}{}^{2-}$ salts. $LiCB_{11}H_{12}$ and $NaCB_{11}H_{12}$ shows vastly improved performance at room and elevated temperature ($LiCB_{11}H_{12} \sim 0.1$ S cm^{-1} at 120 °C), even for divalent cations.[11,15] The insertion of a carbon atom creates a dipole within the boron anion and changes the anion reorientational dynamics, which is believed to increase the ion conductivity.[16,17] Metal cations diffuse through the anionic lattice, possibly through a paddle-wheel mechanism, which reduces cation hopping energy and as a result improves the ion conductivity at a specific temperature.[18] Introducing a lead atom into the anion was also seen to show high ionic conductivity, however, not to the level of the 12-vertex carborane.[19] The lower ion conductivity displayed by these plumba-*closo*-dodecaborates

could possibly be explained by them not demonstrating a polymorphic phase transition to a structure with high reorientational dynamics, which is present in the carboranes.

Stannaborates ($B_{11}H_{11}Sn^{2-}$ compounds) have been known for 30 years since their discovery by Chapman et al.[20] The prototypical stannaborate, $[Ph_3MeP]_2[B_{11}H_{11}Sn]$, was synthesised from a nido-borane precursor, $B_{11}H_{14}^-$, and has since been modified into a variety of different salts (e.g. NBu_4^+).[21] These compounds have been used in coordination chemistry, coordinating from the tin atom to a variety of metal centres such as Mo, Ru, and Ni.[21,22] When the salts are synthesised, they are usually coupled with a bulky organic cation and they have not yet been explored in regard to their ion conductivity. While organic cations are particularly useful in coordination chemistry, they cannot be used as solid-state electrolytes in battery applications. For this purpose, salts with a metal cation must be used. Solvated lithium and cesium stanna-closo-dodecaborates have previously been synthesised, and the synthesis of similar alkali metal salts with a $B_{11}H_{11}Pb^{2-}$ anion have also been achieved.[19,23] The aim of this research is to synthesise and characterise a variety of alkali metal stannaborate salts for their potential use as solid-state ion conductors.

4.3 Experimental

Density Functional Theory (DFT) was performed using the B3LYP hybrid functional with a LanL2MB basis set, in order to process the large Sn atom.[24–26] The calculations were performed using the software Gaussian G09W, optimising geometry and anion energy.[27] Electrostatic Potential (ESP) surfaces were mapped at an isovalue of 0.008 electrons/bohr^3. Atomic coordinates of the $B_{11}H_{11}Sn^{2-}$ anion are shown in Table S1.

Nuclear Magnetic Resonance (NMR) spectroscopy was performed on a Bruker AVANCE III 400 MHz spectrometer (128.4 MHz for ^{11}B) with proton decoupled spectra referenced to $BF_3 \cdot OEt_2$ and Me_4Si respectively using a CD_3CN solvent.

Differential scanning calorimetry (DSC) was performed using a Netzsch STA 449 F3 Jupiter. The samples ($\sim$ 4 mg) were placed in a sealed aluminium crucible with a pinhole pierced into the lid and heated from 40 - 400 °C (10 °C min^{-1}) in an argon flow of 40 mL min^{-1}. The

temperature and sensitivity of the DSC was calibrated using In, Zn, Sn, Bi, and CsCl reference materials, resulting in a temperature accuracy of ± 0.2 °C.

Electrochemical Impedance Spectroscopy (EIS) was measured using a ZIVE SP1 instrument. The compounds were pressed into pellets, with a diameter of 6 mm and thickness of ~ 1 mm, by applying a pressure of 1000 kg in an inert argon atmosphere. A pellet was placed between 2 gold wafers (0.1 mm thickness) and loaded into sealed Teflon sample cells with stainless steel electrodes under argon. The data were collected using AC voltage from 1 MHz to 10 Hz. To elucidate the ion conductivity (σ) from the data, the x-intercept (Z_{real}) of the Nyquist plot was determined using a known literature method, see Figure B1. [28]

Linear Sweep Voltammetry (LSV) was performed to determine the oxidative stability limit of the $Li_2B_{11}H_{11}Sn$ salt against Li metal. The method used was based on a method proposed by Han *et al.* and Asakura *et al.* [7,29] $Li_2B_{11}H_{11}Sn$ was mixed with graphite (Sigma Aldrich, powder < 20 µg), previously heated to 550 °C under vacuum for 12 h, in a weight ratio of 75:25 by grinding 5 times with a mortar and pestle. 3 mg of the mixture was layered on top of 40 mg of pristine $Li_2B_{11}H_{11}Sn$ and pressed together at 2000 kg in an inert argon atmosphere to form a two layered pellet. This pellet was sandwiched to form an Al/Pt/Sample+C/Sample/Li configuration, which was sealed within an air-tight Teflon cell. LSV was conducted at 60 °C with a scan rate of 50 µV s^{-1} from the open circuit voltage (2.3 V) to 8 V. A second LSV cycle was also conducted from 1 - 5.2 V at the same scan rate and temperature to verify subsequent reactions. The oxidative stability of the material was determined from the intersection point of the background and the oxidative current.[29]

In-situ and ex situ Synchrotron Radiation – X-Ray Diffraction (SR-XRD) data were collected on the powder diffraction (PD) beamline at the Australian Synchrotron using a Mythen-II strip detector with at a scan rate of 30 secs scan^{-1} using a wavelength of 0.59096(1) Å. All samples were packed in borosilicate capillaries (inner diameter – 0.7 mm) and flame sealed under an argon atmosphere. The samples were heated to 327 °C using a hot air blower at 5 °C min^{-1}. Sample temperatures were calibrated against the known lattice parameter of silver as a function of temperature.[30] Crystallographic indexing was performed in Topas v.5 (Bruker, Germany).

Raman Spectroscopy was performed using a WITec Alpha 300 SAR confocal Raman microscope with a 532 nm green light excitation wavelength and 600 grating/mm. Samples were prepared in 1 mm wide borosilicate capillaries in an Ar filled glovebox then flame sealed to prevent exposure to air and moisture. Spectra were collected with 100 accumulations with an integration time of 400 ms. Data processing including background subtraction was performed using Project 4 (WITec) software.

Lithium hydroxide (98%, −4 +1 4 mesh, anhydrous, Alfa Aesar), anhydrous sodium hydroxide (reagent grade, ≥ 98%, pellets, Sigma-Aldrich), potassium hydroxide (technical, ≥ 85% powder, Sigma-Aldrich), tin (II) chloride (98%, Sigma-Aldrich), and hydrochloric acid (37%, Fisher) were all used as purchased or diluted to desired concentrations using Milli-Q water. $(CH_3)_3NHB_{11}H_{14}$ was prepared using the method of Dunks et $al.$ from sodium borohydride (98% (0.5% $MgCO_3$), Sigma-Aldrich) and 1-bromopentane (98%, Sigma-Aldrich) in diglyme (99.5%, anhydrous, Sigma-Aldrich).[31] The synthesis involves dissolving sodium borohydride in diglyme followed by the drop-wise addition of 1-bromopentane at 105 °C for 4h, and subsequent room temperature precipitation from water using trimethylammonium chloride (Sigma-Aldrich). All samples were prepared and stored under an inert argon atmosphere.

4.3.1 Synthesis of $Li_2B_{11}H_{11}Sn$

The synthesis method was an adaption of that reported by Gädt and Wesemann.[23] $(CH_3)_3NHB_{11}H_{14}$ (2.600 g, 13.46 mmol) was dissolved in anhydrous tetrahydrofuran (THF) (40 mL) and cooled to 0 °C before n-butyllithium (30 mL) was added dropwise and the solution was stirred for 30 minutes under an inert argon atmosphere. Tin (II) chloride (3.70 g, 19.51 mmol) dissolved in THF (30 mL) was added dropwise to the pale yellow solution at room temperature. The solution turned deep red instantaneously and was stirred for a further 4 hours at room temperature. THF was removed using rotary evaporation and the dry product was dissolved in aqueous lithium hydroxide (1M, 50 mL) to extract the product from the resulting mixture. The solution was filtered in $vacuo$ and the filtrate neutralised to pH 7 using HCl (1 M). The solvent was removed in $vacuo$ and acetonitrile (15 mL) was added to the resulting solid, which helps to remove the LiCl by-product. The suspension was filtered and

the filtrate was dried *in vacuo* at 150 °C leaving a pale yellow, highly hygroscopic solid, which was stored under argon, $Li_2B_{11}H_{11}Sn$ (2.083 g, 7.93 mmol, 59% yield). ^{11}B {^1H} NMR (128 MHz, CD_3CN) −5.3 (s, 1B), -11.1 (s, 5B), -12.4 (s, 5B). ^1H {^{11}B} NMR (400 MHz, CD_3CN) 2.98 (s, 1H), 1.60 (s, 5H), 0.82 (s, 5B).

4.3.2 Synthesis of $M_2B_{11}H_{11}Sn$ (M = Na, K)

$Li_2B_{11}H_{11}Sn$ (0.215 g, 0.819 mmol) was dissolved in water (5 mL) and passed through a column containing Amberlite® IR 120 hydrogen form ion exchange resin. The resulting acidic solution was treated with the relevant metal hydroxide (NaOH or KOH) until pH 7. The water was removed *in vacuo* at 150 °C leaving the desired product, $Na_2B_{11}H_{11}Sn$ (0.201 g, 84% yield) or $K_2B_{11}H_{11}Sn$ (68% yield).

4.4 Results and Discussion

The use of a stannaborate salt as a solid-state electrolyte provides an alternative to a carborane salt, which may hold similar anionic polarity due to the similarity between charge distribution in the anion. It is postulated that a polarised anionic charge distribution may allow for favourable reorientational anion dynamics in the solid-state, thus providing similar levels of high ion conductivity as the carborane. The replacement of Sn for C-H may also change the temperature at which rapid reorientational dynamics are observed via a lower temperature polymorphic phase transition. To understand the charge distribution in the stannaborate anion a theoretical calculation can be undertaken computationally and compared to similar anions. Figure 4.1 shows the calculated electrostatic potential surfaces of various borane anions. The introduction of a heteroatom into the 12-vertex borane anion creates a permanent electrostatic dipole with electron density moving away from the heteroatom in the case of carborane. The lithium and sodium salts of the 12-vertex carborane ($CB_{11}H_{12}^-$) show vastly improved ion conductivity compared with the respective unsubstituted $B_{12}H_{12}^{2-}$ salts.[11] The overall charge is higher for the divalent $B_{11}H_{11}Sn^{2-}$ anion compared to the

monovalent $CB_{11}H_{12}^-$. A major difference between the carborane and stannaborate anions is the fact that the carbon is protonated, whilst the tin atom is not. As such, it is clear from Figure 4.1 that whilst the C-H unit in the carborane forms a less-negative node, the Sn atom forms a more-negative node, in contrast to the B-H units in the respective anions. Despite the different charge distribution in the stannaborate compared to carborane anion, a noticeable polarity to the charge is present. The length of the $B_{11}H_{11}Sn^{2-}$, measured from Sn-H1 is 5.446 Å, which is similar to the total length of $CB_{11}H_{12}^-$ (5.524 Å when measured CH-H1) despite the Sn not being protonated. This is due to the disproportionate size of the tin atom being similar to a C-H unit. The unsubstituted $B_{12}H_{12}^{2-}$ is slightly larger (5.833 Å) than the carborane due to the fact the carbon atom sits further down into the cage. The resulting crystal structure of a solid-state salt can be influenced by the charge distribution of the ions. In the case of respective borates, the anionic polarity (or lack of) will affect the respective cation locations with respect to the anion due to electrostatic forces and steric constraints.[32] The resulting crystal structure will change the cationic conductive mechanisms and pathways through the anionic lattice. Therefore, the calculated charge distribution of the stannaborate anion provides indications that it may form favourable alkali metal salts.
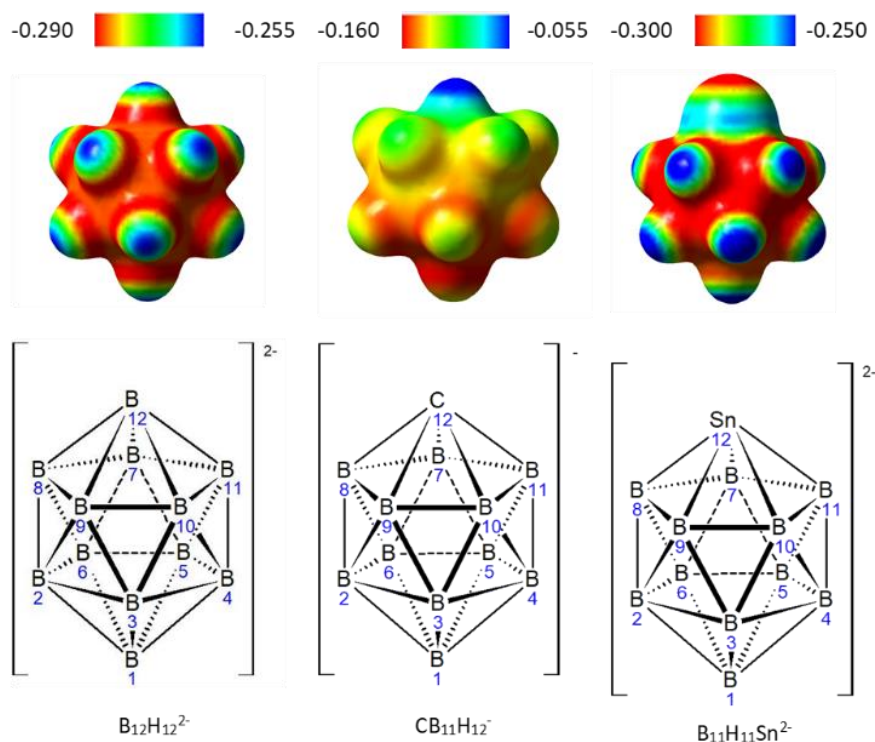
Figure 4.1. Electrostatic potential surfaces and structures (without hydrogen shown) of *closo*-borate anions optimised and generated using a B3LYP/LanM2MB basis set (Total Self-Consistent Field (SCF) Density (isovalue = 0.008)). NOTE: Sn atom is not protonated.

The synthesis of the $B_{11}H_{11}Sn^{2-}$ anion follows the same synthetic pathways as its sister compounds $CB_{11}H_{12}^-$ and $B_{11}H_{11}Pb^{2-}$.[20,33] An open 11-vertex borane anion ($B_{11}H_{14}^-$) is deprotonated by a base and a non-boron heteroatom is inserted into the anion to form a *closo*-undecaborate anion containing the atom of choice. The method used follows that described by Chapman *et al.* using a $Me_3NHB_{11}H_{14}$ precursor treated with a strong base, in this case *n*BuLi, and reacted with $SnCl_2$ in a THF solvent under an inert atmosphere.[20] Due to the increased stability of $SnCl_2$ compared with its carbon analogue, CCl_2, which can only be made *in-situ*, it can instead be added directly as a reagent. This synthetic route has also previously been used to synthesise stannaborate salts with bulky organic cations or solvated lithium or cesium.[23] The synthesis of alkali metal stannaborate salts is achieved by modifications to the original synthetic procedure reported by Chapman *et al*.[20] It should also be noted that anhydrous $SnCl_2$ must be used as insertion reactions since hydrated $SnCl_2 \cdot 2H_2O$ was attempted but did not result in the insertion of a Sn atom into the borane cage.

Furthermore, aqueous bases such as hydroxides cannot be used for the same reason in the initial anion synthesis. In contrast, the synthesis of $B_{11}H_{11}Pb^{2-}$ salts utilise aqueous bases due to two main factors: the maintained activity of the aqueous $PbCl_2$ reagent, and the avoidance of highly toxic butyl lead when nBuLi is reacted with Pb compounds.

The $B_{11}H_{11}Sn^{2-}$ anion was successfully synthesised and confirmed by ^{11}B NMR spectroscopy (see Figure 4.2a). It shows three characteristic resonances at -5.3 (B1), -11.1 (B2-B6) and -12.4 (B7-B11) ppm with an intensity ratio 1:5:5, which correlates to the three different boron environments within the anion structure (B1, B2-B6, B7-B11 in Figure 4.1). Interestingly, there are shoulders on the resonance seen at -11.1 ppm. These arise from the coupling of the boron atoms to the tin atom, which has a low abundance (7.7 %) NMR active ($I = ½$) isotope that causes peak splitting of the singlet.[34] The interaction between the Sn and adjacent B's creates a triplet arising from the spin active ($I = ½$) and inactive ($I = 0$) tin nuclei, respectively, which was also seen in the NMR spectrum of $B_{11}H_{11}Pb^{2-}$.[19] The ^{1}H {^{11}B} NMR spectra shows 3 major resonances (2.98, 1.60 and 0.82 ppm) alongside two solvent signals at 2.8 and 1.9 ppm corresponding to acetonitrile and water.[35] There is a small $B_{11}H_{11}^{2-}$ impurity ($\sim$ 2.5% based on [11]B integration) arising from premature closing of the boron-cage after deprotonation, but before Sn insertion. This is not believed to have a major impact on the bulk ion conductivity or thermal characteristics. The sodium and potassium salts show the same NMR spectra as they weren't synthesised from the lithium analogue using cation exchange.
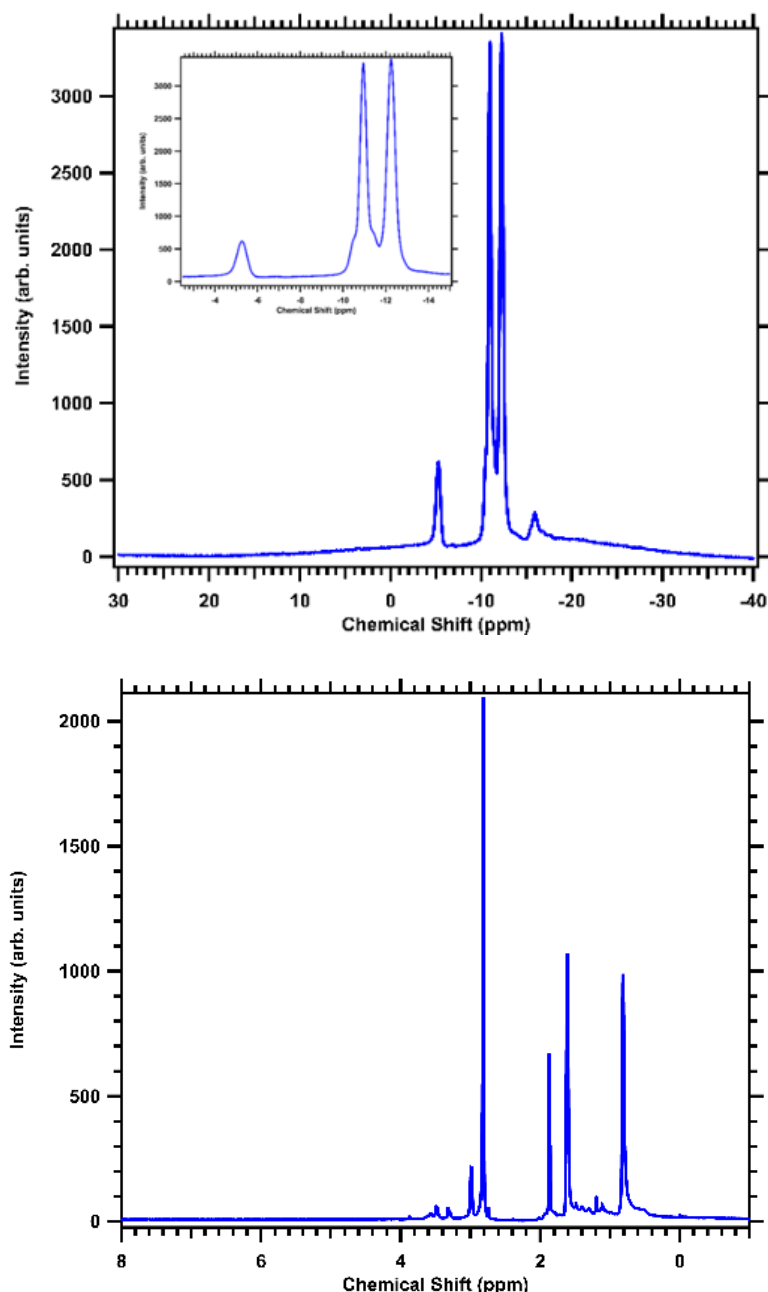
Figure 4.2a. ^{11}B {^{1}H} NMR spectrum of $Li_2B_{11}H_{11}Sn$ in CD_3CN: -5.3 (s, 1B, B1), -11.1 (s, 5B, B7-B11), -12.4 (s, 5B, B2-B6). **Figure 4.2b**. ^{1}H {^{11}B} NMR spectrum of $Li_2B_{11}H_{11}Sn$ in CD_3CN: 2.98 (s, 1H), 1.60 (s, 5H), 0.82 (s, 5H).

The lithium stannaborate salt was analysed using Raman spectroscopy (Figure 4.3) under an inert argon atmosphere in a sealed capillary. The spectrum contains a strong signal at $\sim$ 2450 cm^{-1} that corresponds to a B-H stretch within the $B_{11}H_{11}Sn^{2-}$ cage. There are 3 other major signals in the spectrum at 750, 570, and 280 cm^{-1}. These correspond to vibrational modes connected to the stretching modes of the stannaborate cage. The signals at 750 and 570 cm^{-1} correspond to similar modes seen the in mono-carborane anion ($CB_{11}H_{12}^{-}$) due to the

stretching and deformation of a boron cage. The very strong peak at 280 cm^{-1} is not seen in the case of the carborane, owing to the signal corresponding to the stretch of the B-Sn bond, which is consistent with the computational pattern in Figure 4.3. The low frequency of the stretch is due to the high mass of the Sn atom in comparison to a boron or carbon atom. The Raman spectrum for the lithium stannaborate salt also correlates well with one previously reported for cesium stannaborate.[23] Thus, the Raman and NMR data show that the B$_{11}$H$_{11}$Sn^{2-} anion has been successfully synthesised.
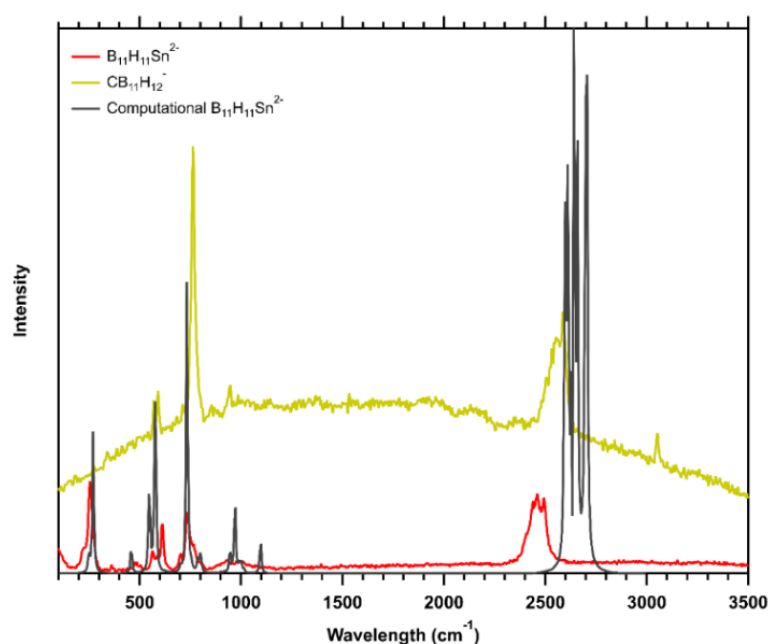
Figure 4.3. Experimental Raman spectroscopy of Li$_2$B$_{11}$H$_{11}$Sn and Zn(CB$_{11}$H$_{12}$)$_2$ performed in an inert argon atmosphere compared with a computational spectrum of B$_{11}$H$_{11}$Sn^{2-}.

Figure 4.4 shows the DSC analysis of the lithium, sodium, and potassium stannaborate salts. All samples show a distinct endothermic peak at different temperatures, which could be synonymous with a variety of different structural and chemical processes. Li$_2$B$_{11}$H$_{11}$Sn shows this endothermic event at 340 °C with Na$_2$B$_{11}$H$_{11}$Sn at 180 °C and K$_2$B$_{11}$H$_{11}$Sn at 250 °C, respectively.
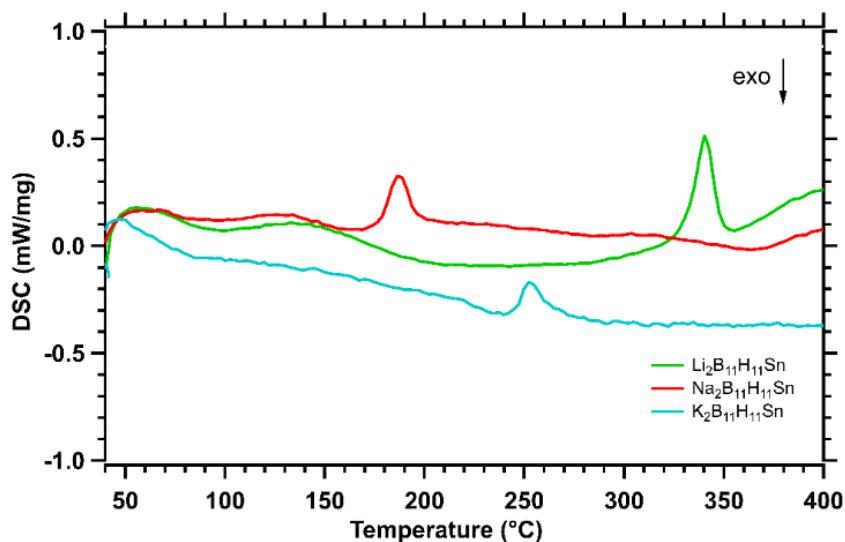
Figure 4.4. DSC analysis of alkali metal $B_{11}H_{11}Sn^{2-}$ salts in an argon atmosphere at 5 °C min^{-1}.

In-situ SR-XRD was performed on the stannaborates in an attempt to understand the endothermic events observed during DSC analysis with the data illustrated in Figure 4.5 and Figures B2-B6. The data for the $Li_2B_{11}H_{11}Sn$ sample (Figure 4.5a) illustrates that pattern at 30 °C contains at least two crystallographic phases. One of these phases is LiCl, an impurity, which persists throughout heating and cooling of the material. One phase decomposes at ~ 65 °C and is likely attributed to a dehydration step, where hydration of the sample occurred during exposure to air when sealing the capillary due to the fact that no characteristic water signals are seen in the Raman spectrum. It should be noted that none of the observed phases match the known $[Li(thf)_3]_2[SnB_{11}H_{11}]$ crystal structure, indicating again that the lithium stannaborate is likely hydrated, rather than solvated by tetrahydrofuran, as shown by NMR.[23] Another major phase exists that undergoes an increase of crystallographic symmetry at 130 °C, possibly due to the full or partial dehydration of the material. Indexing of the diffraction pattern determined a tetragonal space group ($P4_2/ncm$) with lattice parameters of $a = b =$ 9.8923(4) Å and c = 10.4149(3) Å. This phase is present until ~ 330 °C when decomposition occurs forming an amorphous phase which is apparent through a halo around 2θ = 6°, which is also seen after the decomposition of similar compounds such as $Li_2B_{11}H_{11}Pb$.[19] These observations are corroborated in the DSC data (Figure 4.4), where endothermic events occur at peak temperatures of 60, 130, and 340 °C, respectively. After decomposition, the crystallisation of Sn metal is seen.

Na$_2$B$_{11}$H$_{11}$Sn and K$_2$B$_{11}$H$_{11}$Sn also show their respective metal chloride (NaCl and KCl) impurities, which persist throughout the heating process (Figure 4.5b and 4.5c). The room temperature phase of K$_2$B$_{11}$H$_{11}$Sn has been indexed to exist in an orthorhombic space group with a = 11.7216(3), b = 8.1006(1), and c = 12.0948(3) Å, although the crystal structure could not explicitly be solved. The room temperature data for Na$_2$B$_{11}$H$_{11}$Sn could not be indexed due to the poor crystallinity of the sample. Upon heating, these compounds behave differently to the lithium analogue. They have a reversible polymorphic phase change at 200 °C and 250 °C, respectively, which explains the endothermic peaks seen in DSC (Figure 4.4). These high temperature phase changes for Na$_2$B$_{11}$H$_{11}$Sn and K$_2$B$_{11}$H$_{11}$Sn occur at higher temperatures than seen in the lithium and sodium 12-vertex carborane.[36] High temperature polymorphic phase transitions can be favourable in enhancing the ion conductivity of a material, as seen in this class of boron-based compounds.[37] However, this is an improvement on B$_{11}$H$_{11}$Pb^{2-} salts due to the fact there are no polymorphic phase transitions before decomposition. The high temperature phase changes are also coupled by the appearance of a halo at 2θ = 4.2° and indicates the formation of an amorphous phase, which is different to the decomposition halo seen in Li$_2$B$_{11}$H$_{11}$Sn, which is seen at 2θ = 6.2°. This is also seen as a decomposition product, such as Li$_2$B$_{12}$H$_{12}$.[38] Upon cooling, both the Na$_2$B$_{11}$H$_{11}$Sn and K$_2$B$_{11}$H$_{11}$Sn materials return to their low temperature phases as the decomposition temperature of these materials were not attained.
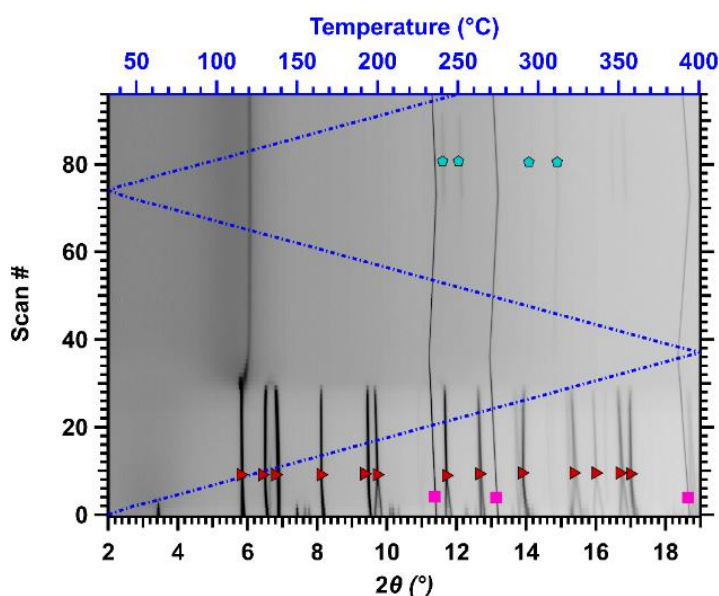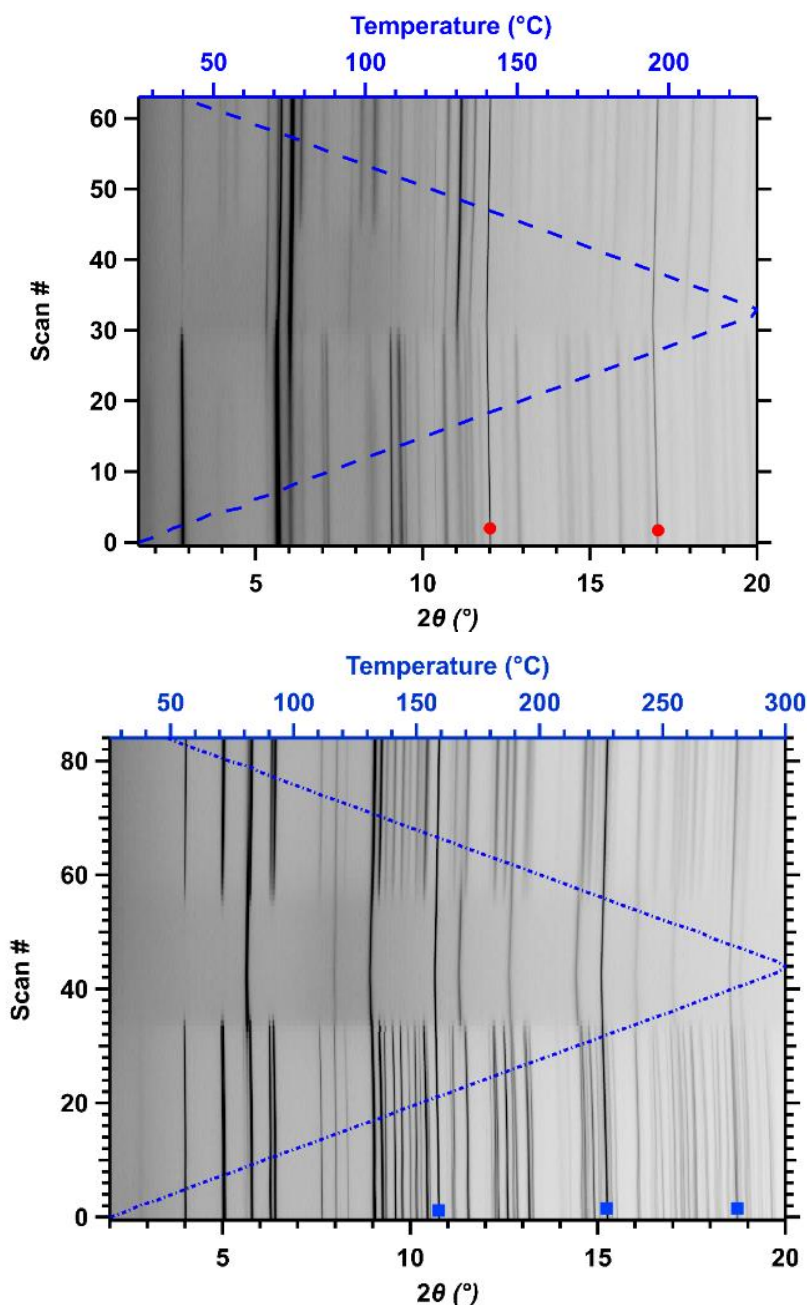
Figure 4.5a. *In-situ* XRD spectrum of $Li_2B_{11}H_{11}Sn$ heated at 5 °C min^{-1} and λ = 0.59096(1) Å. Pink square – LiCl, Blue pentagon – Sn metal. Blue dashed line signifies temperature for a specific scan.

Figure 4.5b. *In-situ* XRD spectrum of $Na_2B_{11}H_{11}Sn$ heated at 5 °C min^{-1} and λ = 0.59096(1) Å. Red circle – NaCl. **Figure 4.5c.** *In-situ* XRD spectrum of $K_2B_{11}H_{11}Sn$ heated at 5 °C min^{-1} and λ = 0.59096(1) Å. Blue square – KCl.

The stannaborate salts were analysed by EIS to assess their ion conductivity as a function of temperature and determine their suitability as solid-state ion conductors (Figure 4.6). All of the materials show low, but measurable ion conductivity at room temperature but improve greatly on heating. $Li_2B_{11}H_{11}Sn$ shows promise as it reaches superionic conductivity (> 1 x 10$^-$

^{3} S cm^{-1}) above 110 °C. The ion conductivity reaches a maximum of 8 x 10^{-3} S cm^{-1} at 130 °C, however, the ion conductivity decreases at higher temperature, which corresponds with an event seen in the *in-situ* XRD, attributed to desolvation (Figure 4.5a). Desolvation is known to have an effect on the ion conductivity of solid-state ion conductors.[14] Thus, the ion conductivity for Li$_2$B$_{11}$H$_{11}$Sn is lower than Li$_2$B$_{11}$H$_{11}$Pb (2 x 10^{-2} S cm^{-1} at 120 °C)[19] and LiCB$_{11}$H$_{12}$ (2 x 10^{-1} at 150 °C)[11], but does show a higher ion conductivity than the unsubstituted Li$_2$B$_{12}$H$_{12}$ above 110 °C. Na$_2$B$_{11}$H$_{11}$Sn shows promise reaching 1 x 10^{-3} S cm^{-1} at 170 °C, which is a large improvement in comparison to its contemporaries Na$_2$B$_{11}$H$_{11}$Pb (1 x 10^{-5} S cm^{-1} at 170 °C)[19] and the unsubstituted Na$_2$B$_{12}$H$_{12}$ (1 x 10^{-4} S cm^{-1} at 170 °C)[39]. K$_2$B$_{11}$H$_{11}$Sn shows low ion conductivity of 1 x 10^{-6} S cm^{-1} at 100 °C, much lower than KB$_{11}$H$_{14}$ (1 × 10^{-4} S cm^{-1} at 150 °C) and slightly better than to KB$_3$H$_8$ (2 x 10^{-7} S cm^{-1} at 150 °C).[12,40] The ion conductivity results for the stannaborates in comparison to other borate salts demonstrate that superionic conductivities are obtainable, but it is still difficult to predict which borate salts will present superionic conductivity at (or near) room temperature. High ion conductivity is most often linked to rapid reorientational dynamics, but also structural considerations, including anion size, anion electrostatic polarity, cation size, and structure-type.[28,37,41] Therefore, the search for a room temperature superionically conducting salt still requires further experimental and theoretical studies to determine the optimum chemical compositions and structures.
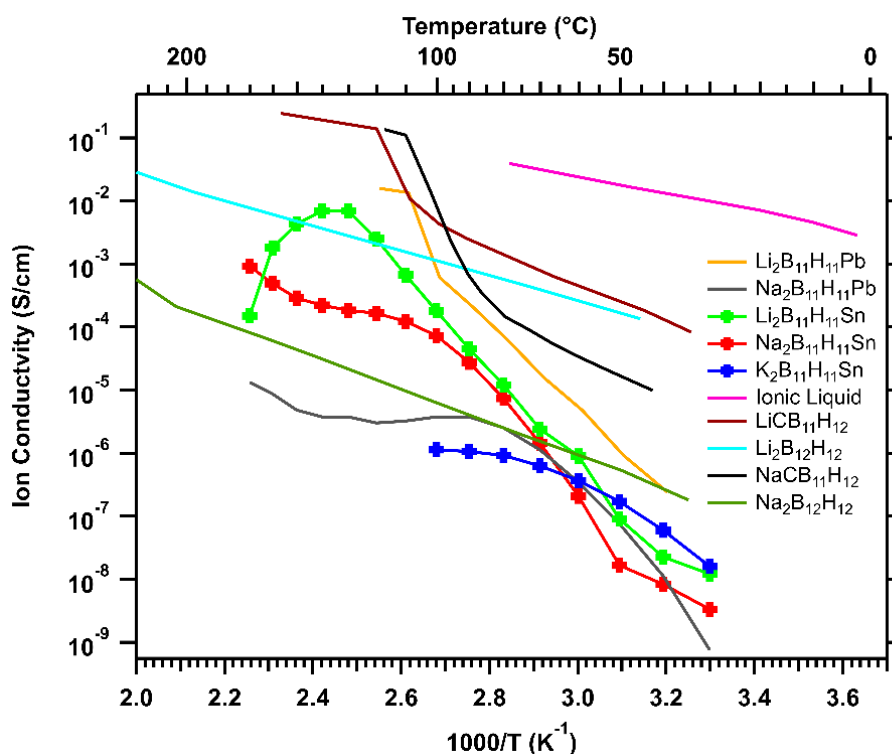
Figure 4.6. Ion conductivity of stannaborates and comparable salts from literature.[11,19,37,42]

Linear sweep voltammetry (LSV) was performed on $Li_2B_{11}H_{11}Sn$ to assess the oxidative stability of the material, which shows the electrochemical limit where the compound is irreversibly oxidised. Thus, this shows the working range of these materials as a possible solid-state electrolyte. $Li_2B_{11}H_{11}Sn$ shows immediate, irreversible oxidation from the open circuit voltage of 2.3 V vs Li^+/Li (Figure 4.7). This value is compared to other borate salts such as $LiBH_4$ (2.2 V), $Li_2B_{11}H_{11}Pb$ (2.3 V), and $LiB_{11}H_{14}\cdot xH_2O$ (2.9 V).[12,19,29] The oxidation event in Figure 4.7 is only observable in the first LSV scan, showing that it only occurs on the first voltage cycle as the electrolyte is already oxidised.
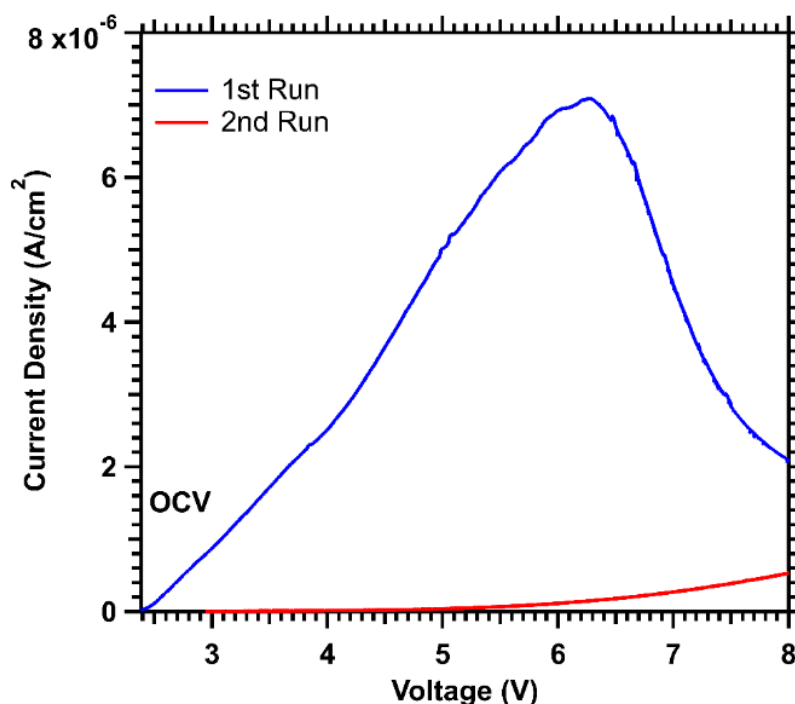
Figure 4.7. Linear Sweep Voltammetry chart of $Li_2B_{11}H_{11}Sn$ at 60 °C with a scan rate of 50 μV s^{-1} from the open circuit voltage (2.3 V) to 8 V.

4.5 Conclusions

A series of group 1 metal stanna-*closo*-dodecaborate salts were successfully synthesised from trimethylammonium *nido*-undecaborate. This was confirmed using ^{11}B and ^{1}H NMR along with computational and experimental Raman spectroscopy. Additional characterisation of these compounds included SR-XRD and DSC, which showed polymorphic phase changes in $Na_2B_{11}H_{11}Sn$ and $K_2B_{11}H_{11}Sn$ at 200 and 250 °C, respectively, and a decomposition event at 340 °C for $Li_2B_{11}H_{11}Sn$. The compounds showed crystalline structures and a high temperature polymorph of $K_2B_{11}H_{11}Sn$ could be indexed having an orthorhombic space group however, the full crystal structure of these compounds could not be determined. $Li_2B_{11}H_{11}Sn$ showed excellent ion conductivity above 1 mS cm^{-1} between 110 and 130 °C, however, the conductivity reduces at higher temperatures and correlates with a polymorphic phase change (increase in symmetry) seen in the *in-situ* SR-XRD diffraction pattern. $Na_2B_{11}H_{11}Sn$ also shows superionic conductivity at 170 °C and has higher conductivity than the lead analogue, however, once more, lower than $NaCB_{11}H_{12}$. It is thought that the ion conductivity of these compounds is lower than the carborane due to divalent nature of these salts. One way to

improve the conductivity could be to introduce elements into the cage resulting in a monovalent anion.

4.6 References

1   Y. Nishi, *J. Power Sources*, 2001, **100**, 101–106.

2   P. G. Balakrishnan, R. Ramesh and T. Prem Kumar, *J. Power Sources*, 2006, **155**, 401–414.

3   O. Crowther and A. C. West, *J. Electrochem. Soc.*, 2008, **155**, A806.

4   J. G. Kim, B. Son, S. Mukherjee, N. Schuppert, A. Bates, O. Kwon, M. J. Choi, H. Y. Chung and S. Park, *J. Power Sources*, 2015, **282**, 299–322.

5   A. Hooper, *J. Electroanal. Chem.*, 1980, **109**, 161–166.

6   L. Schweiger, K. Hogrefe, B. Gadermaier, J. L. M. Rupp and H. M. R. Wilkening, *J. Am. Chem. Soc.*, 2022, **144**, 9597–9609.

7   F. Han, Y. Zhu, X. He, Y. Mo and C. Wang, *Adv. Energy Mater.*, 2016, **6**, 1–9.

8   Q. Zhang, D. Cao, Y. Ma, A. Natan, P. Aurora and H. Zhu, *Adv. Mater.*, 2019, **31**, 1–42.

9   L. Yue, J. Ma, J. Zhang, J. Zhao, S. Dong, Z. Liu, G. Cui and L. Chen, *Energy Storage Mater.*, 2016, **5**, 139–164.

10   F. Cuevas, M. B. Amdisen, M. Baricco, C. E. Buckley, Y. W. Cho, P. De Jongh, L. M. De Kort, J. B. Grinderslev, V. Gulino, B. C. Hauback, M. Heere, T. Humphries, T. R. Jensen, S. Kim, K. Kisu, Y. S. Lee, H. W. Li, R. Mohtadi, K. T. Møller, P. Ngene, D. Noréus, S. I. Orimo, M. Paskevicius, M. Polanski, S. Sartori, L. N. Skov, M. H. Sørby, B. C. Wood, V. A. Yartys, M. Zhu and M. Latroche, *Prog. Energy*, 2022, **4**, 032001.

11   W. S. Tang, A. Unemoto, W. Zhou, V. Stavila, M. Matsuo, H. Wu, S. I. Orimo and T. J. Udovic, *Energy Environ. Sci.*, 2015, **8**, 3637–3645.

12   D. H. P. Souza, K. T. Møller, S. A. Moggach, T. D. Humphries, A. M. D'Angelo, C. E. Buckley and M. Paskevicius, *J. Mater. Chem. A*, 2021, **9**, 15027–15037.

13   D. H. P. Souza, A. M. D'Angelo, C. E. Buckley, M. Paskevicius and T. D. Humphries, *Dalt. Trans.*, 2022, **51**, 13848–13857.

14   D. H. P. Souza, T. D. Humphries, Y. Liu, A. Gradišek, A. M. D'Angelo, C. E. Buckley and M. Paskevicius, *Sustain. Energy Fuels*, 2022, **6**, 4614–4625.

15   A. Berger, A. Ibrahim, C. E. Buckley and M. Paskevicius, *Phys. Chem. Chem. Phys.*, 2023, **25**, 5758–5775.

16   M. Dimitrievska, H. Wu, V. Stavila, O. A. Babanova, R. V. Skoryunov, A. V. Soloninin, W. Zhou, B. A. Trump, M. S. Andersson, A. V. Skripov and T. J. Udovic, *J. Phys. Chem. C*, 2020, **124**, 17992–18002.

17   K. Sau, T. Ikeshoji, S. Kim, S. Takagi and S. Orimo, *Chem. Mater.*, 2021, **33**, 2357–2369.

18   M. Paskevicius, B. R. S. Hansen, M. Jørgensen, B. Richter and T. R. Jensen, *Nat. Commun.*, 2017, **8**, 10–15.

19   T. A. Hales, K. T. Møller, T. D. Humphries, A. M. D'Angelo, C. E. Buckley and M. Paskevicius, *J. Phys. Chem. C*, 2023, **127**, 949–957.

20   R. W. Chapman, J. G. Kester, K. Folting, W. E. Streib and L. J. Todd, *Inorg. Chem.*, 1992, **31**, 979–983.

21   L. Wesemann, T. Marx, U. Englert and M. Ruck, *Eur. J. Inorg. Chem.*, 1999, 1563–1566.

22   T. Gädt, B. Grau, K. Eichele, I. Pantenburg and L. Wesemann, *Eur. J.*, 2006, 1036–1045.

23   T. Gädt and L. Wesemann, *Zeitschrift fur Anorg. und Allg. Chemie*, 2007, **633**, 693–699.

24   W. R. Wadt and P. J. Hay, *J. Chem. Phys.*, 1985, **82**, 284–298.

25   P. J. Hay and W. R. Wadt, *J. Chem. Phys.*, 1985, **82**, 270–283.

26   P. J. Hay and W. R. Wadt, *J. Chem. Phys.*, 1985, **82**, 299–310.

27   M. J. Frisch, G. W. Trucks, H. B. Schlegel, G. E. Scuseria, M. A. Robb, J. R. Cheeseman, G. Scalmani, V. Barone, G. A. Petersson, H. Nakatsuji, X. Li, M. Caricato, A. V. Marenich, J. Bloino, B. G. Janesko, R. Gomperts, B. Mennucci, H. P. Hratchian, J. V. Ortiz, A. F. Izmaylov, J. L. Sonnenberg, Williams, F. Ding, F. Lipparini, F. Egidi, J. Goings, B. Peng, A. Petrone, T. Henderson, D. Ranasinghe, V. G. Zakrzewski, J. Gao, N. Rega, G. Zheng, W. Liang, M. Hada, M. Ehara, K. Toyota, R. Fukuda, J. Hasegawa, M.

Ishida, T. Nakajima, Y. Honda, O. Kitao, H. Nakai, T. Vreven, K. Throssell, J. A. Montgomery Jr., J. E. Peralta, F. Ogliaro, M. J. Bearpark, J. J. Heyd, E. N. Brothers, K. N. Kudin, V. N. Staroverov, T. A. Keith, R. Kobayashi, J. Normand, K. Raghavachari, A. P. Rendell, J. C. Burant, S. S. Iyengar, J. Tomasi, M. Cossi, J. M. Millam, M. Klene, C. Adamo, R. Cammi, J. W. Ochterski, R. L. Martin, K. Morokuma, O. Farkas, J. B. Foresman and D. J. Fox, *Gaussian 09, Revis. A. 02*, 2009.

28   B. R. S. Hansen, M. Paskevicius, M. Jørgensen and T. R. Jensen, *Chem. Mater.*, 2017, **29**, 3423–3430.

29   R. Asakura, L. Duchêne, R. S. Kühnel, A. Remhof, H. Hagemann and C. Battaglia, *ACS Appl. Energy Mater.*, 2019, **2**, 6924–6930.

30   I. K. Suh, H. Ohta and Y. Waseda, *J. Mater. Sci.*, 1988, **23**, 757–760.

31   G. B. Dunks, K. Barker, E. Hedaya, C. Hefner, K. Palmer-Ordonez and P. Remec, *Inorg. Chem.*, 1981, **20**, 1692–1697.

32   Z. Zhang and L. F. Nazar, *Nat. Rev. Mater.*, 2022, **7**, 389–405.

33   A. Berger, C. E. Buckley and M. Paskevicius, *Inorg. Chem.*, 2021, **60**, 14744–14751.

34   E. Scientific, P. Company, C. Devillers, T. Lecomte and R. Hagemann, 1983, **50**, 205–217.

35   G. R. Fulmer, A. J. M. Miller, N. H. Sherden, H. E. Gottlieb, A. Nudelman, B. M. Stoltz, J. E. Bercaw, K. I. Goldberg, R. Gan and H. Apiezon, *Organometallics*, 2010, **29**, 2176–2179.

36   T. J. Udovic, M. Matsuo, W. S. Tang, H. Wu, V. Stavila, A. V. Soloninin, R. V. Skoryunov, O. A. Babanova, A. V. Skripov, J. J. Rush, A. Unemoto, H. Takamura and S. I. Orimo, *Adv. Mater.*, 2014, **26**, 7622–7626.

37   B. R. S. Hansen, M. Paskevicius, H. W. Li, E. Akiba and T. R. Jensen, *Coord. Chem. Rev.*, 2016, **323**, 60–70.

38   M. P. Pitt, M. Paskevicius, D. H. Brown, D. A. Sheppard and C. E. Buckley, *J. Am. Chem. Soc.*, 2013, **135**, 6930–6941.

39   T. J. Udovic, M. Matsuo, A. Unemoto, N. Verdal, V. Stavila, A. V. Skripov, J. J. Rush, H. Takamura and S. I. Orimo, *Chem. Commun.*, 2014, **50**, 3750–3752.

40   J. B. Grinderslev, K. T. Møller, Y. Yan, X. M. Chen, Y. Li, H. W. Li, W. Zhou, J. Skibsted, X. Chen and T. R. Jensen, *Dalt. Trans.*, 2019, **48**, 8872–8881.

41   M. Jørgensen, P. T. Shea, A. W. Tomich, J. B. Varley, M. Bercx, S. Lovera, R. Černý, W. Zhou, T. J. Udovic, V. Lavallo, T. R. Jensen, B. C. Wood and V. Stavila, *Chem. Mater.*, 2020, **32**, 1475–1487.

42   Y. Sadikin, M. Brighi, P. Schouwink and R. Černý, *Adv. Energy Mater.*, 2015, **5**, 1501016.

Chapter 5

Monovalent heavy metal substituted closo-dodecaborate ($B_{11}H_{11}M^{-}$) (M = Sb, Bi) salts as potential solid-state ion conductors

Thomas A. Hales, Terry D. Humphries, Craig E. Buckley, Mark Paskevicius

CHAPTER 5 - MONOVALENT HEAVY METAL SUBSTITUTED *CLOSO*-DODECABORATE ($B_{11}H_{11}M^-$) (*M* = Sb, Bi) SALTS AS POTENTIAL SOLID-STATE ION CONDUCTORS

5.1 Abstract

Closo-dodecaborate salts with a group 1 cation have been shown to have impressive performance as solid-state electrolytes for future battery applications. Group 1 stiba- and bisma-*closo*-borate salts were synthesised from sodium *nido*-undecaborate as confirmed with ^{11}B NMR and Raman spectroscopies. The resulting monovalent anions exhibit polar electronegativity akin to the best performing borohydride cluster salts, $LiCB_{11}H_{12}$ and $NaCB_{11}H_{12}$. $NaB_{11}H_{11}Bi$ and $NaB_{11}H_{11}Sb$ show superionic conductivity above 140 and 90 °C up to maximum of 2 x 10^{-3} S cm⁻¹ at 170 °C and 1 x 10^{-2} S cm⁻¹ at 150 °C, respectively. This performance is better than the lithium salts, which not only show low ion conductivity ≤ 10^{-8} S cm⁻¹ but do not reach superionic conductivity even at elevated temperature. The ionic conductivity results reveal that monovalent alkali salts with weakly-coordinating anions continue to show promise for future battery applications, opening up an array of alternative chemistries for solid-state ionic conductors to be explored.

5.2 Introduction

Energy storage systems are crucial to future energy technologies due to the increased usage of intermittent, renewable energy sources such as wind and solar.[1] As a result, increased focus into battery technologies is paramount to effectively store the required energy to power the world. One of the most common contemporary batteries is the Li-ion battery, comprising of a Li-doped graphite anode, a lithium transition metal oxide cathode (e.g. $LiMnO_2$) and

dissolved electrolyte (e.g. LiPF$_6$) in a flammable and volatile solvent (e.g. ethylene carbonate).[2,3] The liquid nature of the battery cell results in certain compromises including the requirement for a graphite anode and a solvent that limits the operating temperature limit and increases the risk of fire.[4] One way to avoid this issue is to use a full solid-state cell construction using a solid-state electrolyte.[5]

Solid-state electrolytes work in the same way to their liquid alternatives, where instead of a cation travelling through the liquid medium between the relative electrodes, it can instead diffuse through an anionic lattice.[6,7] A variety of different materials have been investigated for use as solid-state electrolytes, for example, ceramics, polymers and ionic salts. Some have shown particular promise, such as the ceramic (Li$_{10}$GeP$_2$S$_{12}$) and the polymer (PAN - Li$_{0.33}$La$_{0.55}$TiO$_3$) showing high ion conductivities.[8–10] However, other properties are also desired including mechanical flexibility, electrochemical stability, low cost, and ease of manufacture. Recently, complex alkali metal borohydride salts have also shown promise with high ion conductivities at or near room temperature (e.g. LiB$_{11}$H$_{14}$).[11,12] Both Li- and Na$_2$B$_{12}$H$_{12}$ have been investigated as ionic conductors, which show step-function jumps in ionic conductivity above temperatures when a structural phase change occurs, resulting in enhanced anionic dynamics.[13,14] Reducing the symmetry of the anion tends to improve the cationic conductivity, as seen by the ion conductivity of the decahydro-*closo*-decaborate (B$_{10}$H$_{10}$$^{2-}$), and more dramatically, the 12-vertex mono-carborane (CB$_{11}$H$_{12}$$^-$). LiCB$_{11}H_{12}$ shows a considerably higher ionic conductivity, 5 x 10^{-1} S cm^{-1} at 160 °C against the symmetric Li$_2$B$_{12}$H$_{12}$, 2 x 10^{-4} S cm^{-1} at 180 °C.[15–17] Introducing a carbon atom favourably changes the valency of the B$_{12}$H$_{12}$$^{2-}$ anion from divalent to monovalent, which causes the anion to be more weakly coordinating to the cation. The loss of anionic symmetry also affects the anion dynamics in the structure to be more polar, allowing for lower activation energies for cation migration.[18,19] It has been reported that the lowering of activation energy may be due to cations migrating through an anionic lattice with a "paddle wheel" mechanism.[20–22]

The mono-carborane (CB$_{11}$H$_{12}$$^-$) has recently been synthesised to provide a low-cost chemical pathway to a polar weakly-coordinating anionic salt.[23] More recently, other substitutions to the *closo*-borate anion have been explored with group 14 elements such as tin (Sn) and lead (Pb) being substituted as opposed to carbon (C).[24,25] These compounds were synthesised by heavy metal atomic insertion into a B$_{11}$H$_{14}$$^-$ precursor, but unlike CB$_{11}$H$_{12}$$^-$, the stanna-

($B_{11}H_{11}Sn^{2-}$) and plumba-*closo*-borates ($B_{11}H_{11}Pb^{2-}$) were divalent due to the lack of a metal-hydrogen group akin to the C–H group in the carborane. Both substituted borates demonstrated excellent ionic conductivity: $Li_2B_{11}H_{11}Pb$ was 7 x 10^{-3} S cm^{-1} at 120 °C and $Li_2B_{11}H_{11}Sn$ was 8 x 10^{-3} S cm^{-1} at 130 °C, but both were lower than the carborane at equivalent temperatures.[24] The lower ionic conductivity in the metallo-*closo*-borates may be related to their divalence, causing stronger cation-anion coordination, but may also be related to the fact that the mono-carborane undergoes a polymorphic phase transition to a more dynamic structure, which improves the ion conductivity.[26]

As a result, the aim of this research is to synthesise and characterise monovalent metal substituted 12-vertex borate salts and investigate their solid-state ion conductivity. In order to synthesise a monovalent anion, group 15 elements (Sb or Bi) were introduced into the anion cage. The ability for group 15 elements to reach a higher oxidation number, +5, in comparison to +4 for group 14 elements, allowed the overall charge of the anions to be −1 rather than −2. All of the substituted heavy metals are not protonated, unlike the B in unsubstituted $B_{12}H_{12}^{2-}$ and C in the $CB_{11}H_{12}^-$ anion, hence the need for a higher oxidation number to reach the desired valence.

5.3 Experimental

Computational calculations were performed using Density Functional Theory (DFT) using the B3LYP hybrid functional with a LanL2MB basis set, to compute the large Sb and Bi atoms. The computations were performed using the Gaussian G09W software, optimising geometry and anion energy. This was used to calculate computational Raman spectra for the respective anions. Electrostatic Potential (ESP) surfaces were mapped at an isovalue of 0.008 electrons/bohr^3 (5.40 x 10^{28} electrons/m^3).

Nuclear Magnetic Resonance (NMR) spectroscopy was performed using a Bruker AVANCE III 400 MHz spectrometer (128.4 MHz for [11]B) with chemical shifts referenced to BF_3·OEt_2 and tetramethylsilane (TMS), respectively, using a CD_3CN solvent (Sigma-Aldrich, 99.8% D).

Differential scanning calorimetry – Thermogravimetric analysis (DSC-TGA) was performed using a Netzsch STA 449 F3 Jupiter. The materials ($\sim$ 5 mg) were sealed in an aluminium crucible with a pinhole pierced in the lid and heated from 40 – 350 °C (10 °C min^{-1}) under an argon flow of 40 mL min^{-1}. The sensitivity and temperature of the DSC was calibrated using In, Zn, Sn, Bi and CsCl reference materials, resulting in a temperature accuracy of ± 0.2 °C. Residual Gas Analysis was performed on the gases released during the DSC-TGA heating using a quadrupole mass spectrometer (RGA-300, Stanford Research Systems) operating under high vacuum ($\sim$ 1 x 10^{-3} mbar) through a bleed of the DSC-TGA flow gas.

Electrochemical Impedance Spectroscopy (EIS) was measured using a ZIVE SP1 instrument. The materials were pressed into pellets, with a diameter of 6 mm and thickness of $\sim$ 1 mm, by applying a pressure of 1000 kg in an inert argon atmosphere. A pellet was placed between 2 gold wafers (0.1 mm thickness) and loaded into a sealed Teflon Swagelok-type cell with stainless steel electrodes under argon and data were collected using 50 mV AC from 1 MHz to 10 Hz. The temperature of the cells was kept isothermal at each temperature and monitored using a K-type thermocouple. To calculate the ion conductivity (σ) from the data, the x-intercept (R_{real}) of the resulting Nyquist plot was determined using a known method.[27]

Powder X-ray diffraction (XRD) characterisation was performed using a Bruker D8 Advance diffractometer equipped with a copper X-ray source Cu K$_{\alpha 1}$ radiation, λ = 1.540593 Å, Cu K$_{\alpha 2}$ radiation, λ = 1.544414 Å and a Lynxeye PSD detector in Bragg-Brentano geometry. Data were collected in the 2θ range from 5° to 80° with a step size of 0.02°. Powder samples were prepared into a flat-plate in an argon filled glovebox and the packed material was covered with a MYLAR® film and sealed with grease to prevent contact with air and moisture.

Raman Spectroscopy was performed using a WITec Alpha 300 SAR confocal Raman microscope with 600 grating mm^{-1} and a 532 nm green light excitation wavelength. Samples were prepared in an argon filled glovebox to prevent contamination with moisture or air and sealed in 1 mm borosilicate capillaries. Raman spectra were collected using 100 accumulations with an integration time of 400 ms. Data processing was performed including background subtraction using Project 4 (WITec) software.

Energy dispersive X-Ray Spectroscopy (EDS) was performed using a Zeiss Neon 40EsB scanning electron microscope. Powder samples were loaded on carbon tape mounted on an aluminium

stub. Samples were covered in a custom made air sealed container then placed inside the air free atmosphere SEM, preventing air exposure. The acceleration voltage used was 20 kV at a working distance of 7 mm and an aperture size of 60 mm. The data was analysed using the Aztec, version 5.1 software.

Lithium *closo*-dodecaborate tetrahydrate (>98%, Katchem), lithium hydroxide (98%, −4+14 mesh, anhydrous, Alfa Aesar), sodium hydroxide (anhydrous reagent grade, ≥98%, pellets, Sigma-Aldrich), *n*-butyllithium (2.5M in hexane, Sigma-Aldrich), tetrahydrofuran (≥99%, anhydrous, contains 250 ppm BHT as inhibitor, Sigma-Aldrich), acetone (Unilab) triethylamine (≥99.5%, Sigma-Aldrich), antimony (III) chloride (98%, Sigma-Aldrich), bismuth (III) chloride (≥98%, Sigma-Aldrich), and hydrochloric acid (37%, Fisher) were all used as purchased or diluted to desired concentrations using Milli-Q water. $(CH_3)_3NHB_{11}H_{14}$ was prepared using the method of Dunks *et al.* from sodium borohydride (98% (0.5% $MgCO_3$), Sigma-Aldrich) and 1-bromopentane (98%, Sigma-Aldrich) in diglyme (99.5%, anhydrous, Sigma-Aldrich).[28] The synthesis involves dissolving sodium borohydride in diglyme followed by the drop-wise addition of 1-bromopentane at 105 °C for 4h, and subsequent room temperature precipitation from water using trimethylamine hydrochloride (Me_3NHCl, 98%, Sigma-Aldrich). All samples were prepared and stored under an inert argon atmosphere using either Schlenk techniques or an mBraun glovebox (< 1 ppm H_2O & O_2).

5.3.1 Synthesis of $LiB_{11}H_{11}Bi$

$Me_3NHB_{11}H_{14}$ (0.75 g, 3.88 mmol) was dissolved in anhydrous tetrahydrofuran (THF) (30 mL) and cooled to 0 °C before *n*-butyllithium (6 mL) was added dropwise and the solution was stirred for 15 minutes under an inert Ar atmosphere. Bismuth (III) chloride (2.26 g, 7.17 mmol) dissolved in THF (15 mL) was added dropwise to the pale yellow solution at room temperature. The solution turned black instantaneously and was stirred for a further 15 minutes at room temperature before being refluxed for 4 hours at 65 °C. Water (4 mL) was added then the solvent was removed *in vacuo*. The residues were dissolved in water and the mixture filtered *in vacuo* and the resulting yellow liquid filtrate was dried *in vacuo*. The resultant solid was dried *in vacuo* at 150 °C leaving a pale yellow, highly hygroscopic solid,

which was stored under argon, $LiB_{11}H_{11}Bi$ (0.677 g, 1.96 mmol, 50 % yield). ^{11}B {^1H} NMR (128 MHz, CD_3CN) +11.5 ppm (s, 1B, B1), −6.4 ppm (m, 5B, B7−B11), −7.8 ppm (s, 5B, B2−B6)).

5.3.2 Synthesis of $NaB_{11}H_{11}Bi$

$LiB_{11}H_{11}Bi$ (0.282 g, 0.82 mmol) was dissolved in water (6 mL) and passed through a column containing Amberlite® IR 120 hydrogen form ion exchange resin (Sigma-Aldrich). The resulting acidic solution was treated with the sodium hydroxide until pH 7. The water was *removed in vacuo* at 150 °C leaving the desired product, $Na_2B_{11}H_{11}Bi$ (0.181 g, 61 % yield).

5.3.3 Synthesis of $MB_{11}H_{11}Sb$ (M = Li or Na)

$(Me_3)_3NHB_{11}H_{14}$ (0.821 g, 4.25 mmol) was dissolved in anhydrous THF (80 mL) and triethylamine (2.4 mL) was added before stirring for 15 minutes under an inert Ar atmosphere. Antimony (III) chloride (1.21 g, 5.3 mmol) dissolved in THF (15 mL) was added dropwise to the pale yellow solution at room temperature. The solution turned red instantaneously, then brown, and was stirred for a further 12 hours at room temperature. The solvent was removed *in vacuo* resulting in a brown oil. Lithium or sodium hydroxide (1 M, 20 mL) was added then the solution was heated to 80 °C for 2 hours whilst stirring and the resultant orange solid was filtered *in vacuo*. The filtrate was neutralised to pH 7 using HCl and a yellow solid formed. This was filtered *in vacuo* and the filtrate dried *in* vacuo. Acetone (20 mL) was added to the resulting solid and the insoluble LiCl by-product was filtered *in vacuo.* The filtrate was dried *in vacuo* at 80 °C for 5 hours leaving a pale yellow, highly hygroscopic solid, which was stored under argon, $LiB_{11}H_{11}Sb$ (0.174 g, 0.67 mmol, 16 % yield), $NaB_{11}H_{11}Sb$ (0.280 g, 1.02 mmol, 24 % yield). ^{11}B {^1H} NMR (128 MHz, CD_3CN) +9.7 ppm (s, 1B, B1), −8.6 ppm (m, 5B, B7−B11), −9.2 ppm (s, 5B, B2−B6).

5.4 Results and Discussion

Various substituted ($CB_{11}H_{12}^-$, $B_{11}H_{11}Pb^{2-}$, $B_{11}H_{11}Sn^{2-}$) 12-vertex *closo*-borate cages have previously been synthesised and their alkali metal salts have shown to have promise as solid-state electrolytes.[23–25] The polar nature of the anion is thought to be partially responsible for the structural reorientational dynamics observed at elevated temperatures. Computing the electropotential surfaces of $B_{11}H_{11}Bi^-$ and $B_{11}H_{11}Sb^-$ using DFT shows the charge profile within the anions are similar to the carborane, with the heteroatom (C–H, Sb, Bi) being more positive than the borane end of the anionic cage (Figure 5.1). The charge profiles of the divalent Pb and Sn substituted anions were more negatively charged and anisotropic.[24,29] As the carbon atom in the carborane is protonated, the overall length of the anions (H1 – CH, Sb or Bi) are similar, despite the much larger and more diffusely charged Sb and Bi atoms.
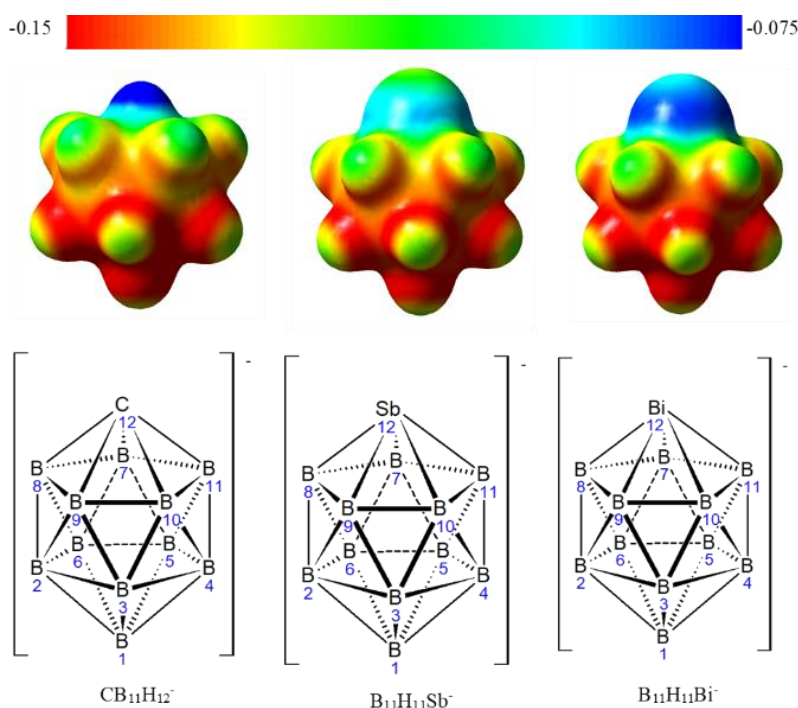
Figure 5.1. Electrostatic potential and structures without hydrogens of various anions using Density Functional Theory (DFT) and a B3LYP/LanM2MB basis set (Total Self-Consistent Field (SCF) Density (isovalue = 0.008)). NOTE: Hydrogen atoms are not shown for clarity, but the carbon atom in $CB_{11}H_{12}^-$ is protonated whereas the Bi and Sb atoms are not.

The synthesis of $B_{11}H_{11}Bi^-$ and $B_{11}H_{11}Sb^-$ salts follow the same basic pattern, $Me_3NHB_{11}H_{14}$ is reacted with a base (nBuLi for $B_{11}H_{11}Bi^-$ and Et_3N for $B_{11}H_{11}Sb^-$) in THF under an inert argon atmosphere. The resulting mixture is reacted with the respective metal (III) chloride and then worked up to form the respective alkali metal salt. These methods are adapted from that reported in the 1990 paper by Little *et al.*, modified in order to isolate the lithium and sodium salts.[30] These compounds were successfully synthesised as seen in the ^{11}B {^1H} NMR (Figure 5.2). The NMR spectra shows 3 district boron environments for both synthesised compounds in comparison to $B_{12}H_{12}{}^{2-}$. $B_{11}H_{11}Sb^-$ shows a distinct 1:5:5 ratio which correlates to the 3 boron environments clearly seen in the anionic structure (Figure 5.1). The first resonance at 9.7 ppm corresponds to the antipodal boron (B1) and the two other resonances at −8.6 and −9.2 ppm correspond to B7−B11 and B2−B6 respectively, as seen in previous research.[30] There are some minor impurities in the as-synthesised compounds, such as the starting material, $B_{11}H_{14}{}^-$, at -14.0, -15.6 and -16.9 ppm respectively.[31] The $B_{11}H_{11}Bi^-$ sample shows a spectrum with less impurities with only a minor $B_{11}H_{13}OH^-$ impurity (−14.1, −22.9, −11.0, −39.3, 18.0, −28.9 and −9.7 ppm respectively).[32] The spectrum also shows a 1:5:5 integration with some variation in peak intensity due to different broadness of the respective resonances.
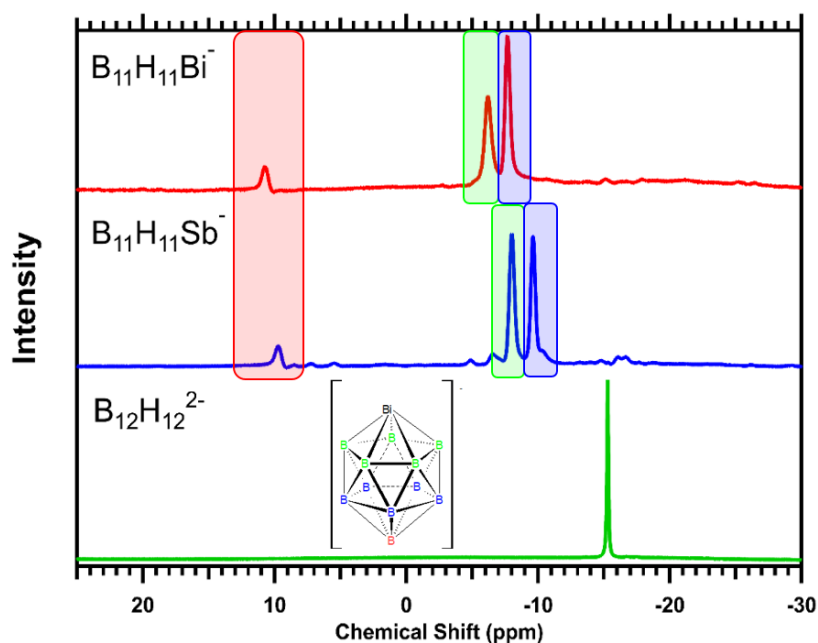
Figure 5.2. ^{11}B {^1H} NMR spectrum of $NaB_{11}H_{11}Bi$, $NaB_{11}H_{11}Sb$ and $Li_2B_{12}H_{12}$ in CD_3CN − $NaB_{11}H_{11}Bi$: 11.5 ppm (s, 1B, B1), −6.4 ppm (m, 5B, B7−B11), −7.8 ppm (s, 5B, B2−B6). $NaB_{11}H_{11}Sb$: +9.7 ppm (s, 1B, B1), −8.6 ppm (m, 5B, B7−B11), −9.2 ppm (s, 5B, B2−B6). $Li_2B_{12}H_{12}$: −15.5 ppm (s, 12B). The colour corresponds to the relevant boron atoms in the structure.

Raman spectroscopy was performed on powder samples under an inert atmosphere to further confirm the synthesis of the respective compounds (Figure 5.3). Both the antimony and bismuth salts show similar spectra due to their similar anionic structures. They show a low frequency peak at $\sim$ 240 cm^{-1}, which corresponds to the M−B stretch (M = Bi, Sb), confirmed using DFT, which is not seen in the experimental spectra of the mono-carborane as seen in Figure 5.3. This is at such low frequency due to the heavy metals involved in the bond. The additional B−C mode in the mono-carborane is at a similar frequency to the B−B modes so is difficult to differentiate. There are also 4 other main signals seen in the fingerprint region of the spectra at $\sim$ 450, 580, 710 cm^{-1}, which correspond to bond excitations within the anionic cage itself. Finally, the strong resonance at 2500 cm^{-1} corresponds to the B−H stretch. When these spectra are compared with the computationally generated spectra, they principally agree with each other, but as is typical, the spectra do show some wavenumber shifts in comparison to the experimental spectra.
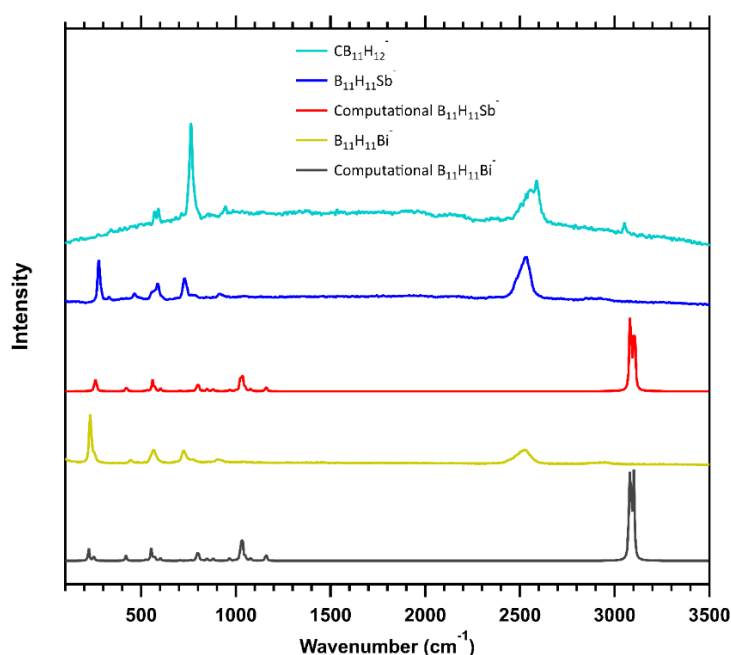
Figure 5.3. Raman spectroscopy of as-synthesised NaB$_{11}$H$_{11}$Sb, NaB$_{11}$H$_{11}$Bi and Zn(CB$_{11}$H$_{12}$)$_2$ performed in an inert argon atmosphere compared with computational spectra of the B$_{11}$H$_{11}$Bi$^-$ and B$_{11}$H$_{11}$Sb$^-$ anions. Zn(CB$_{11}$H$_{12}$)$_2$ was synthesised from the method used by Berger *et al.*[26].

Differential scanning calorimetry (DSC) was performed on the as-synthesised *closo*-borates to ascertain the thermodynamic events that occur along with any mass losses observed with thermogravimetric analysis (TGA). $LiB_{11}H_{11}Sb$ shows a large exothermic peak (or peaks) starting at 110 °C, which also coincides with a mass loss seen in the TGA data (Figure 5.4a). The exothermic peak likely corresponds to decomposition of the sample as desolvation is usually endothermic. Due to the relatively low temperature of this event, it was ensured that temperatures above 80 °C were not used in the synthesis of the compound. $NaB_{11}H_{11}Sb$ shows an exothermic peak at 230 °C, which also corresponds to a sharp drop in mass in the TGA (Figure 5.4b). This event likely also corresponds to decomposition. A similar trend in decomposition is seen in the bismuth containing salts, where $LiB_{11}H_{11}Bi$ shows a strong exothermic peak at 220 °C, which corresponds with a mass loss in the TGA plot (Figure 5.4c). Similarly, $NaB_{11}H_{11}Bi$ shows an exothermic peak starting at 350 °C (Figure 5.4d).

a – LiB$_{11}$H$_{11}$Sb

b – NaB$_{11}$H$_{11}$Sb
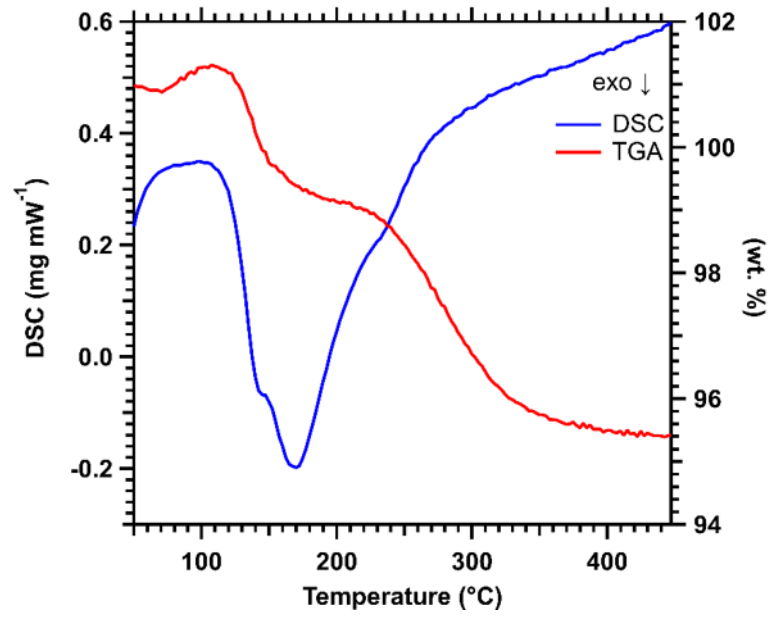
c – LiB$_{11}$H$_{11}$Bi
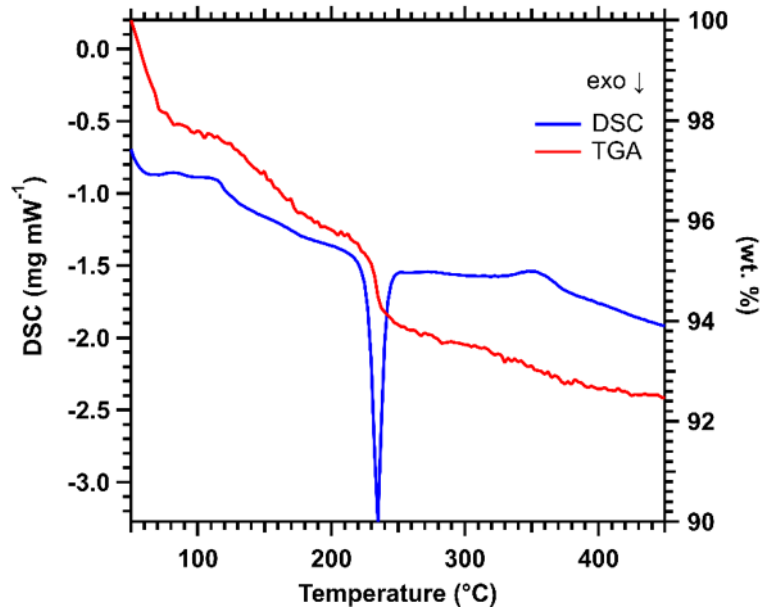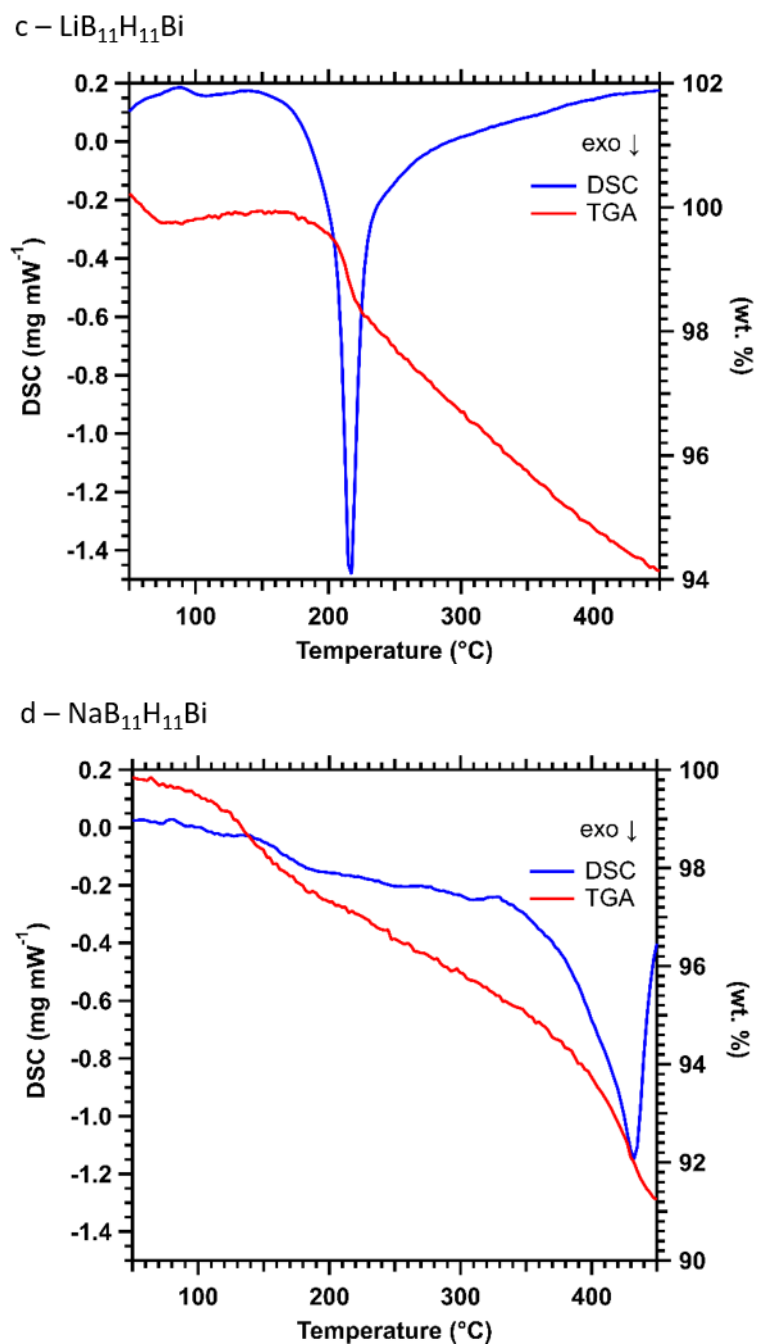
d – NaB$_{11}$H$_{11}$Bi

Figure 5.4a. DSC-TGA spectra of LiB$_{11}$H$_{11}$Sb heated to 450 °C at 10 °C min^{-1}. **b**. DSC-TGA spectra of NaB$_{11}$H$_{11}$Sb heated to 450 °C at 10 °C min^{-1}. **c.** DSC-TGA spectra of LiB$_{11}$H$_{11}$Bi heated to 10 °C min^{-1}. **d**. DSC-TGA spectra of NaB$_{11}$H$_{11}$Bi heated to 450 °C at 10 °C min^{-1}.

Powder X-Ray Diffraction (XRD) was performed on each material. The XRD pattern for LiB$_{11}$H$_{11}$Sb (Figure 5.5a) shows a lithium chloride impurity, which is a by-product formed during synthesis that was not completely removed. Most importantly, a low angle amorphous peak (18.5° 2θ) is also present, which shows that the as-synthesised LiB$_{11}$H$_{11}$Sb is amorphous and not crystalline, unlike most other *closo*-borate compounds.[33] The use of NMR and Raman

spectroscopy proves the presence of $LiB_{11}H_{11}Sb$ in the sample, but it is possible that the structure is amorphous due to partial solvation of the cation, which cannot be further desolvated due to the low temperature decomposition (> 110 °C) as shown by DSC-TGA.

The XRD pattern of $NaB_{11}H_{11}Sb$ shows the presence of some $Sb_2O_5 \cdot xH_2O$ by-product, but as with the lithium salt, the desired product, $NaB_{11}H_{11}Sb$, is amorphous. The presence of the desired product is confirmed by other techniques as mentioned with the lithium salt and is further reinenforced by the EDS analysis of the material (Figure C1). It shows a large intensity of boron and sodium alongside oxygen and antimony reinforces the bulk material being $NaB_{11}H_{11}Sb$, along with NMR and Raman spectroscopy results.

The XRD patterns for $LiB_{11}H_{11}Bi$ and $NaB_{11}H_{11}Bi$ show some additional crystalline phases along with potential amorphous humps, which could not be indexed nor identified as any known crystalline Li/Na-B-O-H-Cl-Bi material. It is believed that these crystalline peaks arise from the as-synthesised compounds themselves, as reinforced by the EDS spectra for these compounds. In addition, the NMR and Raman spectra show that the materials were synthesised, although the low intensity of the crystalline peaks in XRD data may indicate a large amorphous fraction. Further XRD investigation into these compounds and related high temperature phase changes can be identified using *in-situ* XRD studies using a temperature ramp. It may even be possible to perform XRD of as-synthesised compounds dried at room temperature, to see if more hydrated compounds are more crystalline.
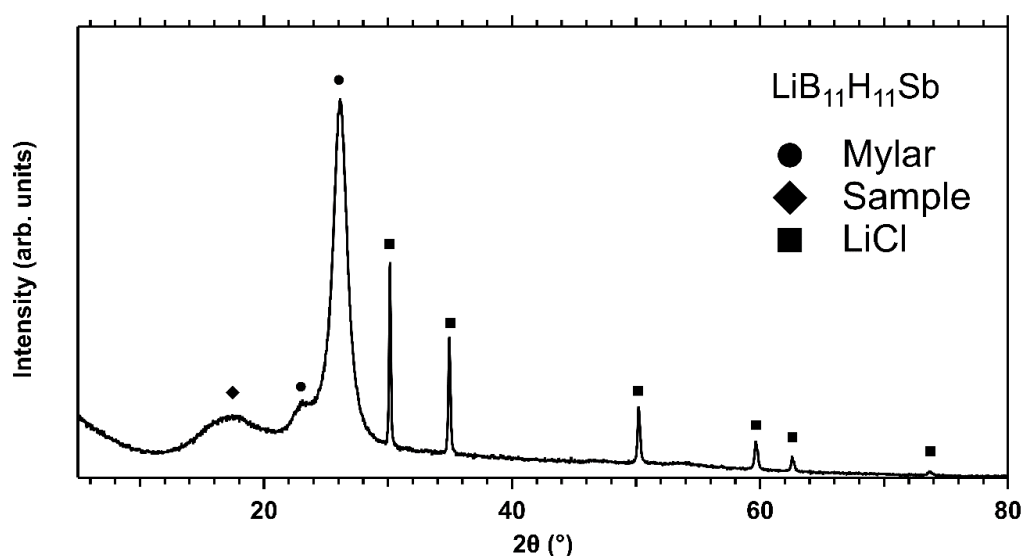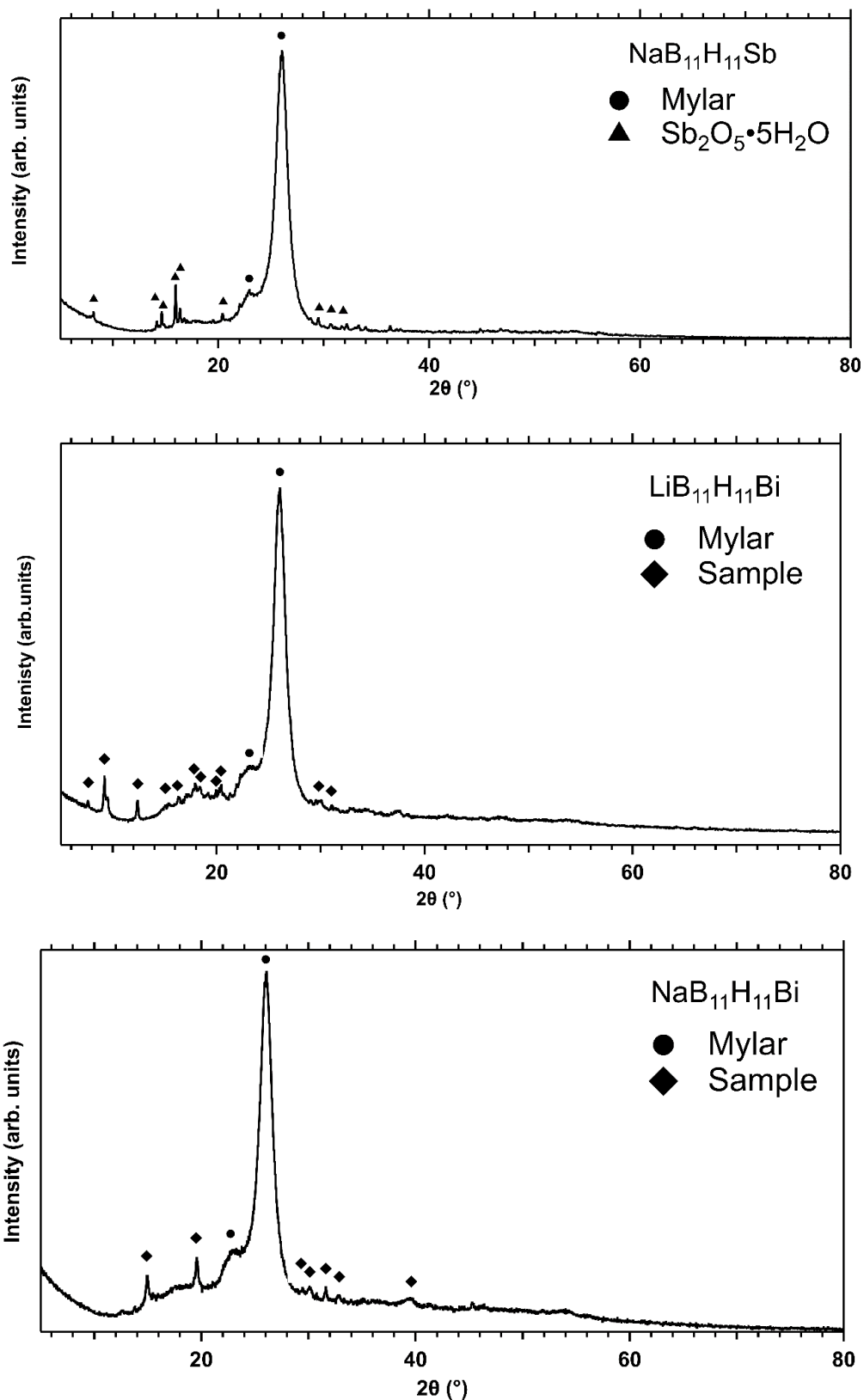
Figure 5.5a. XRD spectrum of $LiB_{11}H_{11}Sb$ covered by a MYLAR® film. λ = 1.54056 Å. **Figure 5.5b**. XRD spectrum of $NaB_{11}H_{11}Sb$ covered by a MYLAR® film. **Figure 5.5c.** XRD spectrum of $LiB_{11}H_{11}Bi$ covered by a MYLAR® film. Figure 5.5d. XRD spectrum of $NaB_{11}H_{11}Bi$ covered by a MYLAR® film.

The ionic conductivity of the stiba and bisma-*closo*-borate salts were measured using EIS as a function of temperature. Both $LiB_{11}H_{11}Sb$ and $LiB_{11}H_{11}Bi$ show low ion conductivity at 30 °C, below 1×10^{-8} S cm^{-1} (Figure 5.6a). This is lower than other substituted borohydride cluster salts such as $Li_2B_{11}H_{11}Sn$ and $Li_2B_{11}H_{11}Pb$ and far lower than the best performing lithium borate salt, $LiCB_{11}H_{12}$.[15] The ion conductivity improves with temperature for both compounds reaching a maximum for $LiB_{11}H_{11}Sb$ of 8×10^{-6} S cm^{-1} and 8×10^{-5} S cm^{-1} for $LiB_{11}H_{11}Bi$. This is possibly due to the decomposition of the material seen in the DSC-TGA analysis. This is also substantially lower than both the unsubstituted $Li_2B_{12}H_{12}$ (2×10^{-2} S cm^{-1} at 200 °C) and other substituted borohydride salts, $LiCB_{11}H_{12}$ (1×10^{-1} S cm^{-1} at 120 °C) and $Li_2B_{11}H_{11}Pb$ (1×10^{-2} S cm^{-1} at 110 °C).[24] It is difficult to analyse why the ionic conductivity is poor for the $LiB_{11}H_{11}Sb$ and $LiB_{11}H_{11}Bi$ salts without a crystal structure. It may be that the Li^+ cation is bound relatively strongly to the rather electronegative metal in the anion (Figure 5.1). It is clear that the mono-carborane shows a more distinct electrostatic dipole within the anion and undergoes a low temperature phase transition which aids ion conductivity.[15,26,34] The lack of these thermodynamic events seen in the DSC analysis show that this is not the case with $LiB_{11}H_{11}Sb$ and $LiB_{11}H_{11}Bi$.

The sodium salts show much better ionic conductivity at room temperature than their lithium analogues, with $NaB_{11}H_{11}Sb$ having a better ionic conductivity at room temperature than other sodium salts of heavy metal substituted borates (Figure 5.6b). $NaB_{11}H_{11}Sb$ has an ionic conductivity $\sim 1 \times 10^{-6}$ S cm^{-1} in comparison to 1×10^{-8} S cm^{-1} for $NaB_{11}H_{11}Bi$ and literature compounds $Na_2B_{11}H_{11}Sn$ (3×10^{-9} S cm^{-1}) and $Na_2B_{11}H_{11}Pb$ (8×10^{-9} S cm^{-1}).[24] $NaB_{11}H_{11}Sb$ show great promise in fact as this reaches superionic conductivity (above 1×10^{-3} S cm^{-1}) at 90 °C up to a maximum of 1×10^{-2} S cm^{-1} at 150 °C. $NaB_{11}H_{11}Bi$ also reaches superionic conductivity at 140 °C, reaching a maximum of 2×10^{-3} S cm^{-1} at 170 °C. $NaB_{11}H_{11}Sb$ shows impressive ionic performance, which is even an improvement on $NaCB_{11}H_{12}$ from 50 – 90 °C, which is the borohydride salt with the current best performance in its pure state.[12] However, at elevated temperature $NaCB_{11}H_{12}$ shows better performance to a maximum of 1×10^{-1} S cm^{-1} at 120 °C due to a change in cation dynamics, which arises from a polymorphic phase change.[15] The improved performance of sodium salts compared with the lithium salts is also seen with other cluster borohydride salts such as the $B_{10}H_{10}{}^{2-}$ salts.[17,35] This is due to the relationship between the size and charge density of the cation, which allows the cation

diffusion through the anionic lattice to be easier and therefore have a higher ionic conductivity.
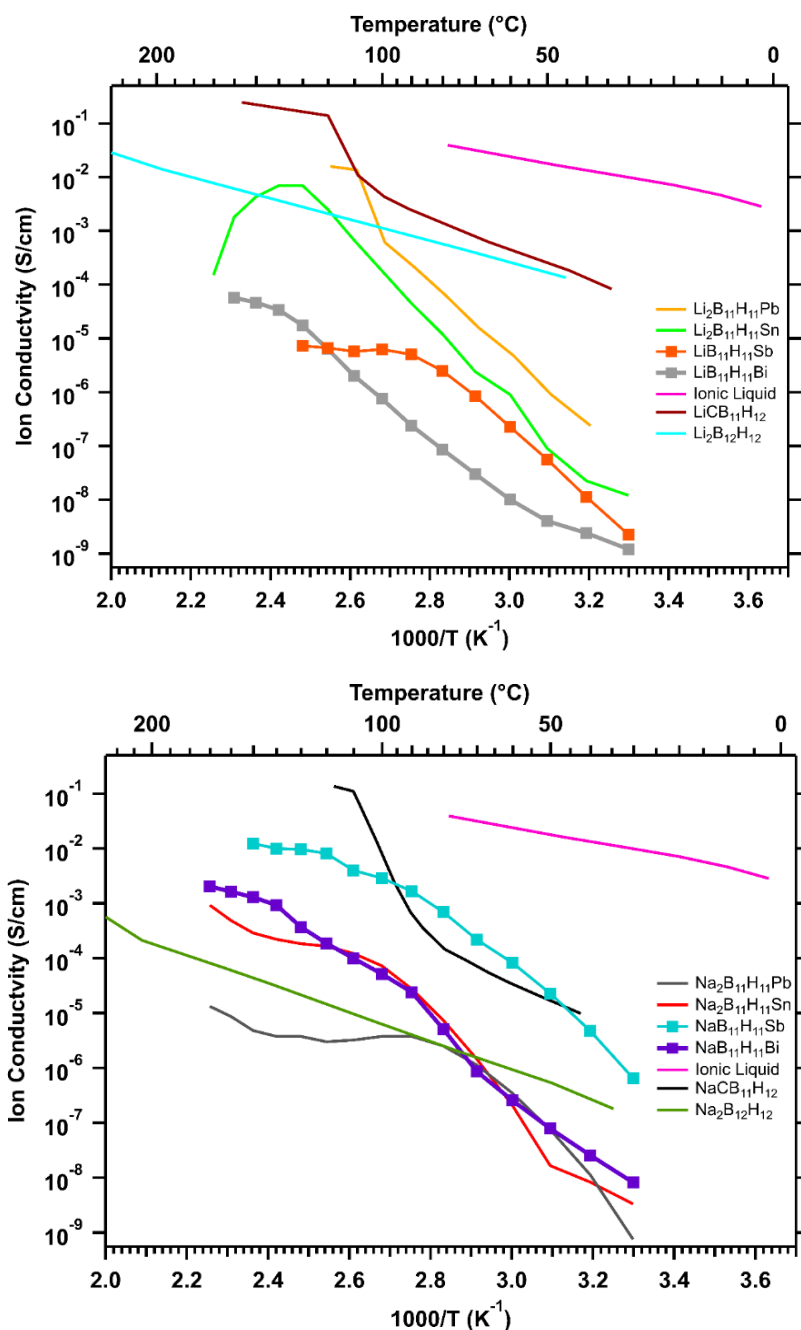

Figure 5.6a. Ion conductivity of $LiB_{11}H_{11}Sb$ and $LiB_{11}H_{11}Bi$ and comparable salts from literature. Ionic liquid – $LiBF_4/EMIB_4$.[15,24,36,37] **Figure 5.6b.** Ion conductivity of $NaB_{11}H_{11}Sb$ and $NaB_{11}H_{11}Bi$ and comparable salts from literature. Ionic liquid – $LiBF_4/EMIB_4$.[15,24,36,37]

5.5 Conclusions

A variety of heavy metal substituted, monovalent cluster borohydride salts were successfully synthesised from trimethylammonium *nido*-undecaborate, confirmed using NMR and Raman spectroscopies. $NaB_{11}H_{11}Sb$ shows high ionic conductivity with superionic conductivity reached above 90 °C to a maximum of 1×10^{-2} S cm^{-1} at 150 °C, which is higher than $NaCB_{11}H_{12}$, the previous best performance for a cluster borohydride salt. $NaB_{11}H_{11}Bi$ reaches superionic conductivity at 140 °C reaching a maximum of 2×10^{-3} S cm^{-1} at 170 °C. These monovalent sodium salts show increased performance to their lithium analogue possibly due to the lower charge density of the sodium ion being preferential to lithium. This indicates that the electrostatics could be more of a factor when it comes to diffusion activation energy than the size of the cation. The room temperature conductivities of these samples are comparatively low compared to other substituted borohydride cluster salts.

5.6 References

1   A. G. Olabi and M. A. Abdelkareem, *Renew. Sustain. Energy Rev.*, 2022, **158**, 112111.

2   D. Solyali, B. Safaei, O. Zargar and G. Aytac, *Int. J. Energy Res.*, 2022, **46**, 17786–17812.

3   M. Li, J. Lu, Z. Chen and K. Amine, *Adv. Mater.*, 2018, **30**, 1–24.

4   L. T. M. Le, T. D. Vo, K. H. P. Ngo, S. Okada, F. Alloin, A. Garg and P. M. L. Le, *J. Mol. Liq.*, 2018, **271**, 769–777.

5   A. M. Bates, Y. Preger, L. Torres-Castro, K. L. Harrison, S. J. Harris and J. Hewson, *Joule*, 2022, **6**, 742–755.

6   J. Nanda, C. Wang, P. Liu and G. Editors, 2018, **43**, 740–745.

7   H. Yang and N. Wu, *Energy Sci. Eng.*, 2022, **10**, 1643–1671.

8   L. Schweiger, K. Hogrefe, B. Gadermaier, J. L. M. Rupp and H. M. R. Wilkening, *J. Am. Chem. Soc.*, 2022, **144**, 9597–9609.

9   S. Song, Z. Yan, F. Wu, X. Zhang and Y. Xiang, *IOP Conf. Ser. Earth Environ. Sci.*, 2020, **461**, 0–8.

10   F. Tan, H. An, N. Li, J. Du and Z. Peng, *Nanoscale*, 2021, **13**, 11518–11524.

11   D. H. P. Souza, T. D. Humphries, Y. Liu, A. Gradišek, A. M. D'Angelo, C. E. Buckley and M. Paskevicius, *Sustain. Energy Fuels*, 2022, **6**, 4614–4625.

12   F. Cuevas, M. B. Amdisen, M. Baricco, C. E. Buckley, Y. W. Cho, P. De Jongh, L. M. De Kort, J. B. Grinderslev, V. Gulino, B. C. Hauback, M. Heere, T. Humphries, T. R. Jensen, S. Kim, K. Kisu, Y. S. Lee, H. W. Li, R. Mohtadi, K. T. Møller, P. Ngene, D. Noréus, S. I. Orimo, M. Paskevicius, M. Polanski, S. Sartori, L. N. Skov, M. H. Sørby, B. C. Wood, V. A. Yartys, M. Zhu and M. Latroche, *Prog. Energy*, 2022, **4**, 032001.

13   A. Unemoto, K. Yoshida, T. Ikeshoji and S. Orimo, 2016, **57**, 1639–1644.

14   T. J. Udovic, M. Matsuo, A. Unemoto, N. Verdal, V. Stavila, A. V. Skripov, J. J. Rush, H.

Takamura and S. I. Orimo, *Chem. Commun.*, 2014, **50**, 3750–3752.

15   W. S. Tang, A. Unemoto, W. Zhou, V. Stavila, M. Matsuo, H. Wu, S. I. Orimo and T. J. Udovic, *Energy Environ. Sci.*, 2015, **8**, 3637–3645.

16   C. Zhou, Y. Yan and T. R. Jensen, *ACS Appl. Energy Mater.*, 2023, **6**, 7346–7352.

17   T. J. Udovic, M. Matsuo, W. S. Tang, H. Wu, V. Stavila, A. V. Soloninin, R. V. Skoryunov, O. A. Babanova, A. V. Skripov, J. J. Rush, A. Unemoto, H. Takamura and S. I. Orimo, *Adv. Mater.*, 2014, **26**, 7622–7626.

18   A. V. Skripov, R. V. Skoryunov, A. V. Soloninin, O. A. Babanova, W. S. Tang, V. Stavila and T. J. Udovic, *J. Phys. Chem. C*, 2015, **119**, 26912–26918.

19   A. V. Soloninin, M. Dimitrievska, R. V. Skoryunov, O. A. Babanova, A. V. Skripov, W. S. Tang, V. Stavila, S. I. Orimo and T. J. Udovic, *J. Phys. Chem. C*, 2017, **121**, 1000–1012.

20   Z. Zhang and L. F. Nazar, *Nat. Rev. Mater.*, 2022, **7**, 389–405.

21   A. Lundén and M. A. K. L. Dissanayake, *J. Solid State Chem.*, 1991, **90**, 179–184.

22   M. Paskevicius, B. R. S. Hansen, M. Jørgensen, B. Richter and T. R. Jensen, *Nat. Commun.*, 2017, **8**, 10–15.

23   A. Berger, C. E. Buckley and M. Paskevicius, *Inorg. Chem.*, 2021, **60**, 14744–14751.

24   T. A. Hales, K. T. Møller, T. D. Humphries, A. M. D'Angelo, C. E. Buckley and M. Paskevicius, *J. Phys. Chem. C*, 2023, **127**, 949–957.

25   R. W. Chapman, J. G. Kester, K. Folting, W. E. Streib and L. J. Todd, *Inorg. Chem.*, 1992, **31**, 979–983.

26   A. Berger, A. Ibrahim, C. E. Buckley and M. Paskevicius, *Phys. Chem. Chem. Phys.*, 2023, **25**, 5758–5775.

27   B. R. S. Hansen, M. Paskevicius, M. Jørgensen and T. R. Jensen, *Chem. Mater.*, 2017, **29**, 3423–3430.

28   G. B. Dunks, K. Barker, E. Hedaya, C. Hefner, K. Palmer-Ordonez and P. Remec, *Inorg. Chem.*, 1981, **20**, 1692–1697.

29 T. A. Hales, A. M. D. Angelo, K. T. Møller, C. E. Buckley, T. D. Humphries and M. Paskevicius, *Phys. Chem. Chem. Phys.*,(Advance Article) , DOI:10.1039/d3cp03725h.

30 J. L. Little, M. A. Whitesell, J. G. Kester, K. Folting and L. J. Todd, *Inorg. Chem.*, 1990, **29**, 804–808.

31 D. H. P. Souza, K. T. Møller, S. A. Moggach, T. D. Humphries, A. M. D'Angelo, C. E. Buckley and M. Paskevicius, *J. Mater. Chem. A*, 2021, **9**, 15027–15037.

32 O. Volkov, K. Radacki, P. Paetxol and X. Zheng, *Z. Anorg. Allg. Chem.*, 2001, **627**, 1185–1191.

33 I. B. Sivaev, V. I. Bregadze and S. Sjöberg, *Collect. Czechoslov. Chem. Commun.*, 2002, **67**, 679–727.

34 S. Körbe, P. J. Schreiber and J. Michl, *Chem. Rev.*, 2006, **106**, 5208–5249.

35 K. Yoshida, T. Sato, A. Unemoto, M. Matsuo, T. Ikeshoji, T. J. Udovic and S. Orimo, *Appl. Phys. Lett.*, 2017, **110**, 103901.

36 Y. Sadikin, M. Brighi, P. Schouwink and R. Černý, *Adv. Energy Mater.*, 2015, **5**, 1501016.

37 B. R. S. Hansen, M. Paskevicius, H. W. Li, E. Akiba and T. R. Jensen, *Coord. Chem. Rev.*, 2016, **323**, 60–70.

Chapter 6

Summary Discussion

CHAPTER 6 - Summary Discussion

This thesis has focussed on the synthesis and conductive performance of various alkali metal salts of heavy metal substituted *closo*-dodecaborate anions. The synthetic methods for these novel salts were adapted from their relevant literature methods. These prior methods only produced the desired anions with bulky organic cations and isolation of their alkali metal salts was novel to the present study. These were successfully synthesised from an initial $NaBH_4$ precursor. Each synthesis starts by self-condensing $NaBH_4$, forming $NaB_{11}H_{14}$, then reacting with a base and the appropriate heavy metal halide. Synthesising the $B_{11}H_{11}Pb^{2-}$ salts uses aqueous conditions using a metal hydroxide as the main base alongside lead (II) chloride. The other salts were all synthesised using a non-aqueous route using *n*-butyllithium as the base for $B_{11}H_{11}Sn^{2-}$ and $B_{11}H_{11}Bi^-$ salts and triethylamine for $B_{11}H_{11}Sb^-$ salts. These salts were all synthesised with a small metal chloride impurity, formed during the isolation process, which was detected using XRD. However, this was not thought to be detrimental, due to the fact that inert non-conductive additives have previously been used to improve conductive performance.[1] All of the as-synthesised compounds were shown to be crystalline via XRD apart from $LiB_{11}H_{11}Sb$, which was found to be amorphous at room temperature.

The main aim of the research was to screen these compounds as potential solid-state electrolytes by measuring the ion conductivity of the samples at different temperatures. Figure 6.1 shows the ion conductivity of all synthesised lithium and sodium salts compared with similar compounds and the current best cluster borate ion salts, $CB_{11}H_{12}^-$.[2,3] The lithium salts show good ion conductivities, especially at temperatures above 100 °C. $Li_2B_{11}H_{11}Pb$ and $Li_2B_{11}H_{11}Sn$ show superionic conductivity above 80 °C and 110 °C respectively, however, the monovalent lithium salts do not reach this level of performance. Furthermore, the conductivity of the lithium samples is poorer than the state-of-the-art $LiCB_{11}H_{12}$ and the incumbent ionic liquid $LiBF_4/LiEMBF_4$ at all temperatures, as a result, despite showing promise, these samples do not show an improvement on modern technologies.[4]

The sodium salts show improved performance compared to their lithium analogues when compared to similar compounds found in literature. $Na_2B_{11}H_{11}Sn$ and $NaB_{11}H_{11}Bi$ both achieve superionic conductivity at high temperatures above 150 °C, whereas, $Na_2B_{11}H_{11}Pb$ does not

achieve superionic conductivity within the temperature parameters possible in this study. In comparison, NaB$_{11}$H$_{11}$Sb shows superionic conductivity at only 80 °C. This is an improvement on the best performing cluster borate sodium salt NaCB$_{11}$H$_{12}$, with NaB$_{11}$H$_{11}$Sb showing improved conductive performance between 50 and 100 °C. However, above this temperature the carborane shows better performance. This is due to a polymorphic phase transition into a highly conductive high temperature polymorph. All of the heavy metal substituted borate salts synthesised in the thesis do not undergo a phase change near ambient conditions and as a result they do not achieve the very highest levels of conductivity, which is shown in the carborane salts.
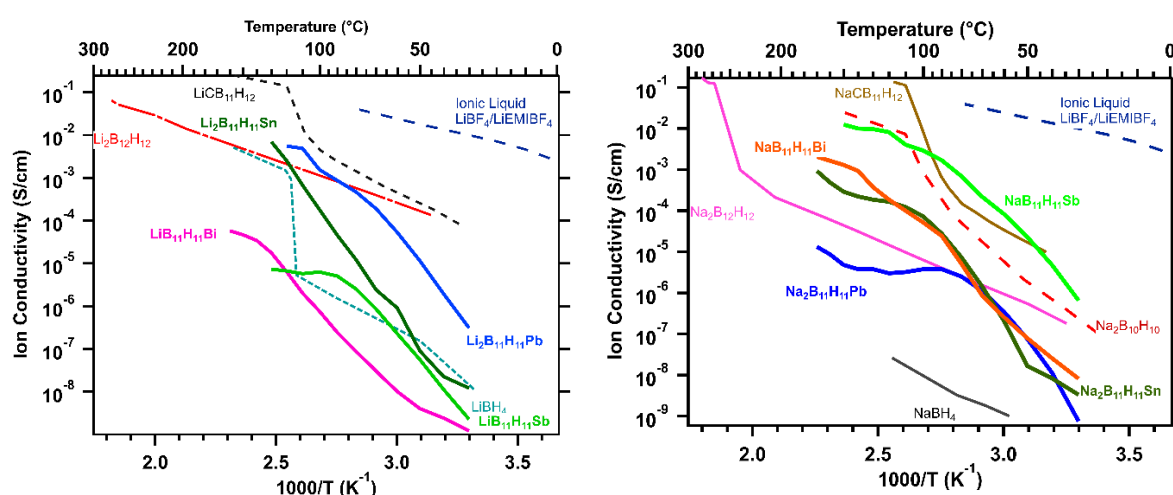
Figure 6.1. Ion conductivity of LiB$_{11}$H$_{11}$Sb and LiB$_{11}$H$_{11}$Bi and comparable salts from literature. Ionic liquid – LiBF$_4$/EMIB$_4$.[4–7] Figure 5.6b. Ion conductivity of NaB$_{11}$H$_{11}$Sb and NaB$_{11}$H$_{11}$Bi and comparable salts from literature. Ionic liquid – LiBF$_4$/EMIB$_4$.

Heavy metal substituted borate salts have been shown to have an improvement in conductive performance to the unsubstituted B$_{12}$H$_{12}$$^{2-}$ salts, with the sodium salts shown to achieve vastly higher ion conductivities at temperatures over 80 °C. Divalent lithium salts show improved performance over Li$_2$B$_{12}$H$_{12}$ between 100 – 130 °C, however, the substituted compounds see decreased performance and decomposition above this temperature. Despite good conductive performance for the compounds synthesised in this thesis, they are not suitable for use a solid-state electrolytes in room temperature application due to their low conductive at these temperatures. However, they provide insight into the mechanisms and trends for ionic

conductivity within weakly coordinated anionic salts, possibly allowing for better rational design of other materials in the future.

6.1 References

1   M. Martinez-Ibañez, E. Sanchez-Diez, L. Qiao, Y. Zhang, X. Judez, A. Santiago, I. Aldalur, J. Carrasco, H. Zhu, M. Forsyth, M. Armand and H. Zhang, *Adv. Funct. Mater.*, 2020, **30**, 1–9.

2   A. Berger, C. E. Buckley and M. Paskevicius, *Inorg. Chem.*, 2021, **60**, 14744–14751.

3   A. Berger, A. Ibrahim, C. E. Buckley and M. Paskevicius, *Phys. Chem. Chem. Phys.*, 2023, **25**, 5758–5775.

4   B. R. S. Hansen, M. Paskevicius, H. W. Li, E. Akiba and T. R. Jensen, *Coord. Chem. Rev.*, 2016, **323**, 60–70.

5   T. A. Hales, K. T. Møller, T. D. Humphries, A. M. D'Angelo, C. E. Buckley and M. Paskevicius, *J. Phys. Chem. C*, 2023, **127**, 949–957.

6   W. S. Tang, A. Unemoto, W. Zhou, V. Stavila, M. Matsuo, H. Wu, S. I. Orimo and T. J. Udovic, *Energy Environ. Sci.*, 2015, **8**, 3637–3645.

7   Y. Sadikin, M. Brighi, P. Schouwink and R. Černý, *Adv. Energy Mater.*, 2015, **5**, 1501016.

Chapter 7

Conclusion

CHAPTER 7 - CONCLUSION

This thesis focussed on developing and testing new materials that show promise as solid-state ion conductors for potential battery applications. A variety of metallo-*closo*-dodecaborate salts were successfully synthesised from sodium borohydride via trimethylammonium *nido*-undecaborate. The methods used were adapted from literature synthesis routes to produce novel group 1 metal salts. These salts were characterised and screened as potential solid-state electrolytes through a variety of physical techniques, such as NMR, FTIR, XRD, thermal analyses, and electrochemical techniques such as EIS and LSV.

Plumba-*closo*-dodecaborate salts were chosen to be investigated due to the polar nature of the anion, akin to the state-of-the-art $CB_{11}H_{12}^-$ salts, as calculated using electrostatic potential surfaces. The crystal structures of the different group 1 metal salts were dissimilar as determined by SR-XRD. The space group of $Li_2B_{11}H_{11}Pb$ was identified as $P4_2nm$ (102), however, the full crystal structure could not be identified due to the large disparity in the scattering power of the large $B_{11}H_{11}Pb^{2-}$ anions and small Li^+ cations. $Li_2B_{11}H_{11}Pb$ shows superionic conductivity ($\geq 1 \times 10^{-3}$ S cm^{-1}) from 90 – 120 °C to a maximum of 7 x 10^{-3} S cm^{-1} at 120 °C. At higher temperatures, the material desolvates, releasing water as confirmed from RGA-MS. The sodium and potassium salts show comparatively poor performance with low ion conductivity. Although, the plumba-*closo*-dodecaborate anions were polar, similar the carborane, they possessed a divalent charge, which may have limited ion conductivity through strong electrostatic cation-anion bonding.

In a similar fashion, a library of group 1 metal stanna-*closo*-dodecaborate salts were successfully synthesised and confirmed using ^{11}B and ^1H NMR spectroscopy along with computational and experimental Raman spectroscopy. $Na_2B_{11}H_{11}Sn$ and $K_2B_{11}H_{11}Sn$ shows polymorphic phase transitions at 200 and 250 °C, respectively, and a decomposition event at 340 °C for $Li_2B_{11}H_{11}Sn$ as confirmed by SR-XRD and DSC analysis. The high temperature polymorph of $K_2B_{11}H_{11}Sn$ could be indexed to have an orthorhombic space group but further structural information, for example, full crystal structures for these compounds was not possible. $Li_2B_{11}H_{11}Sn$ showed high ion conductivity above 1 mS cm^{-1} between 110 and 130 °C, however the conductivity reduces above this temperature due to desolvation, seen in the *in-*

situ-SR-XRD pattern. In addition, $Na_2B_{11}H_{11}Sn$ shows superionic conductivity above 170 °C, however both this and the conductivity of lithium salt were lower than the respective monovalent $CB_{11}H_{12}^-$ salt, the current cluster borohydride salts with the best performance.

To investigate other monovalent polar anions, stiba- and bisma-*closo*-dodecaborate salts were synthesised from trimethylammonium *nido*-undecaborate, as shown by NMR and experimental Raman spectroscopy. The stiba borate salts were shown to be amorphous by XRD analysis, whereas the bisma salts were unable to be indexed. However, the high intensity of boron in the EDS analysis of $NaB_{11}H_{11}Sb$ proves that the bulk material is the desired compound, although non-crystalline. The room temperatures ion conductivity of these samples are comparatively low compared with their contemporaries, however, improve at high temperatures. $NaB_{11}H_{11}Sb$ shows excellent superionic conductivity above 90 °C to a maximum of 1×10^{-2} S cm^{-1} at 150 °C, which is higher than the best borohydride cluster sodium salt, $NaCB_{11}H_{12}$. In addition, $NaB_{11}H_{11}Bi$ shows superb performance with superionic conductivity at 140 °C reaching a maximum of 2×10^{-3} S cm^{-1} at 170 °C. The lithium salts show comparatively low ion conductivity with respect to the sodium salts. This could be due to the lower charge density of the sodium ion being preferential, as a result, this could mean the electrostatics may be a greater factor in the diffusion energy of the cations rather than size.

The new class of compounds investigated in this thesis have shown that there is great promise in the rational design of new ion conductors for solid-state battery applications. Based on the body of literature and the results presented we are beginning to see trends in the structural nature of ion conductors with their ionic conductivity. The efforts herein to design polar anions showed some success, but the most favourable ion conductivity came from designing monovalent, weakly-coordinating anions that allowed for higher ion conductivity in general. It is clear the many other novel borate anions remain to be investigated as ion conductors, with great potential in achieving room temperature superionic conductivity with a pure alkali salt.

In conclusion, this project has synthesised a multitude of new compounds with the aim of screening them as possible solid-state ion conductors. Further work into these specific compounds could involve using these materials to construct full battery cells with a metal anode and an appropriate cathode material. Despite some impressive ion conductivities, the

oxidative stability of some of the metallo-borane salts was lower than expected, which may impact the long-term performance of solid-state batteries based on these new materials.

Appendix A

Supplementary Information for

"Investigating the potential of alkali metal plumba-*closo*-dodecaborate ($B_{11}H_{11}Pb^{2-}$) salts as solid-state battery electrolytes"

APPENDIX A
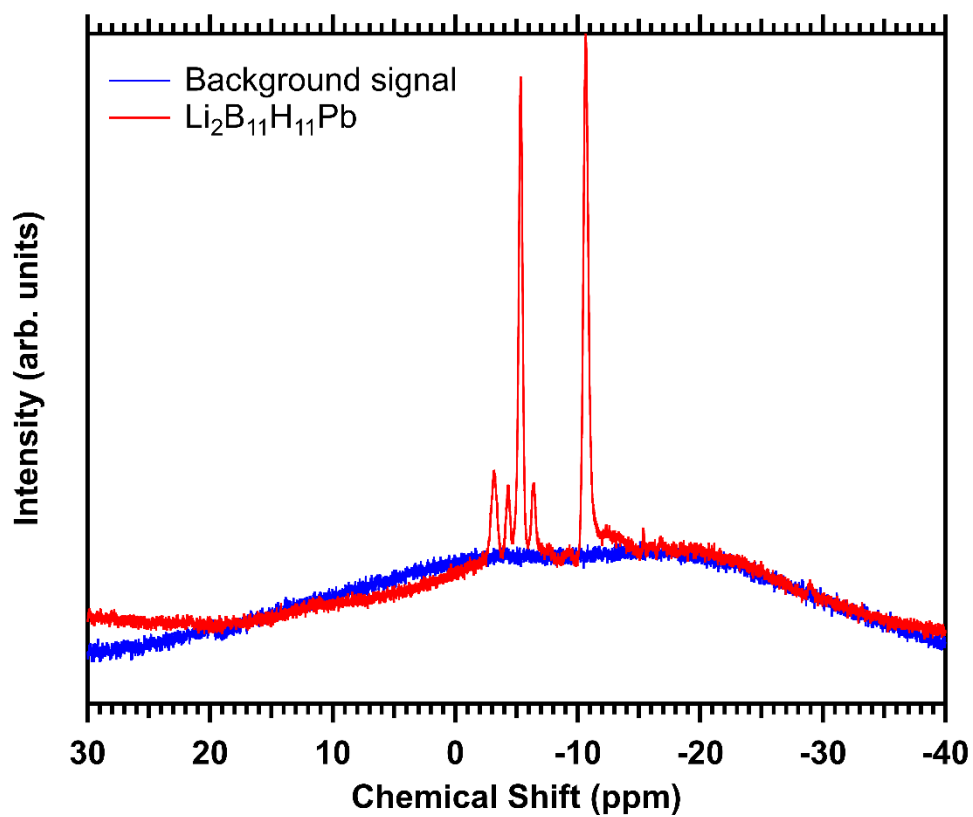
Figure A1. ^{11}B NMR data demonstrating the boron signal in the background due to the borosilicate probe coil inserts in the NMR instrument.
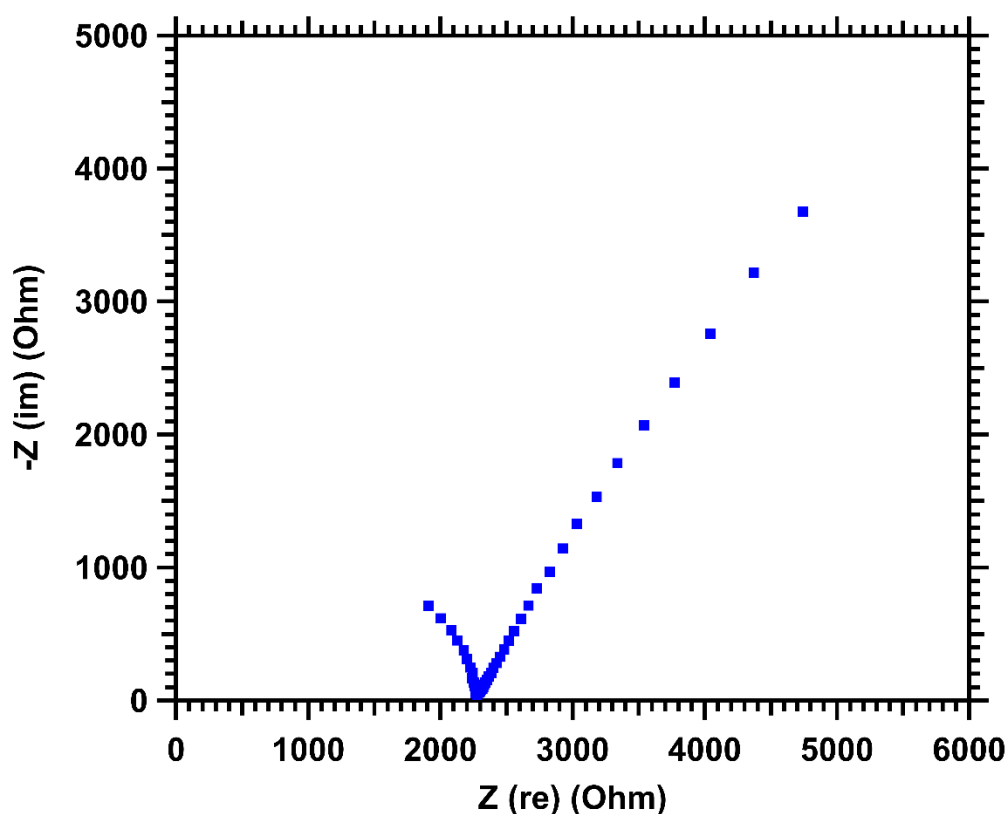
Figure A2. Nyquist plot of $Li_2B_{11}H_{11}Pb \bullet xH_2O$ at 90 °C

Table A1. Atomic Coordinates of $B_{11}H_{11}Pb^{2-}$ as calculated using Density Functional Theory (DFT) and a B3LYP/LanM2MB basis set (Total Self-Consistent Field (SCF) Density (isovalue = 0.008)) on Gaussian 09.

Atom	x	y	z
H1	-2.67220	1.23330	-2.23880
H2	-2.67280	-1.74790	-1.86510
H3	-2.67270	-2.31390	1.08640
H4	-2.67200	0.31790	2.53650
B1	-2.13750	0.73410	-1.33240
B2	-2.13740	1.49470	0.28650
B3	-2.13740	0.18930	1.50970
B4	-2.13790	-1.37740	0.64650
B5	-2.13790	-1.04050	-1.11000
H5	-2.67220	2.51100	0.48110

H6	-0.30210	2.45190	-1.15160
H7	-0.30250	-0.33700	-2.68740
H8	-0.30200	-2.66030	-0.51010
H9	-0.30210	-1.30810	2.37180
B6	-0.65670	1.09450	1.16760
B7	-0.65670	1.44870	-0.68010
B8	-0.65680	-0.19950	-1.58740
B9	-0.65650	-1.57160	-0.30150
B10	-0.65650	-0.77280	1.40110
H10	-0.30200	1.85230	1.97650
B11	-3.06710	0.00030	0.00020
H11	-4.23150	0.00040	0.00030
Pb1	1.27190	0.00000	0.00000
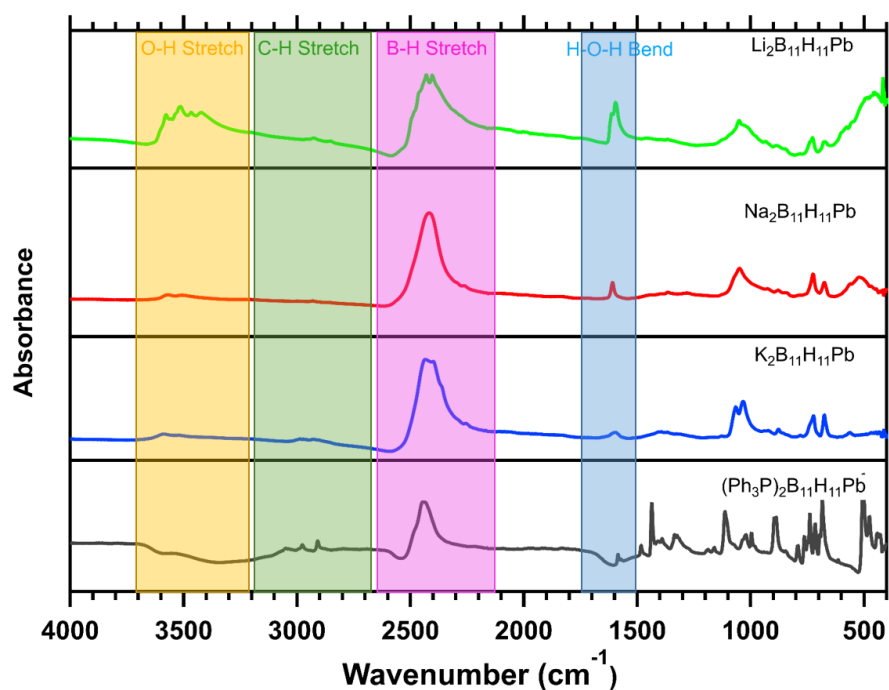
Figure A3. FTIR spectra (ATR) of as-synthesised alkali metal $B_{11}H_{11}Pb^{2-}$ salts and $(Ph_3P)_2B_{11}H_{11}Pb$
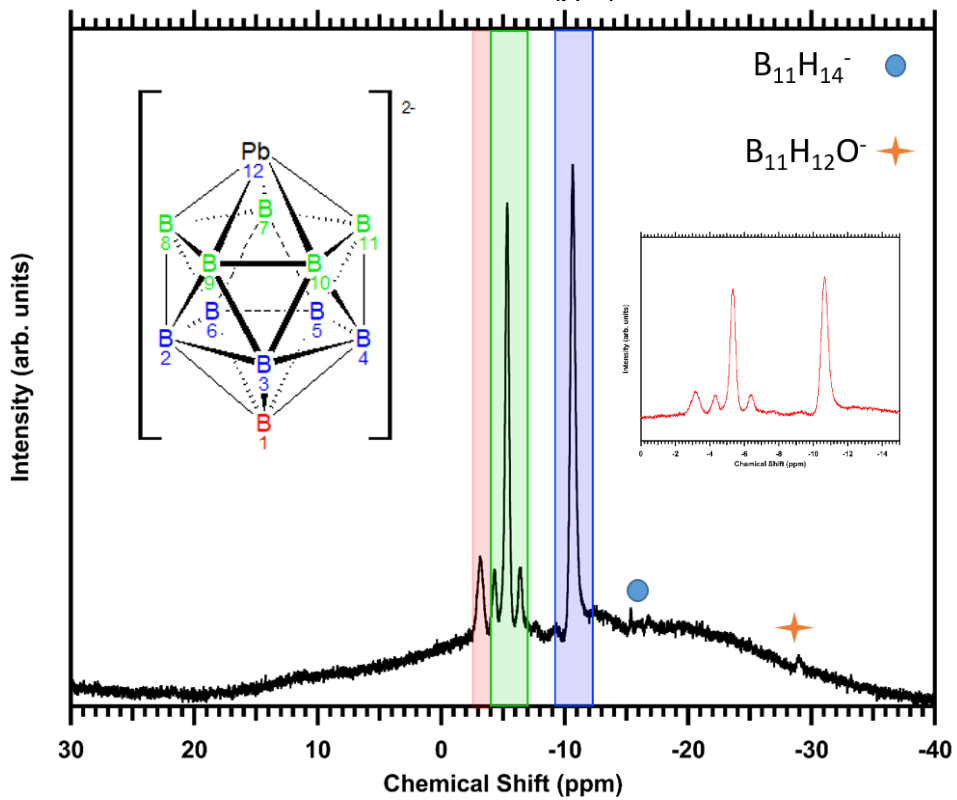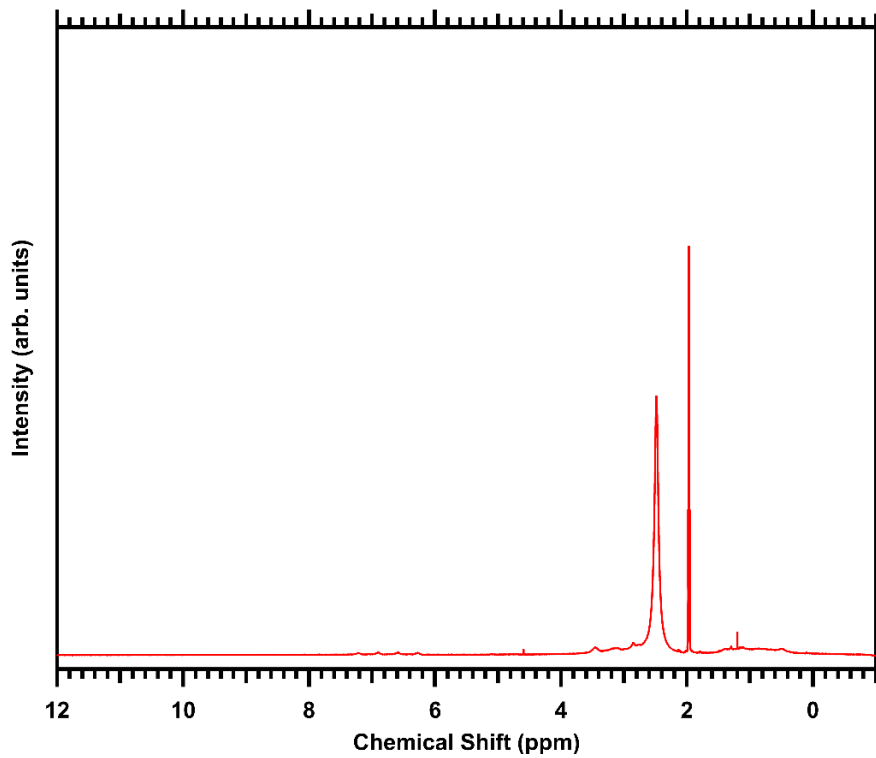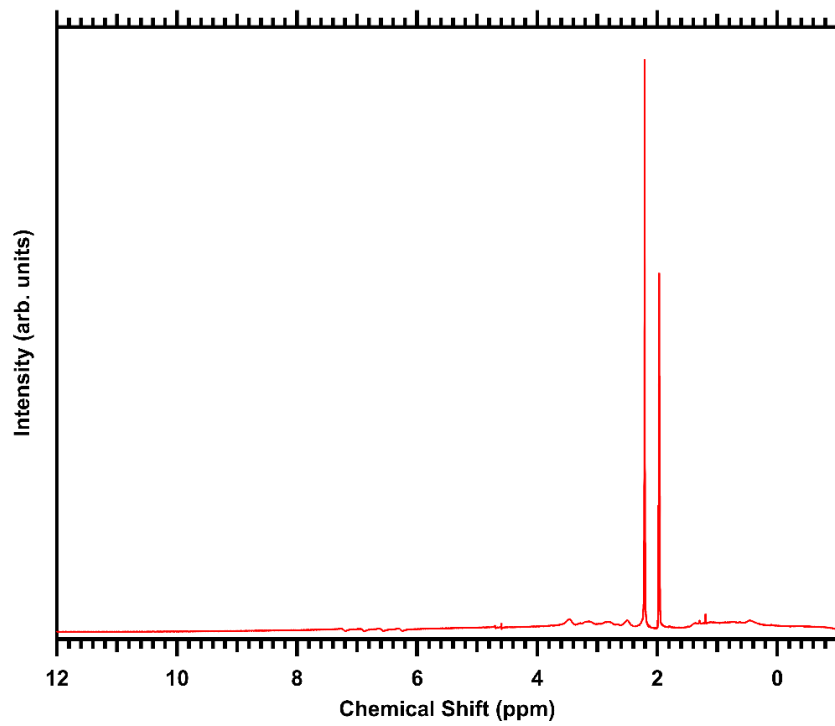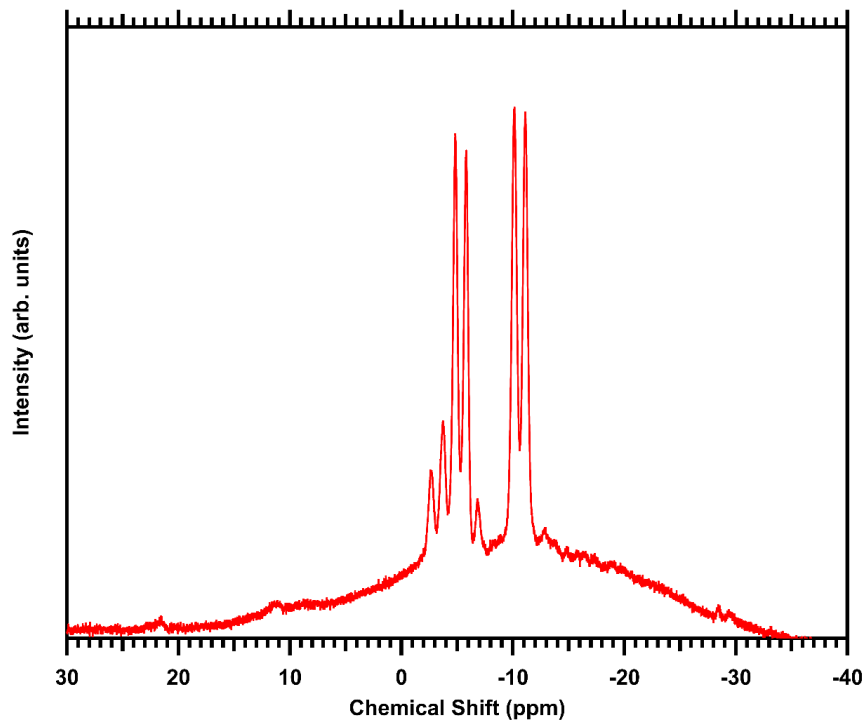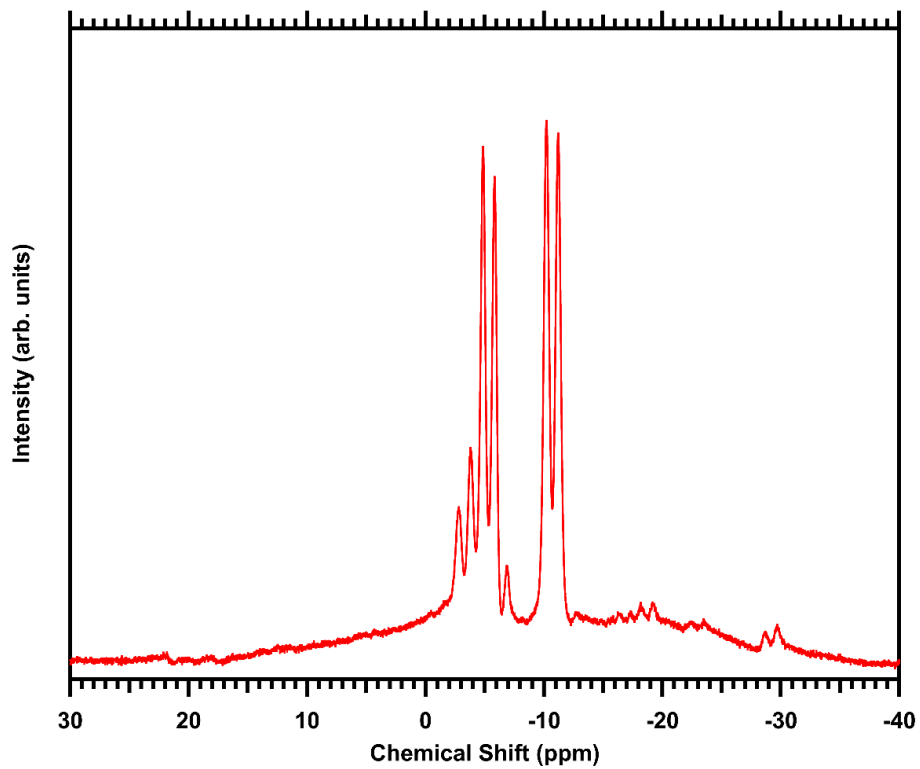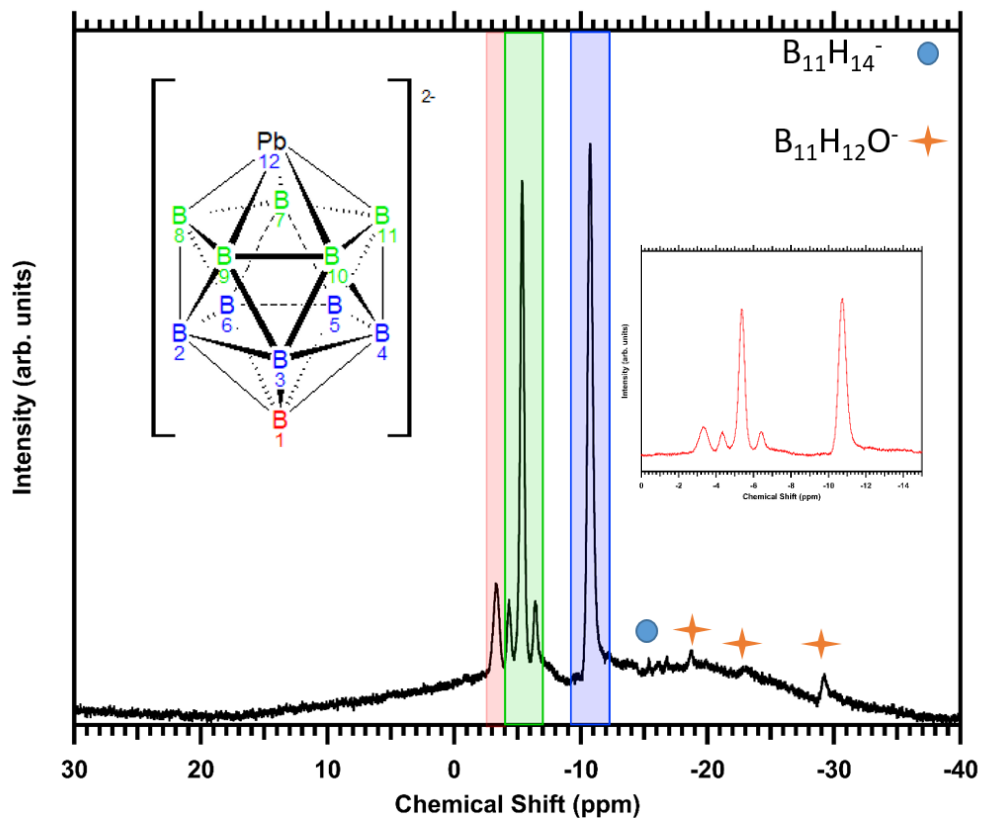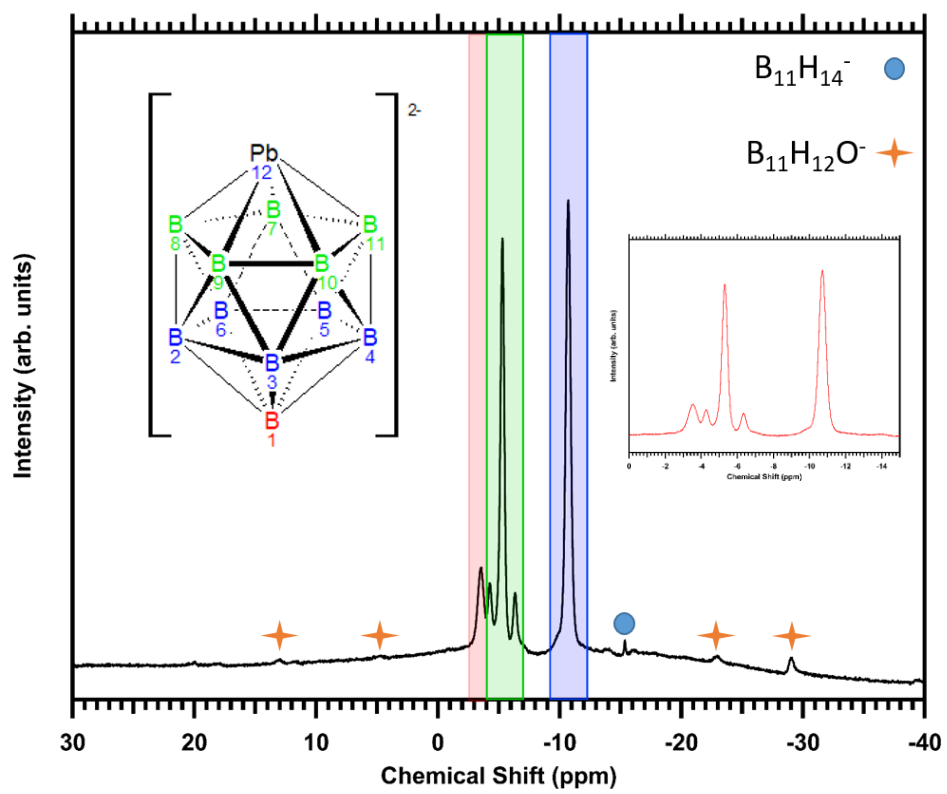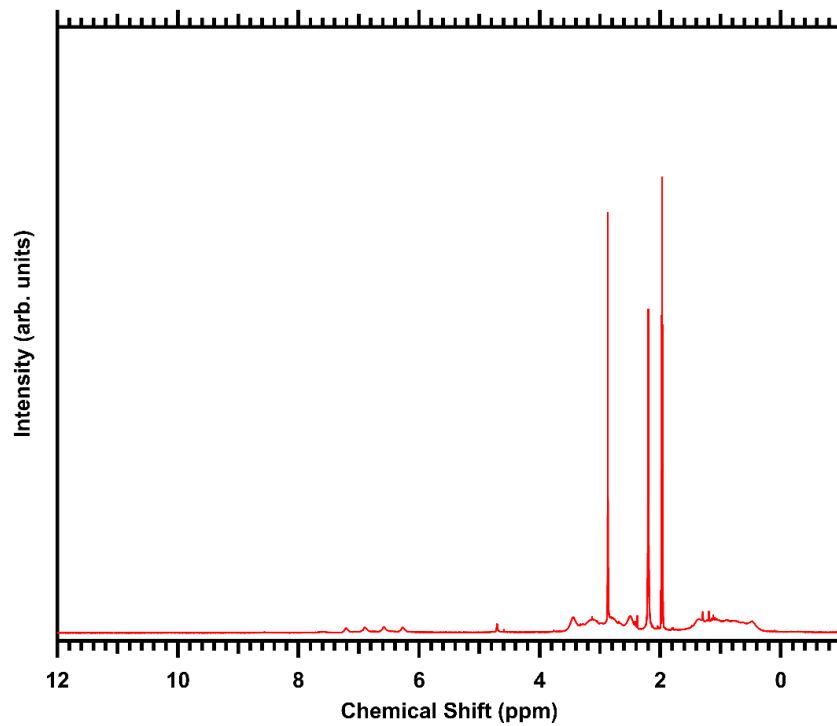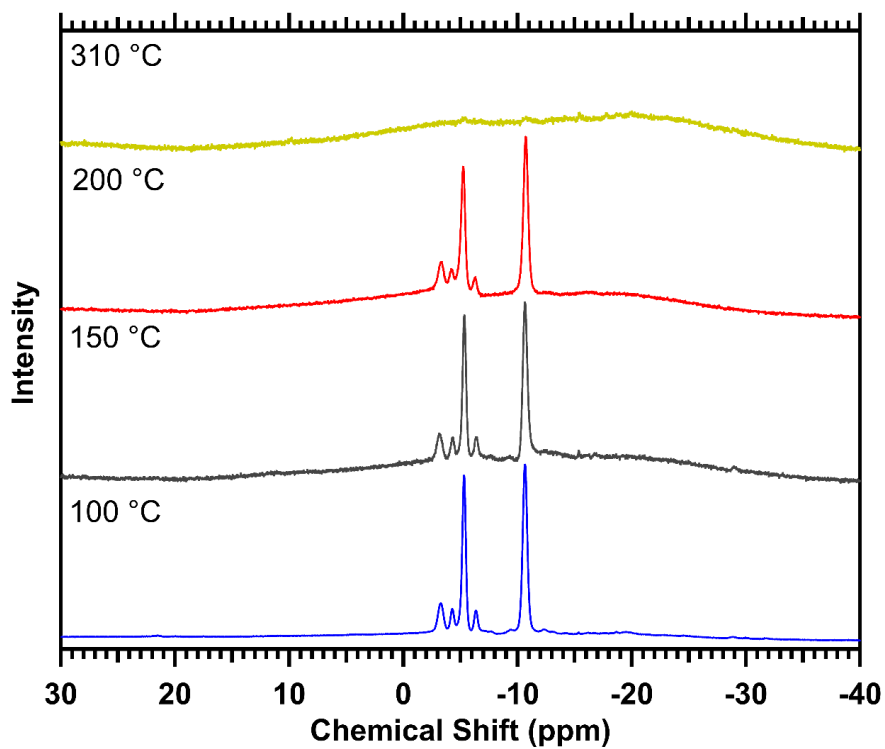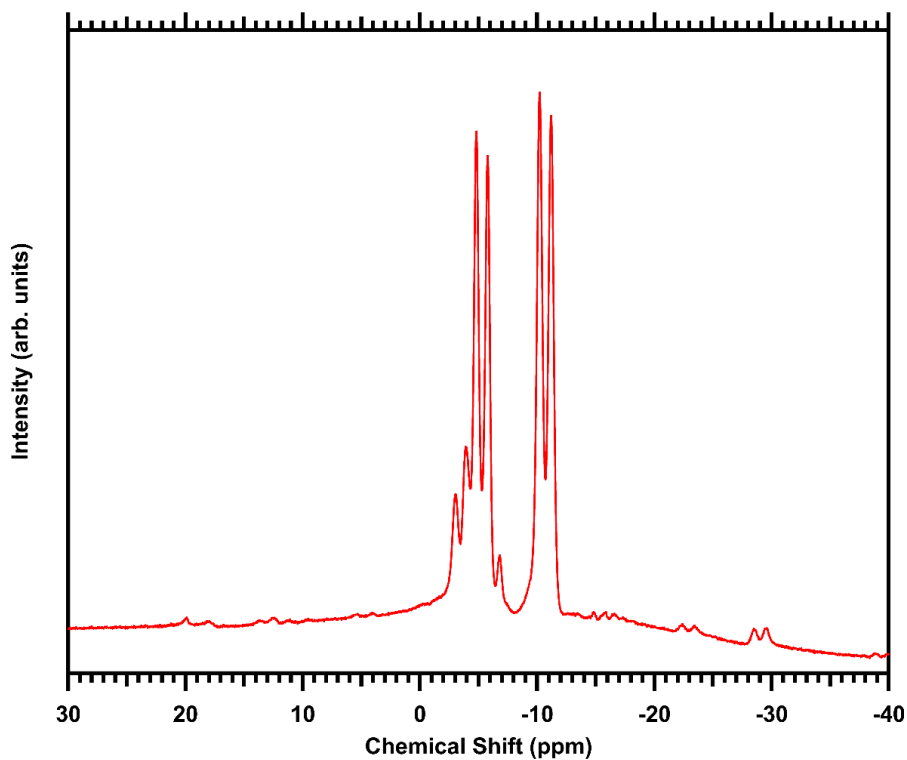
Figure A4a. ^{1}H NMR spectrum of $Li_2B_{11}H_{11}Pb$ in CD_3CN. **Figure A4b**. ^{11}B {^{1}H} NMR spectrum of

$Li_2B_{11}H_{11}Pb$ in CD_3CN. **Figure A4c**. ^{11}B NMR spectrum of $Li_2B_{11}H_{11}Pb$ in $CD_3CN-5.4$ (t, $^1J_{^{11}B-^{207}Pb}$ = 263

Hz, 5B), −10.8 (d, $^1J_{^{11}B-^1H}$ = 166 Hz, 5B**). Figure A4d.** ^{1}H NMR spectrum of $Na_2B_{11}H_{11}Pb$ in CD_3CN.

Figure A4e. ^{11}B {^{1}H} NMR spectrum of $Na_2B_{11}H_{11}Pb$ - −5.4 (t, $^1J_{^{11}B-^{207}Pb}$ = 263 Hz, 5B), −10.8 (d, $^1J_{^{11}B-^1H}$ = 166 Hz, 5B). **Figure A4f.** ^{11}B NMR spectrum of $Na_2B_{11}H_{11}Pb$ in CD_3CN. **Figure A4g.** ^{1}H NMR spectrum of $K_2B_{11}H_{11}Pb$ in CD_3CN**. Figure A4h**. ^{11}B {^{1}H} NMR spectrum of $K_2B_{11}H_{11}Pb$ in CD_3CN - −5.4 (t, $^1J_{^{11}B-^{207}Pb}$ = 263 Hz, 5B), −10.8 (d, $^1J_{^{11}B-^1H}$ = 166 Hz, 5B). **Figure A4i.** ^{11}B NMR spectrum of $K_2B_{11}H_{11}Pb$ in CD_3CN. **Figure A4k.** ^{11}B {^{1}H} NMR spectra of $Li_2B_{11}H_{11}Pb$ in CD_3CN after heating the material *in vacuo* to 100, 150, 200 and 310 °C.
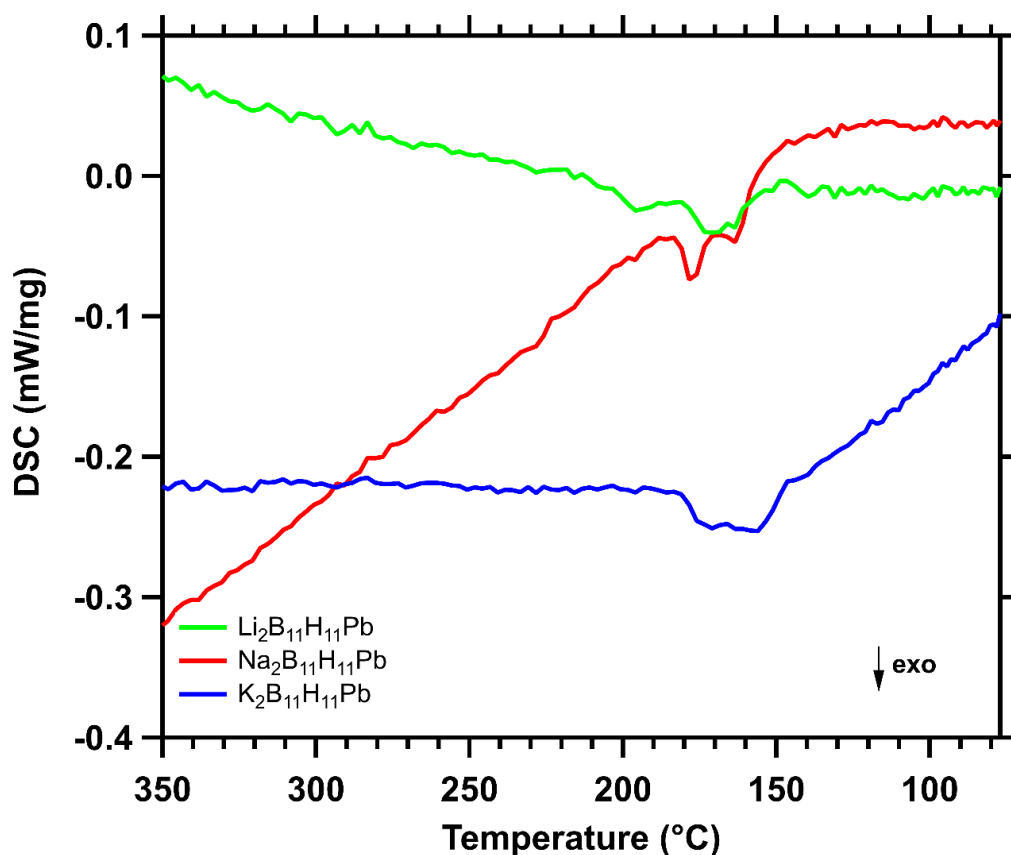
Figure A5. DSC spectra of $Li_2B_{11}H_{11}Pb$, $Na_2B_{11}H_{11}Pb$ and $K_2B_{11}H_{11}Pb$ when cooling from 350 °C to 75 °C at 10 °C min^{-1}.
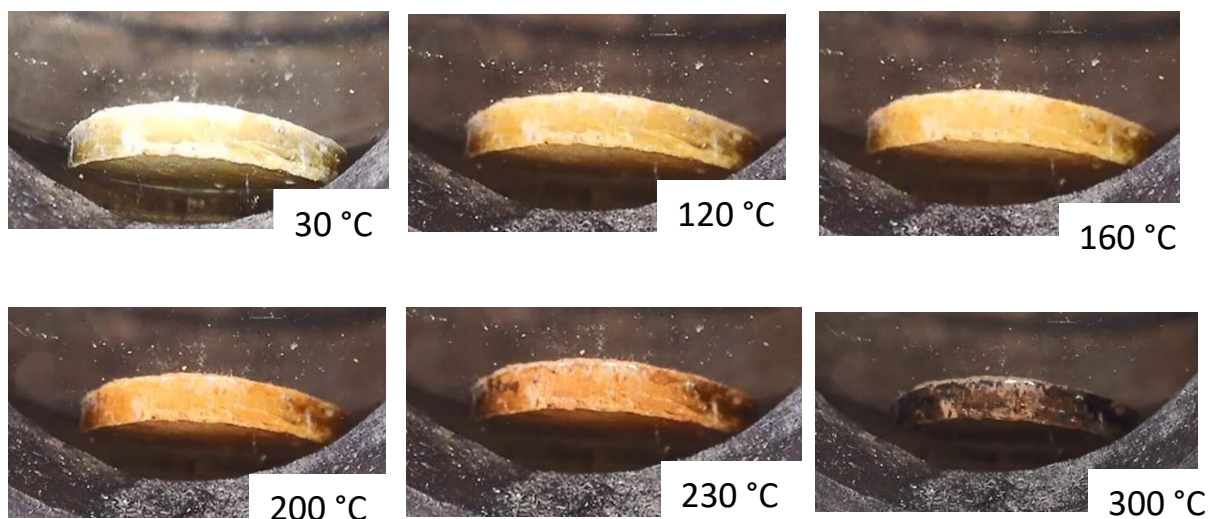
Figure A6a. Temperature Programmed Photographic Analysis (TPPA) of $Li_2B_{11}H_{11}Pb$ at a heating rate 5 °C min^{-1} under an argon atmosphere
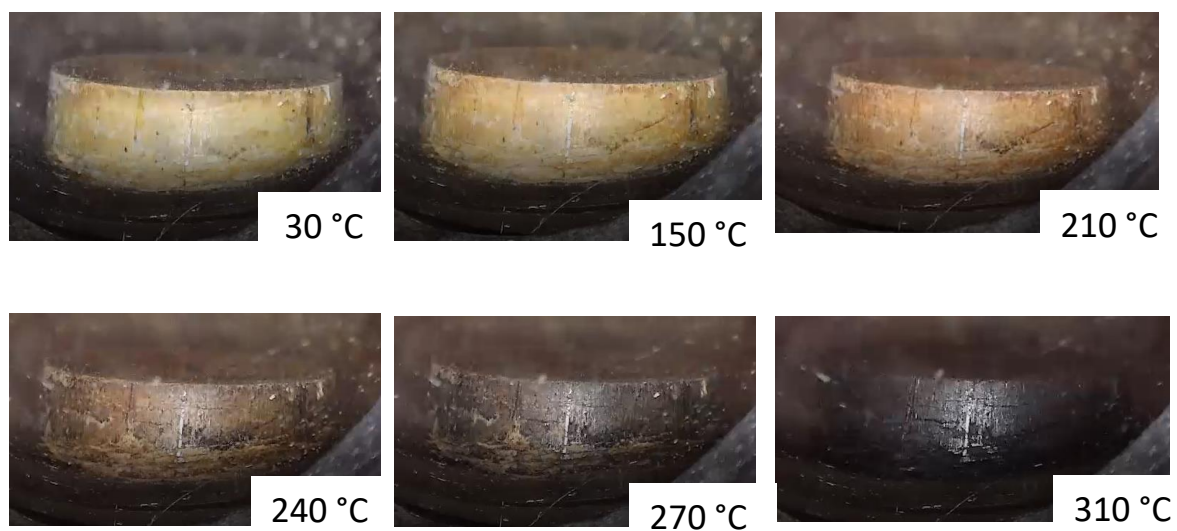
Figure A6b. Temperature Programmed Photographic Analysis (TPPA) of $Na_2B_{11}H_{11}Pb$ at a heating rate 5 °C min^{-1} under an argon atmosphere.

250 °C   280   305 °C

Figure A6c. Temperature Programmed Photographic Analysis (TPPA) of $K_2B_{11}H_{11}Pb$ at a heating rate 5 °C min^{-1} under an argon atmosphere

Figure A6. Temperature Programmed Photographic Analysis (TPPA) of alkali metal plumbadodecaborate salts at a heating rate 5 °C min^{-1} under an argon atmosphere.
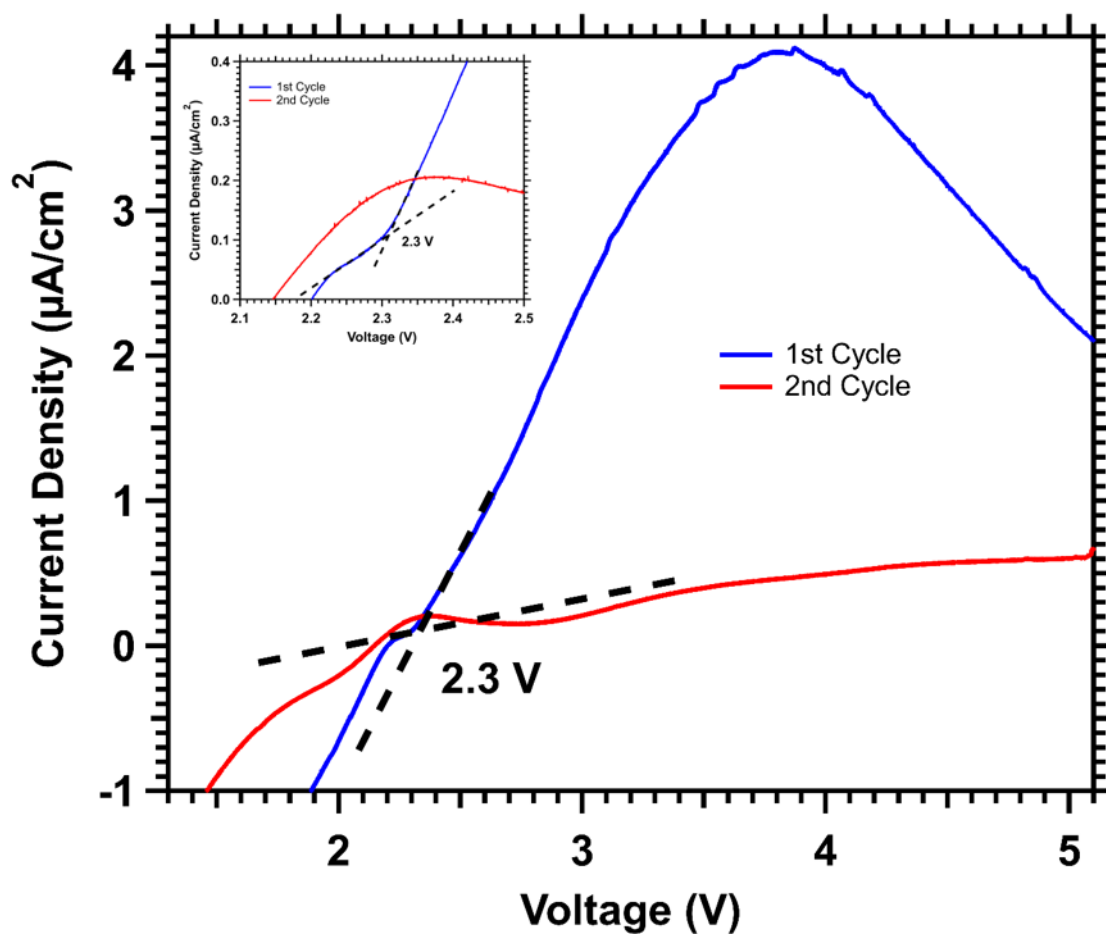
Figure A7. Linear Sweep Voltammetry of $Li_2B_{11}H_{11}Pb$ at 60 °C with a scan rate of 50 µV s^{-1} from 1.5 to 5 V to determine the oxidative stability limit.

Appendix B

Supplementary Information for

"Stannaborates: Tuning the Ion

Conductivity of Dodecaborate Salts with

Tin Substitution"

APPENDIX B
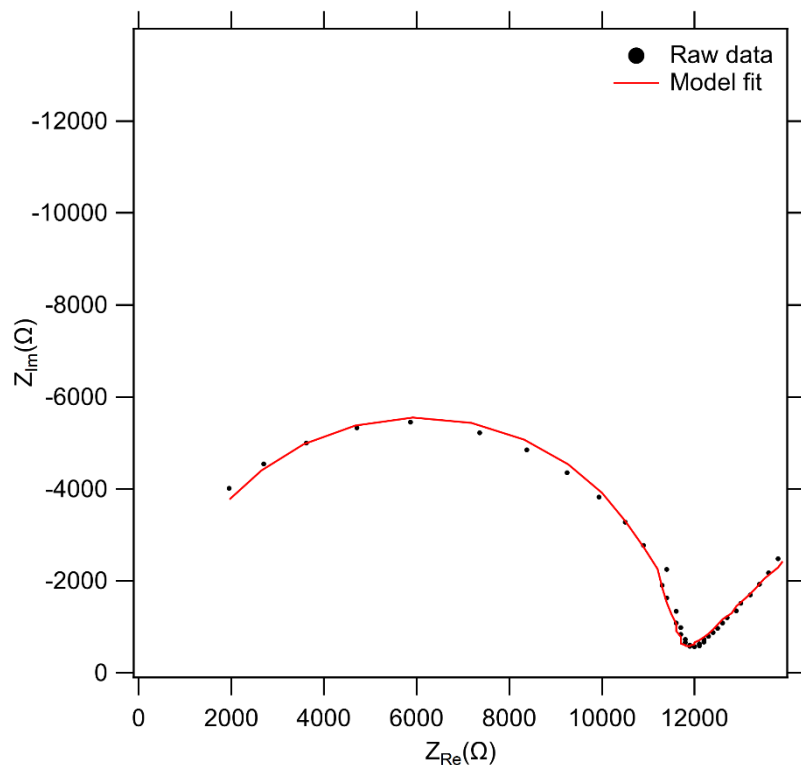
Figure B1. Example of a Nyquist plot of $Na_2B_{11}H_{11}Sn \bullet xH_2O$ at 90 °C, using an R_s-$R_1|C_1$-W circuit model.

Table B1. Atomic Coordinates of $B_{11}H_{11}Sn^{2-}$ ion

Atom No.	x	y	z
B1	0.255802	0.755762	0.881357
B2	0.205457	0.894609	0.780497
B3	0.372747	0.838548	0.775072
B4	0.371572	0.661241	0.785832
B5	0.201589	0.607139	0.794924
B6	0.100840	0.752155	0.796693
B7	0.110495	0.651556	0.650069
B8	0.112575	0.840286	0.642544
B9	0.294824	0.895553	0.627062
B10	0.403098	0.739727	0.631714
B11	0.289579	0.589437	0.644272
H1	0.262282	0.770772	0.998774
H2	0.172624	1.000000	0.823749
H3	0.459391	0.898628	0.829284

H4	0.459451	0.596902	0.832650
H5	0.175126	0.513352	0.862449
H6	0.000000	0.747252	0.858852
H7	0.019250	0.590763	0.604969
H8	0.018325	0.903601	0.608425
H9	0.336478	0.993048	0.574005
H10	0.508037	0.741887	0.576607
H11	0.313340	0.478982	0.608365
Sn1	0.233488	0.735628	0.482036
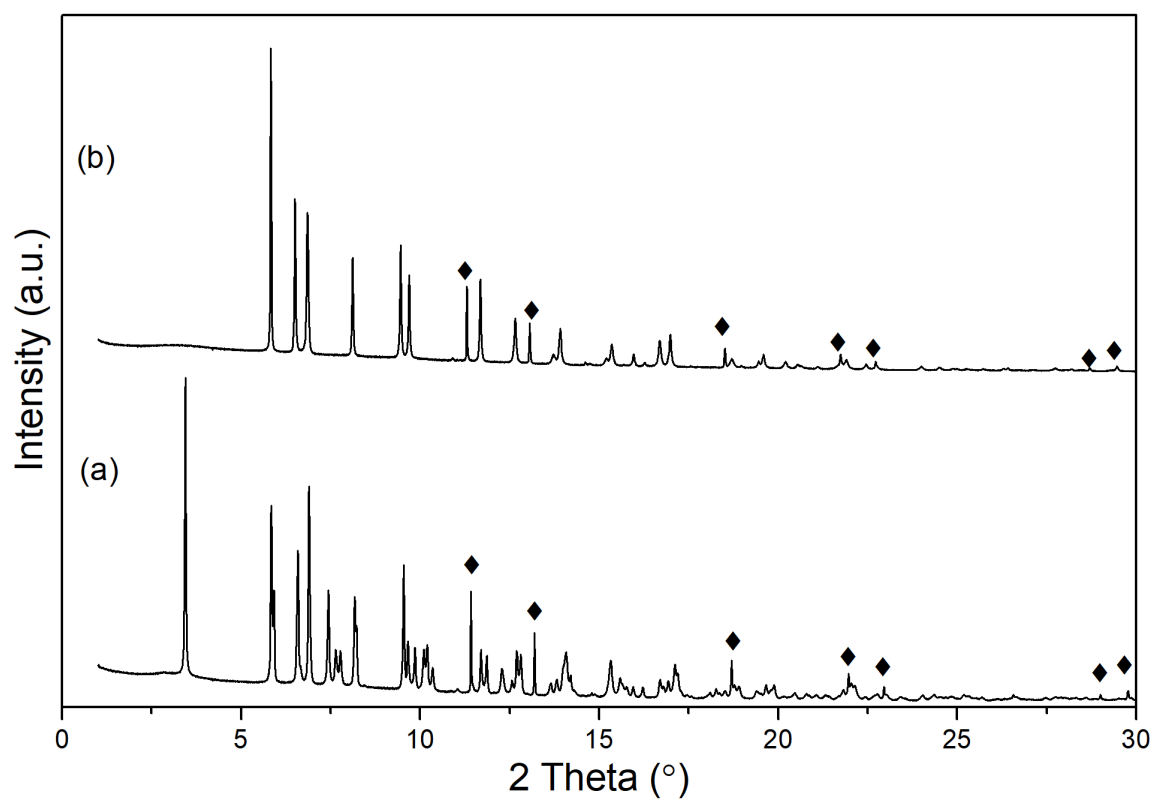
Figure B2. Synchrotron XRD pattern of $Li_2B_{11}H_{11}Sn$ at (a) room temperature and (b) 230 °C. Diamonds represent the peaks for LiCl. λ = 0.59096(1)Å.
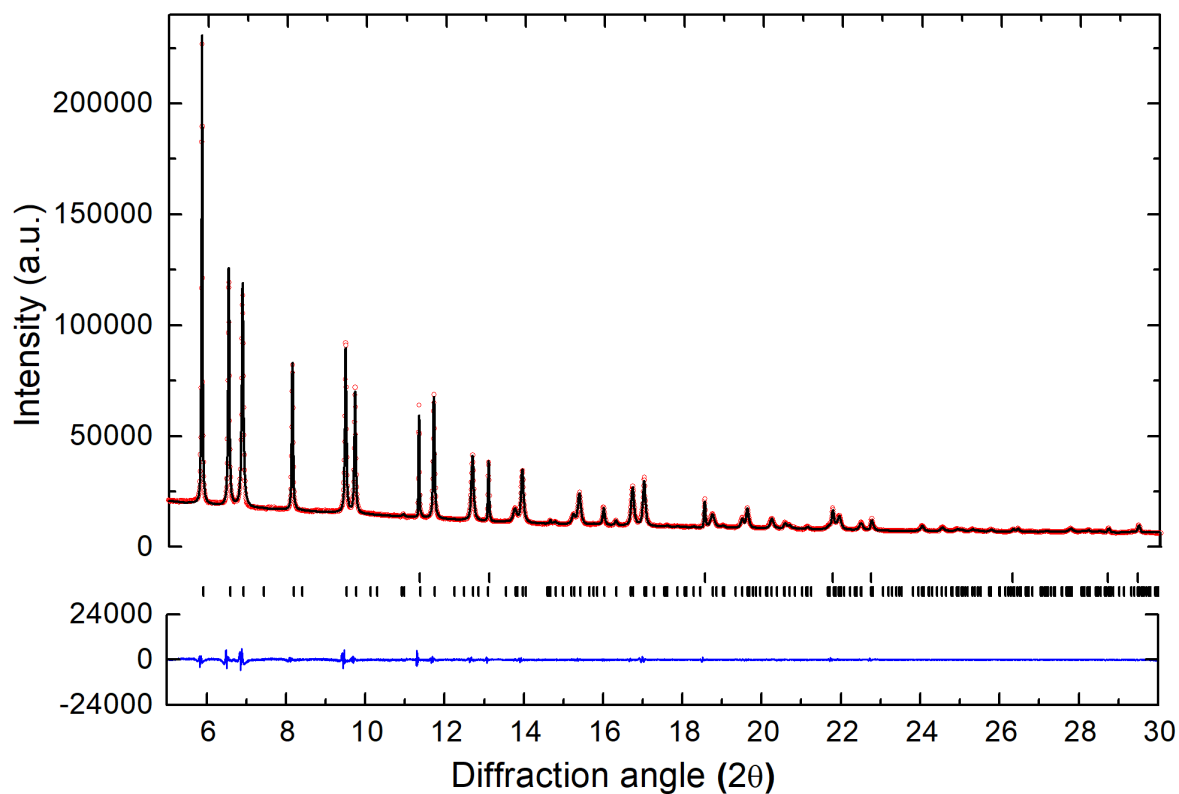
Figure B3. Synchrotron XRD pattern and Le Bail fit of $Li_2B_{11}H_{11}Sn$ at 230 °C. Experimental data as red circles, calculated diffraction pattern as black line and the difference plot in blue. Tick marks show positions for LiCl and $Li_2B_{11}H_{11}Sn$, top to bottom respectively. λ = 0.59096(1)Å. Le Bail plot for employed *hkl*'s for $Li_2B_{11}H_{11}Sn$ generated using space group *P*42/*ncm* with unit cell parameters *a* = *b* = 9.8923(4), *c* = 10.4149(3) giving an R_{wp} = 2.141.
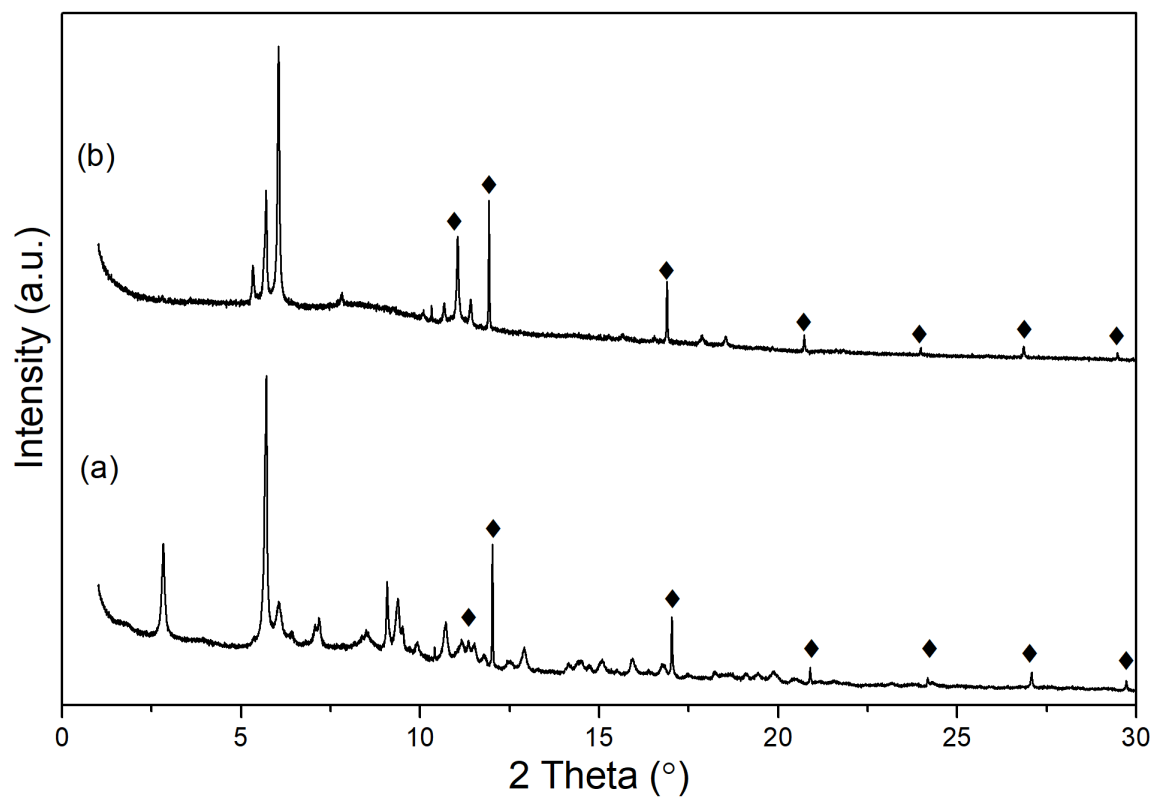
Figure B4. Synchrotron XRD pattern of $Na_2B_{11}H_{11}Sn$ at (a) room temperature and (b) 217 °C.

Diamonds represent the peaks for NaCl. $\lambda = 0.59096(1)$Å.
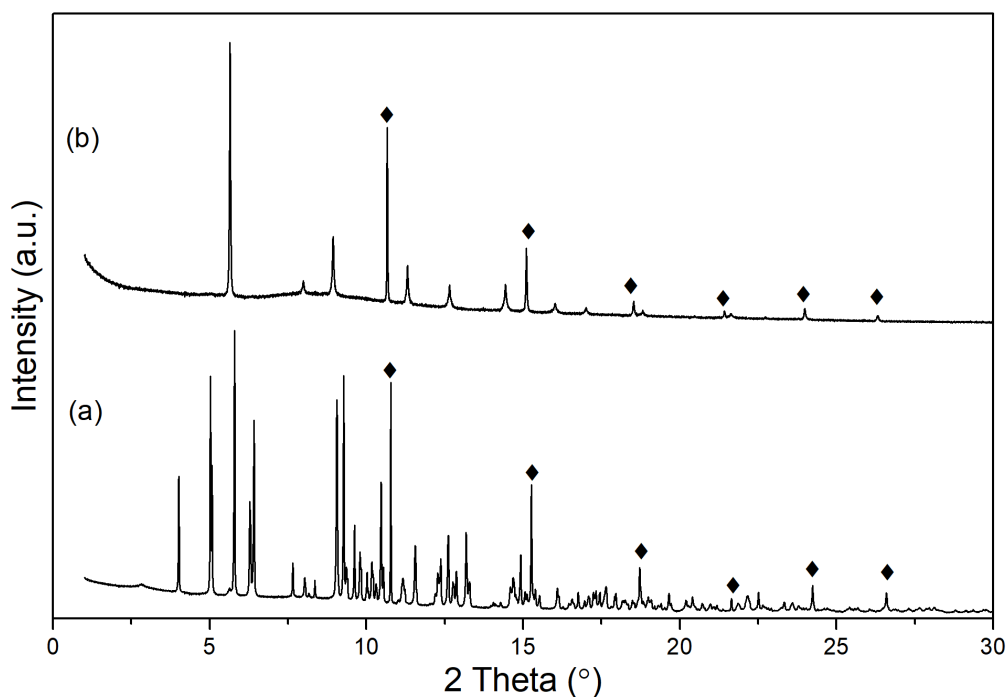
Figure B5. Synchrotron XRD pattern of $K_2B_{11}H_{11}Sn$ at (a) room temperature and (b) 278 °C. Diamonds represent the peaks for KCl. λ = 0.59096(1)Å.
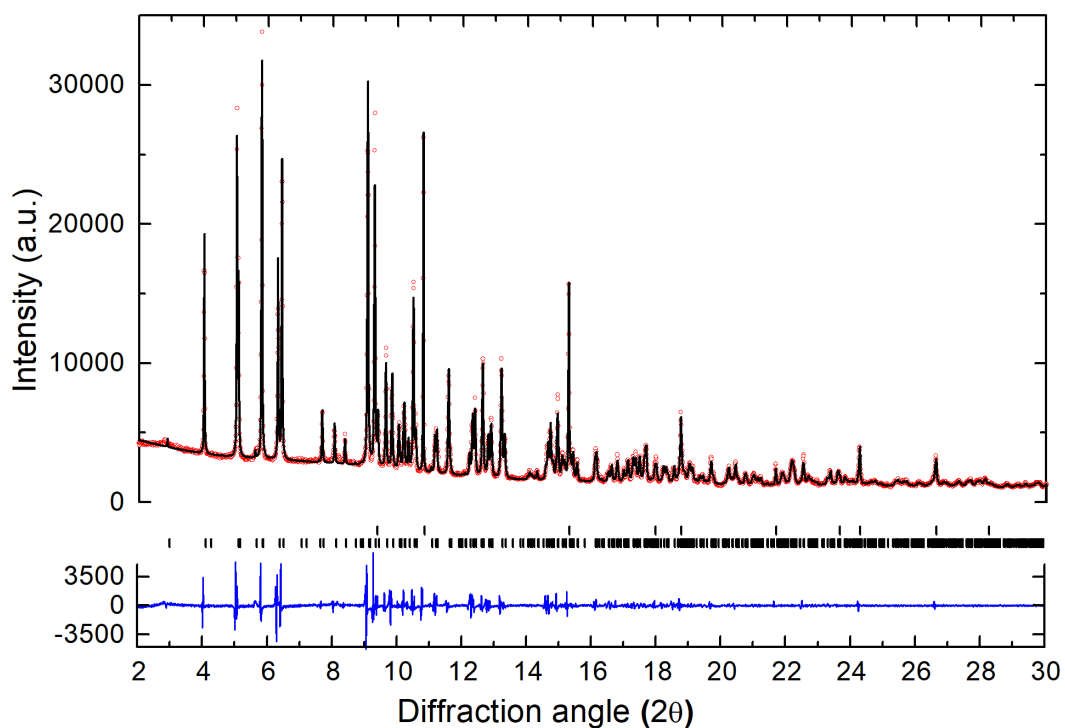
Figure B6. Synchrotron XRD pattern and Le Bail fit of $K_2B_{11}H_{11}Sn$ at room temperature. Experimental data as red circles, calculated diffraction pattern as black line and the difference plot in blue. Tick

marks show positions for LiCl and $K_2B_{11}H_{11}Sn$, top to bottom respectively. $\lambda = 0.59096(1)$Å. Le Bail plot for employed *hkl*'s for $K_2B_{11}H_{11}Sn$ generated using space group $P2_12_12$ with unit cell parameters $a = 11.7216(3)$, $b = 8.1006(1)$, $c = 12.0948(3)$ giving an $R_{wp} = 6.505$.

Appendix C

Supplementary Information for

"Monovalent heavy metal substituted

closo-dodecaborate ($B_{11}H_{11}M^-$) (M = Sb, Bi)

salts as potential solid-state ion

conductors"
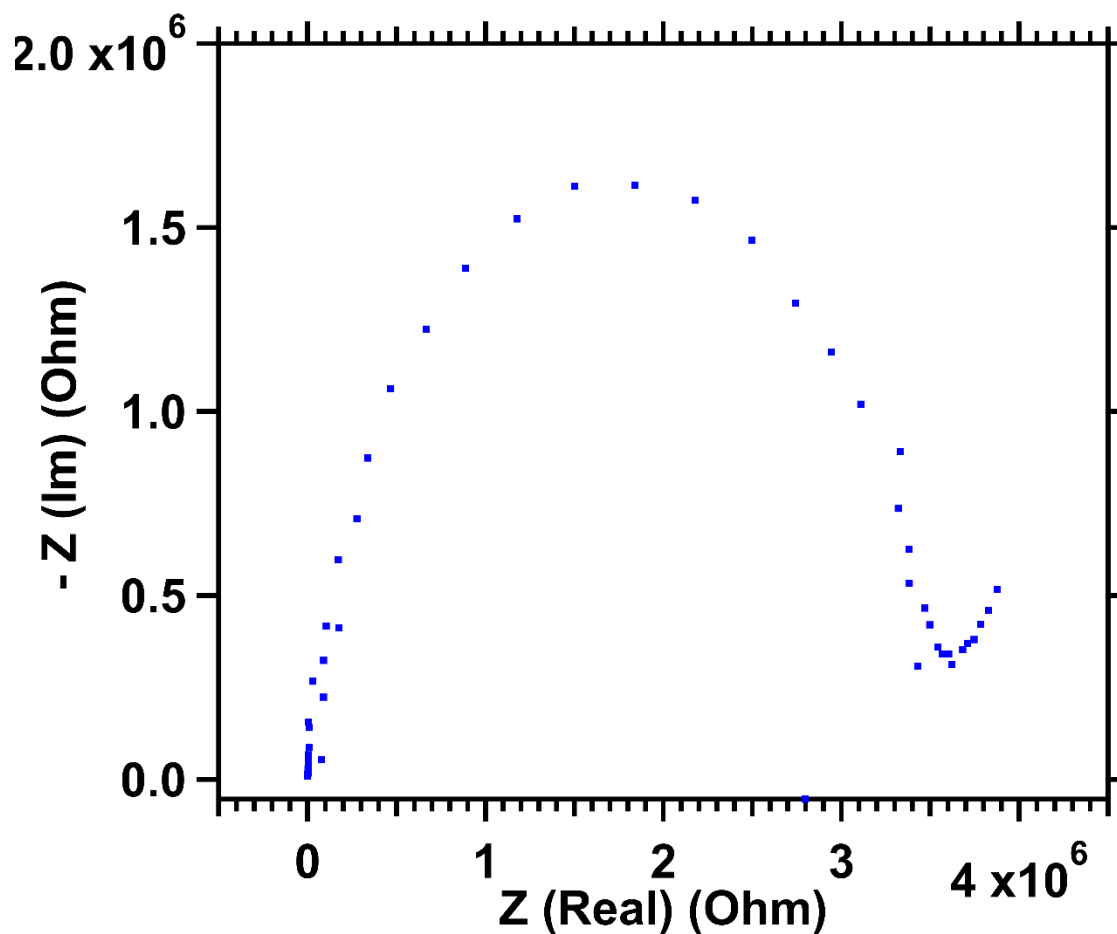
Figure C1. Example of a Nyquist plot of LiB$_{11}$H$_{11}$Sb at 50 °C, using an R_s-$R_1|C_1$-W circuit model.

Table C1. Atomic Coordinates of B$_{11}$H$_{11}$Sb$^-$ ion

Atom no.	x	y	z
B1	0.24007	0.51115	0.97344
B10	0.24015	0.93128	0.77807
B11	0.24006	0.87513	0.31809
B2	0.24017	0.42038	0.22928
B3	0.3207	0.54163	0.81713
B4	0.32058	0.35355	0.61509
B5	0.32069	0.48757	0.37373
B6	0.32068	0.75859	0.42663
B7	0.32068	0.79201	0.70073
B8	0.23995	0.19547	0.63441
B9	0.61186	0.28179	0.87028
H1	0.61178	0.76215	0.9643

H10	0.6119	1	0.53624
H11	0.61187	0.66641	0.17805
H2	0.54535	0.36729	0.46482
H3	0.54539	0.40279	0.75756
H4	0.54536	0.69252	0.81429
H5	0.54541	0.83588	0.5563
H6	0.54542	0.63472	0.34034
H7	0.61172	0.22271	0.38447
H8	0.17846	0.58673	0.58663
H9	0	0.58677	0.58663
Sb	0.82032	0.58666	0.58666

Table C2. Atomic Coordinates of $B_{11}H_{11}Bi^-$ ion

Atom no.	x	y	z
B1	0.23191	0.36428	0.33949
B10	0.23191	0.27393	0.77847
B11	0.2321	0.66344	1
B2	0.23198	0.99454	0.69802
B3	0.30993	0.46805	0.45332
B4	0.30998	0.73345	0.42366
B5	0.30999	0.84368	0.66692
B6	0.31009	0.64634	0.84691
B7	0.30997	0.4142	0.71488
B8	0.23196	0.80962	0.28979
B9	0.58999	0.57639	0.2203
Bi	0.59002	0.22605	0.53972
H1	0.59004	0.42167	0.9718
H10	0.59009	0.89307	0.91911
H11	0.52717	0.84234	0.52094
H2	0.52719	0.59421	0.37986
H3	0.52712	0.38325	0.57214
H4	0.52719	0.501	0.83224
H5	0.5272	0.78491	0.80051
H6	0.5901	0.98852	0.45469
H7	0.17261	0.62117	0.62121
H8	0	0.62112	0.62123
H9	0.80298	0.62113	0.62114
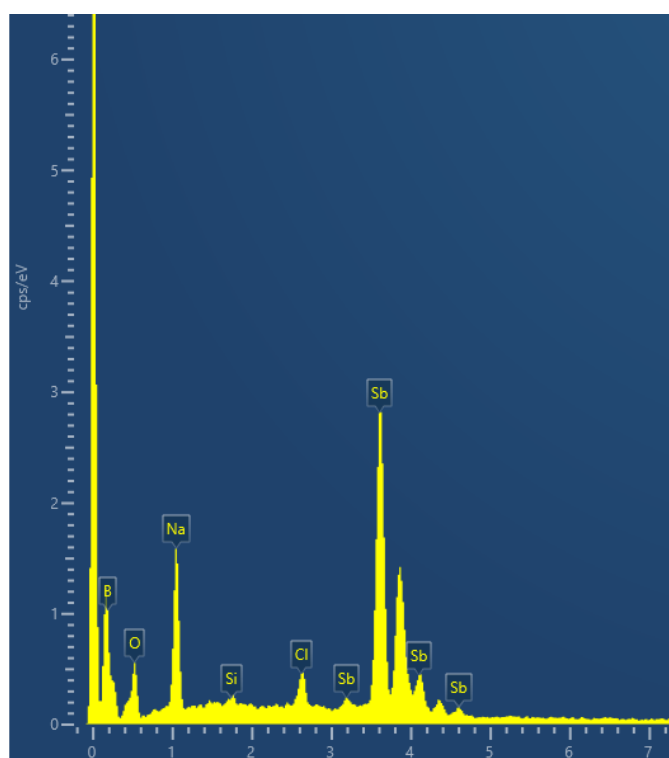
Figure C2. EDS Spectrum of $NaB_{11}H_{11}Sb$.

Appendix D

Co-Author Attribution Statements

APPENDIX D

Co-author Attribution Statement

Chapter 3: Investigating the potential of alkali metal plumba-*closo*-dodecaborate ($B_{11}H_{11}Pb^{2-}$) salts as solid-state battery electrolytes

	Concept and Design	Acquisition of Data and Method	Data Conditioning and Manipulation	Analysis and Statistical Method	Interpretation and Discussion
Thomas Hales	X	X	X	X	X
Acknowledgement: I acknowledge that these represent my contribution to the above research output and I have approved the final version Signed:					
Kasper Møller		X			
Acknowledgement: I acknowledge that these represent my contribution to the above research output and I have approved the final version Signed:					
Anita D'Angelo		X			
Acknowledgement: I acknowledge that these represent my contribution to the above research output and I have approved the final version Signed:					
Terry Humphries			X		X
Acknowledgement: I acknowledge that these represent my contribution to the above research output and I have approved the final version					

Signed: Craig Buckley					X
Acknowledgement: I acknowledge that these represent my contribution to the above research output and I have approved the final version Signed: Mark Paskevicius	X	X	X	X	X
Acknowledgement: I acknowledge that these represent my contribution to the above research output and I have approved the final version Signed:					

All DFT calculations were performed by Thomas Hales.

Co-author Attribution Statement

Chapter 4: Stannaborates: Tuning the Ion Conductivity of Dodecaborate Salts with Tin Substitution

	Concept and Design	Acquisition of Data and Method	Data Conditioning and Manipulation	Analysis and Statistical Method	Interpretation and Discussion
Thomas Hales	X	X	X	X	X
Acknowledgement: I acknowledge that these represent my contribution to the above research output and I have approved the final version Signed:					
Kasper Møller		X			
Acknowledgement: I acknowledge that these represent my contribution to the above research output and I have approved the final version Signed:					
Anita D'Angelo		X			
Acknowledgement: I acknowledge that these represent my contribution to the above research output and I have approved the final version Signed:					
Terry Humphries			X		X
Acknowledgement: I acknowledge that these represent my contribution to the above research output and I have approved the final version Signed:					

Craig Buckley					X

Acknowledgement: I acknowledge that these represent my contribution to the above research output and I have approved the final version

Signed:

Mark Paskevicius	X	X	X	X	X

Acknowledgement: I acknowledge that these represent my contribution to the above research output and I have approved the final version

Signed:

All DFT calculations were performed by Thomas Hales.

Co-author Attribution Statement

Chapter 5: Monovalent heavy metal substituted closo-dodecaborate ($B_{11}H_{11}M^-$) (M = Sb, Bi) salts as potential solid-state ion conductors

	Concept and Design	Acquisition of Data and Method	Data Conditioning and Manipulation	Analysis and Statistical Method	Interpretation and Discussion
Thomas Hales	X	X	X	X	X
Acknowledgement: I acknowledge that these represent my contribution to the above research output and I have approved the final version Signed:					
Terry Humphries			X		X
Acknowledgement: I acknowledge that these represent my contribution to the above research output and I have approved the final version Signed:					
Craig Buckley					X
Acknowledgement: I acknowledge that these represent my contribution to the above research output and I have approved the final version Signed:					
Mark Paskevicius	X	X	X	X	X
Acknowledgement: I acknowledge that these represent my contribution to the above research output and I have approved the final version Signed:					

All DFT calculations were performed by Thomas Hales.

Appendix E

Copyright Statements

APPENDIX E

Stannaborates: tuning the ion conductivity of dodecaborate salts with tin substitution

T. A. Hales, K. T. Møller, T. D. Humphries, A. M. D'Angelo, C. E. Buckley and M. Paskevicius, *Phys. Chem. Chem. Phys.*, 2023, Advance Article , **DOI:** 10.1039/D3CP03725H